

**Aus der Radiologischen Universitätsklinik Tübingen
Abteilung für Diagnostische und Interventionelle Neuroradiologie
Ärztliche Direktorin: Professor Dr. U. Ernemann**

**Multi-directional diffusion weighted imaging:
Implementation, verification and clinical application**

**Inaugural-Dissertation
zur Erlangung des Doktorgrades
der Humanwissenschaften**

**der Medizinischen Fakultät
der Eberhard Karls Universität
zu Tübingen**

vorgelegt von

Kamil Marek Gorczewski

aus

Gliwice, Polen

2011

Dekan: Professor Dr. I. B. Autenrieth
1. Berichterstatter: Professor Dr. U. Klose
2. Berichterstatter: Professor Dr. D. Kern

Multi-directional diffusion weighted imaging: Implementation, verification and clinical application

Kamil Gorczewski

Abstract

A water diffusion in a human brain can be used to analyze fibers within the white matter. The basis of the method is a measurement of a MR signal attenuation due to the water particles motion in a presence of a magnetic field gradient. The signal loss is related to the free path that a particle can travel. The obstacles keep the signal from the water spins coherent. Therefore, the attenuation of MR signal is stronger in the directions of the axons.

The information about the directional structure of the white matter can be extracted from the data with various methods. Those approaches can be divided into two groups: a model-based and direct measurements. Both groups have their own advantages and disadvantages.

The model-based approach like for example a diffusion tensor imaging (DTI) or a spherical harmonics deconvolution (SHD) can shorten the acquisition time and give high resolution images. However, the additional information from the acquisition have to be provided by some prior knowledge (response function in SHD) or assumptions (diffusion function can be described by a tensor). The results from those methods are biased by the first choice of the input functions.

At the other hand, a direct measurement is free from the mentioned above defects, but it requires more measurement time. The additional information has to be gathered in order to directly image the whole diffusion process. In clinical studies the acquisition time is important, because it is difficult to scan the patients longer than 90 minutes.

The aims of the thesis were to implement, verify and show in clinical conditions usefulness and advantages of a high angular resolution diffusion imaging in the diffusion measurements and the fiber tracing.

All measurements were performed on a 3T MR scanner approved for the clinical routines. The computer software layer was implemented during the work on this thesis.

Within this thesis a measurement sequence for multiple diffusion directions and processing routines were developed. Furthermore, it was presented how the implementation can be optimized. All results were obtained using only own software: a standard DTI tractography, a probabilistic segmentation, a q-ball fibre tracking. All implemented routines allow to measure and use a wide range of diffusion methods and adjust all the parameters according to a specific clinical task.

It was presented that all implementation of algorithms were validated with a digital or an artificial phantom as well as in in-vivo experiments. The validation addressed the second aim of the thesis. It was shown, that the proposed MR sequence modifications measure properly the diffusion properties of the human brain. All the data processing software shows a perfect agreement between the results and the assumed geometries and the tests. This gives a confidence in the results obtained in-vivo from the human brain.

It was demonstrated that an acquisition of a high angular resolution data is possible with typical parameters for the standard DTI measurements. The retrieved information about the water self-diffusion process allowed to reconstruct the optic radiation. This was possible with the most important feature of the q-ball measurements and the tracking: a crossing fibre reconstruction. The long optic radiation were successfully reconstructed and presented. Those fibres go through whole brain volume from the anterior to the posterior

passing multiple crossing regions on their way.

It was presented that the high angular resolution diffusion imaging can reconstruct the crossing fibers in an in-vivo experiment. A fiber crossing between the corpus callosum and the motor tract were shown as an example. Better quality of the directional data leads to the better fibre reconstruction. Additional information about the second diffusion direction not only makes the estimation more precise, but also enables the tracking algorithms to access regions of the brain usually not traceable.

The high angular resolution diffusion imaging is a step forward for white matters studies. Two major approaches compete between each other. At the one side, there is a data reconstruction without using any assumptions like q-ball and DSI. At the other side there are methods of a signal decomposition using the prior-knowledge (PAS-MRI, SHD). This work is part of this discussion showing capabilities both approaches and comparing the results obtained by both approaches. The presented material proves that the HARDI methods are acceptable for the clinical application in the human brain. Moreover, presented results show that the HARDI methods have the same reliability of the diffusion direction finding as the standard DTI, but the HARDI methods provide more sophisticated results. Multiple diffusion directions per voxel solves many of the problems found in DTI. The HARDI methods should replace in future the DTI measurements as the fiber crossing regions should be properly resolved for the fiber tracking.

Multidirektionale diffusionsgewichtete MR-Bildgebung: Implementierung, Verifizierung und klinische Anwendung

Kamil Gorczewski

Zusammenfassung

Mit Hilfe der Diffusion des Wassers im menschlichen Gehirn können Faserbahnen innerhalb der weißen Substanz untersucht werden. Die Grundlage der zugehörigen Messmethode ist die Signalabschwächung infolge der Bewegung von Wassermolekülen bei Verwendung von starken Gradienten des magnetischen Felds. Zum größten Signalverlust kommt es, wenn es eine ungehinderte Bewegung der Wassermoleküle gibt. Bei einer Einschränkung der Bewegung bleibt der Kohärenzverlust der Spins in Wassermolekülen geringer. In der Richtung der Axone, in der es weniger Bewegungseinschränkung gibt als senkrecht dazu, ist deshalb die Signalabschwächung größer.

Es gibt unterschiedliche Verfahren, um aus den gemessenen Daten die Information über die Ausrichtung der Fasern zu bestimmen. Dabei kann zwischen modellbasierten und modellfreien Methoden unterschieden werden. Bei modellbasierten Methoden wie der Diffusionstensorbildgebung (DTI) oder der Entfaltung auf der Grundlage von Kugelfunktionen (SHD) kann eine kürzere Messzeit verwendet oder eine höhere räumliche Auflösung erreicht werden. Allerdings benötigen diese Methoden die Verwendung von Annahmen, die damit auch Einfluss auf die erhaltenen Ergebnisse haben. Die modellfreien Verfahren haben diese Einschränkung nicht, aber sie erfordern eine längere Messzeit. Um den Diffusionsprozess vollständig zu erfassen, müssen zusätzliche Daten erfasst werden. Das kann zu einem Problem in klinischen Studien werden, weil die Untersuchungszeit von Patienten 90 Minuten nicht überschreiten sollte. Das Ziel dieser Arbeit war es, Verfahren der Diffusionsbildgebung, die eine hohe Anzahl von Diffusionsrichtungen verwenden, an einem klinisch genutzten Ganzkörpertomographen zu implementieren und Einsatzmöglichkeiten und Vorteile bei der Rekonstruktion von Faserbahnen aufzuzeigen.

Alle Messungen wurden an einem 3T-Gerät durchgeführt. Es wurde eine Messesequenz für vielfache Diffusionsrichtungen sowie Auswertungsroutinen und geeignete Oberflächen für die erforderlichen Computerprogramme entwickelt und optimiert. Bei der Auswertung wurden unterschiedliche Algorithmen realisiert und angewendet: die Standard DTI Traktographie, die probabilistische Segmentierung und die Q-Ball Faserrekonstruktion. Alle implementierten Routinen ermöglichten es, die erforderlichen Messparameter an die klinischen Erfordernisse anzupassen. Eine Validierung der eingesetzten Verfahren erfolgte anhand von digitalen oder hergestellten Phantomen und von in-vivo Messungen. Es konnte gezeigt werden, dass mit den vorgenommenen Veränderungen der Messesequenz die Diffusionseigenschaften des Gehirns gut wiedergegeben werden konnten. Mit unterschiedlichen Algorithmen wurden übereinstimmende Ergebnisse gefunden. Es konnte gezeigt werden, dass Messungen mit einer hohen Zahl von Diffusionsrichtungen mit den gleichen Messparametern wie übliche DTI-Messungen durchgeführt werden können. Als ein Beispiel für die korrekte Realisierung der Analyse der Daten aus diesen Messungen konnte der Verlauf der Sehstrahlung rekonstruiert werden. Das gelang mit Hilfe der wichtigsten Eigenschaft der Q-Ball-Messungen: der möglichen Rekonstruktion von Faserbahnkreuzungen. Die Fasern der Sehstrahlung verlaufen durch das gesamte Gehirn vom anterioren zum posterioren Teil und kreuzen dabei mehrere andere Faserbündel. Die Rekonstruktion von kreuzenden Fasern konnte auch im Bereich des Corpus callosum und der motorischen Faserbahnen gezeigt werden. Einer Erhöhung der Zahl der verwendeten Diffusionsrichtungen führte dabei zu einer verbesserten Faserbahnrekonstruktion. Die Einbeziehung der

zweiten Hauptfaserbahnrichtung ermöglichte es, Faserbahnen bis in diejenigen Regionen zu verfolgen, die bei konventionellen Rekonstruktionen nicht erreicht werden.

Die diffusionsgewichtete MR-Bildgebung mit einer hohen Zahl von Diffusionsrichtungen (HARDI) ist ein weiterer Schritt bei der Verbesserung der Untersuchungsverfahren der weißen Substanz des Gehirns. Bei der Auswertung solcher Daten konkurrieren zwei Ansätze: die Datenrekonstruktion ohne weitere Annahmen (Q-Ball-Analyse, Diffusionsspektrumbildgebung) und die Verfahren der Signalzerlegung (signal decomposition) unter Verwendung von definierten Annahmen (PAS-MRI, SHD). In dieser Arbeit wurden die Möglichkeiten beider Ansätze untersucht, und es wurden Ergebnisse, die mit beiden Ansätzen erhalten wurden, verglichen.

Es konnte gezeigt werden, dass HARDI-Methoden bei Bedingungen wie in klinischen Anwendungen am menschlichen Gehirn eingesetzt werden können. Sie ermöglichen die Rekonstruktion der Hauptfaserbahnen mit der gleichen Sicherheit wie die üblichen DTI-Verfahren, aber die HARDI-Rekonstruktionen führten zu zusätzlichen Ergebnissen. Die Einbeziehung einer großen Zahl von Diffusionsrichtungen reduzierte diejenigen Beschränkungen bei Faserbahnrekonstruktionen, die bei üblichen DTI-Verfahren auftreten. Die HARDI-Methoden sollten deshalb zukünftig die DTI-Messungen ersetzen, damit Regionen mit kreuzenden Faserbahnen in die Faserbahnrekonstruktionen einbezogen werden können.

Contents

1	Introduction	1
1.1	Aim of the work	2
2	Theory	3
2.1	Spins in the magnetic field	3
2.2	Rotating reference frame	4
2.3	Relaxation process	5
2.4	MR imaging	6
2.4.1	MR sequences	6
2.4.2	RF pulses	7
2.4.3	Spin echo	9
2.4.4	Gradients for Imaging	9
2.4.5	Gradient echo	11
2.4.6	Echo Planar Imaging	12
2.5	Diffusion theory and measurement	13
2.5.1	Diffusion Tensor Imaging	16
2.5.2	Q-space description and Diffusion Spectrum Imaging	19
2.5.3	Q-ball imaging	21
2.5.4	Spherical harmonics de-convolution	23
2.6	Anatomical origin of diffusion in human brain	25
2.7	Fiber tracking concepts and strategies	25
2.7.1	Deterministic Fiber Tracking	27
2.7.2	Probabilistic and Stochastic Fiber Tracking	29
3	Methods	31
3.1	Implementation	31
3.1.1	Measurement	31
3.1.2	Data processing	35
3.1.3	Fiber Tracking	39
3.1.4	Fiber Tracts Analysis	44
3.2	Validation	46
3.2.1	Digital phantoms	46
3.2.2	Artificial phantoms	47
3.3	Design of human brain experiments	48
3.3.1	First experiment: q-ball, Tensor and SD comparison	48
3.3.2	fMRI and DTI in optic radiation	50
3.3.3	Third experiment: Probabilistic/Stochastic approach	53
3.3.4	Fourth experiment: q-ball whole-brain fiber tracking	53

4	Results	55
4.1	Digital phantoms	55
4.2	Comparison of artificial phantoms quality	56
4.3	Fiber crossing phantom	59
4.4	SD, q-ball and tensor results comparison	60
4.4.1	Main direction of diffusion	61
4.4.2	Second direction of diffusion in q-ball reconstruction and SD	63
4.4.3	Influence of smoothing and b-value	64
4.5	fMRI and DTI	64
4.5.1	DTI results	65
4.5.2	Segmentation of the fiber bundle	65
4.6	Probabilistic approach	67
4.6.1	Adjustments of the random direction generator	67
4.6.2	Digital phantom	70
4.6.3	Thalamus segmentation	71
4.7	Q-ball tracking	74
4.7.1	Crossing regions	74
4.7.2	Tracking results	74
5	Discussion	77
5.1	Implementation	77
5.1.1	Data processing	78
5.1.2	Fiber tracking	78
5.2	Validation	79
5.2.1	Artificial phantoms	79
5.2.2	SD, q-ball and DTI comparison	80
5.3	Clinical applications	82
	Acknowledgements	84
6	References	86
A	CURRICULUM VITAE	93

Chapter 1

Introduction

The use of the Magnetic Resonance Imaging (MRI) in a medicine exploits the magnetic properties of the protons for diagnostic purposes. Multiple physical properties can be measured by the MRI. The main properties are: relaxation times, a proton density, a perfusion and a diffusion. The scope of this thesis focuses on the diffusion measurements.

An anisotropic diffusion of the water molecules was found in tissues like muscles [1][2] or the brain [3]. The water molecules probe the tissue structure at a microscopic scale well beyond the image resolution. During a typical diffusion time, the water molecules move in the brain on average over a distances around $10\ \mu\text{m}$, bouncing, crossing, or interacting with many tissue components such as cell membranes, fibers, or macromolecules.

The mentioned processes gave a beginning to a whole family of the acquisition and the processing methods. Those methods focus on exploring of the information hidden inside a voxel volume. By probing the water self-diffusion properties, this method have an unique chance to bring up to front the structural information of the examined materials.

The measurement of a diffusion coefficient regardless of its direction is a key feature of a diffusion weighted imaging (DWI). Changes in self-diffusion properties of the water molecules can detect the early-stage brain strokes [4]. These measurements became very important in a clinical practice. At this point, the DWI was finding regions of different diffusion coefficients.

The next step in the diffusion methods development was a discovery that the diffusion coefficients measured with the DWI were dependent on the direction in which this diffusion was measured. A pioneer work to explore the directional dependence of the diffusion was performed by Basser et al. [5]. An introduction of the tensor description in the diffusion measurements opened a way to calculate the direction of water molecules diffusion. A diffusion Tensor Imaging (DTI) is now the state-of-the-art method, due to its short acquisition time and the ease of the data processing. The tensor model is assuming, that there is an unique and dominating direction of the diffusion inside the voxel.

For more than ten years the DTI is now providing a reliable information about the directions of the water diffusion and the anisotropy levels mainly in the human brain, but also in the spinal cord and the muscles. The white matter of the brain is a complex structure and the tensor model have a difficulty in a straightforward resolution of the diffusion direction in a significant amount of the cases. A typical imaged voxel size is in range of millimeters. This volume of the white matter contains thousands of nerve axons. Those fibers can cross, split and join inside the voxel volume.

The diffusion measurements are carrying more information than the tensor model could process. For that reason, numerous solutions were provided to explore more complex diffusion information. Those methods were measuring multiple diffusion coefficients. Each was described by the acquisition parameters. All the possible parameters were included

in a space, called q-space [6]. Regardless of the processing method used, the q-space methods were able to discover more than one dominant diffusion direction per voxel.

The information about the direction of the diffusion in the white matter is connected with the directions of the axons. Assuming that the water diffuse along the axons, the directions provided by the DTI or the q-space are in fact the directions of the neuron bundles. Mori et al. [7] proposed a streamline algorithm capable of the reconstruction of the connections in the brain. This method enabled us to examine and segment the fiber tracts *in-vivo*.

The described methods require a validation and in many cases an optimization. Before clinical decisions are made based on those methods, one have to be sure about the reliability and also one have to be aware of possible errors and limitations of the methods. Possible future clinical applications seems to be very broad, like assisting during a neuro-surgery with information about the actual fiber bundles position, so a surgeon can plan the entry point to preserve certain neuron bundles.

1.1 Aim of the work

The aim of this work was to bring the q-space diffusion measurements to the clinical realm and to show that it is possible to improve the fiber-tracking results by using the data containing more than one average diffusion direction. Particularly, three sub-aims can be distinguished:

Implementation

The aim of this part was to prepare a MR sequence suitable for the diffusion measurements. The sequence should measure the diffusion directions according to the q-space sampling. Secondary aim was to implement the software for the data processing of the DTI and the q-space experiments. The final aim of this part was to create a software for the fiber tracking and the fiber analysis that can use both the DTI and the q-space data.

Validation

The aim of this sub-section was to test the written software, prepare proper digital and artificial phantoms for a simulation. The developed algorithms were tested and adjusted for the best performance with the data from the brain diffusion measurements. Additionally, the diffusion methods were compared.

Clinical application

In this part, the aim was to show that clinical relevant results can be obtained in a time suitable for the patients. The optic tract was reconstructed using the DTI and the functional MR, the thalamus was segmented using the probabilistic fiber tracking and the whole-brain q-space imaging was performed with examples of a crossing fibers resolution.

Chapter 2

Theory

2.1 Spins in the magnetic field

Most of the atoms have a property called nuclear spin (\mathbf{I}). It is similar to an angular momentum (\mathbf{J}). A non-zero spin is connected with a magnetic moment in this way:

$$\mu = \gamma_1 \mathbf{J} = \hbar \gamma_1 \mathbf{I} \quad (2.1)$$

where γ_1 is a gyromagnetic coefficient.

The hydrogen has the largest gyromagnetic moment among all known stable isotopes. Due to this fact and to the information that the hydrogen is the most common element of biological systems, the usage of the ^1H is the best and the easiest approach for Magnetic Resonance Imaging (MRI).

In a system with a large number of spins without a magnetic field, the directions of magnetic dipoles are completely random. External magnetic field will restrict the possible spin direction. The magnetic moments now can be only parallel or anti-parallel to the direction of the external magnetic field. The distribution of the quantum number m_I is discrete with the values of $\frac{1}{2}$ and $-\frac{1}{2}$, which represents the parallel and the anti-parallel situation.

This spin collection energy splitting is called the Zeeman effect. The energy level of a single spin can either:

$$E_1 = \frac{1}{2} \hbar \gamma_I B_0 \quad (2.2)$$

or

$$E_2 = -\frac{1}{2} \hbar \gamma_I B_0 \quad (2.3)$$

The external energy can be provided to a spin collection by an electro-magnetic pulse. The most efficient induction of a spin passing from lower to higher energy state is when the electro-magnetic pulses have the energy similar to the gap between E_1 and E_2 . The energy of electro-magnetic pulse is described by its frequency and it equals to $\hbar\omega$. The resonance condition is:

$$E_2 - E_1 = \Delta E = \hbar\omega = \hbar\gamma_I B_0 \quad (2.4)$$

This condition can be simplified, and stated as: the resonance frequency ω depends only on the magnetic field \mathbf{B}_0 strength and the gyromagnetic coefficient γ_I , which is constant for a given nucleus. The resonance frequency is also called *the Larmor frequency*.

The number of nuclei in macroscopic samples is in a range of the Avogadro number. One cubic centimetre of water contains approx. 10^{23} hydrogen atoms with a random

distribution of the magnetic momentum directions. The ratio between the number of parallel (N^+) and anti-parallel(N^-) spins is given by the Boltzman relation:

$$\frac{N^-}{N^+} = \exp\left(-\frac{\Delta E}{kT}\right) \quad (2.5)$$

The spin system would split half-to-half only for a very high temperature, as the value inside the exponent from eq.2.5 approaches to 0. In the case of human body temperature, a small surplus of spins parallel to the external magnetic field is enough to create measurable, macroscopic magnetization \mathbf{M}_0 . The measurement of this magnetization lays at the basis of all MR experiments.

2.2 Rotating reference frame

The most natural coordinate system is a laboratory reference frame or in other words a scanner reference frame, defined as Cartesian system, where the OZ axis is parallel to the direction of the \mathbf{B}_0 field. It goes through the magnet bore. The OY axis is usually parallel to the gravitation force. When the subject's head is in the scanner it is anterior-posterior direction. The OX axis goes from the left to the right side of the scanner or the subject.

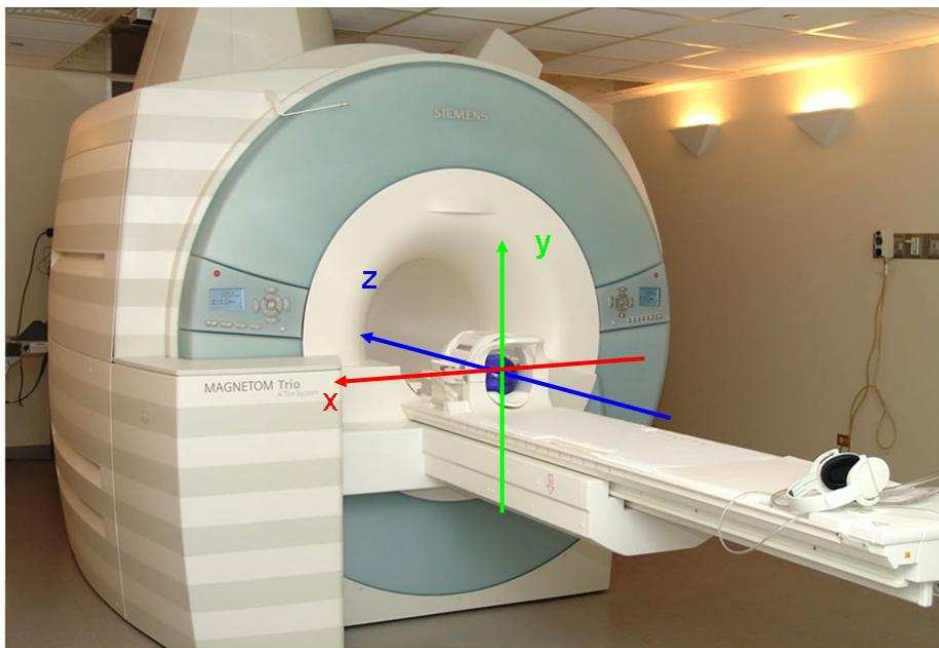


Figure 2.1. A image of SIEMENS 3 [T] MR scanner TRIO. The axes of laboratory reference frame where indicated by arrows. This color and configuration scheme is maintained through all of the thesis.

The quantum physics describe the interactions between the spins. It is necessary to use this description in MR spectroscopy. However, in the case of MR imaging, it sufficient to use a classical description.

In the classical model, the spins in the magnetic field precess with a frequency of ω_0 about the direction of the magnetic field. The energy delivered by the electro-magnetic field will result in a complex trajectory in the laboratory reference frame. To simplify the calculation it is wise to use a notation in the rotating reference frame. The rotating reference removes the precession component from the spin and the magnetisation trajectories. Let us assume there is a vector $\mathbf{p}(t)$ in the laboratory reference frame whose components

are:

$$\mathbf{p}(t) = p_{x'}(t)\hat{\mathbf{x}}' + p_{y'}(t)\hat{\mathbf{y}}' + p_{z'}(t)\hat{\mathbf{z}}' \quad (2.6)$$

The same vector can be described in the rotating reference frame. The new coordinate system rotates about the direction of the magnetic field \mathbf{B}_0 with the angular velocity equal to the resonance frequency ω_0 :

$$\mathbf{p}(t) = p_x(t)\hat{\mathbf{x}} + p_y(t)\hat{\mathbf{y}} + p_z(t)\hat{\mathbf{z}} \quad (2.7)$$

Because the magnetic field \mathbf{B}_0 is parallel to the OZ axis of the laboratory reference frame, therefore:

$$\hat{\mathbf{z}}' = \hat{\mathbf{z}} \quad (2.8)$$

The two sets of transverse axis are described by a rotation:

$$x = x' \cos(\omega_0 t) - y' \sin(\omega_0 t) \quad (2.9)$$

$$y = x' \sin(\omega_0 t) + y' \cos(\omega_0 t) \quad (2.10)$$

Using the matrix algebra it is possible to create a rotation matrix R that transforms points and vectors from the laboratory reference frame to the rotating reference frame.

$$\begin{bmatrix} p_x \\ p_y \\ p_z \end{bmatrix} = \begin{bmatrix} \cos(\omega_0 t) & -\sin(\omega_0 t) & 0 \\ \sin(\omega_0 t) & \cos(\omega_0 t) & 0 \\ 0 & 0 & 1 \end{bmatrix} \begin{bmatrix} p_{x'} \\ p_{y'} \\ p_{z'} \end{bmatrix} = R \cdot \mathbf{p}' \quad (2.11)$$

The reverse operation can be achieved by using inverse matrix R^{-1} , which in the case of the rotation matrix is a transposed matrix R^T .

2.3 Relaxation process

A proper choice of the RF pulse can bend the magnetization from its equilibrium state. The RF pulse rotates the magnetization vector in the transverse plane. *The relaxation* is a natural process of returning of the spin system to the equilibrium state.

Relaxation involves exchange of energy between spins and between spins and the surrounding environment, called *the lattice*. This energy transfer implies magnetic interactions with the magnetic dipoles associated with the spins. For nuclei with $I > \frac{1}{2}$, also an associated quadrupole moment may interact with the electric field gradient, but it is not present in ^1H imaging. Relaxation results from a fluctuation in these interactions, which arise from the Brownian motion of the molecules.

The relaxation is described by the Bloch equations ([8]). They include description of the most important processes of magnetization relaxation. There are more ways for losing energy by the spin system however, those processes are not so important for imaging techniques. They find application in such fields of MR like spectroscopy, where a simple model of magnetisation shown here is not enough and a quantum approach have to be used. Two solutions eqs. 2.12 and 2.13 of the Bloch equations are presented below.

Longitudinal Relaxation

If the magnetization is tilted from its equilibrium position along the direction of magnetic field and the system is allowed to relax, it will return to its equilibrium position.

The behaviour of M_z component of magnetization is controlled by a first-order process characterized by time constant T_1 , according to:

$$\frac{dM_z}{dt} = -\frac{(M_z - M_0)}{T_1} \quad (2.12)$$

The T_1 constant is called in literature the *longitudinal relaxation time* or the *spin-lattice relaxation time*. In this interaction the energy is transferred to the lattice (whatever that maybe): solvent, electrons in the system, or other kinds of atoms or ions. The energy is converted into translational or rotational energy and the nucleus returns to the lower energy state.

Transverse Relaxation

The M_x and M_y components of magnetization also return to their equilibrium state, which is zero. This return corresponds to the dephasing of the spins, once phased by the RF pulse. During dephasing process, energy interchanges between spins causing magnetization changes. The resulting component in the XY-plane, which is a sum of all individual moments, will then decrease. As in the case of longitudinal relaxation, this phenomenon is a first-order process characterized by the time constant T_2 , called the *spin-spin relaxation time* or the *transverse relaxation time*. T_2 is given by the equation:

$$\frac{dM_x}{dt} = -\frac{M_x}{T_2}, \quad \frac{dM_y}{dt} = -\frac{M_y}{T_2} \quad (2.13)$$

2.4 MR imaging

Among many applications of the magnetic resonance, the imaging techniques play a large role in the medical diagnostics. The spin properties can be measured and located in the 3D space. The MR imaging consist of three layers: the hardware, the MR sequence and the computer software. The MR equipment, commonly called *MR scanner* consists of a high field super-conductive magnet for producing the static \mathbf{B}_0 field. Its strengths for the clinical applications vary from 0.5 T up to 3 T and research prototypes have field strengths up to 9.4 T. The transmitter-receiver coils are responsible of providing the RF energy to the spin system and to measure its response. In order to obtain a signal, the RF pulse has to be transmitted into the imaged object. The spins are transmitting back the signal while returning to the equilibrium point. Usage of a multiple receiving coils can speed up the measurement. Those techniques are called a parallel imaging, since the signal is gathered in parallel from many receivers. The last component of the MR hardware is the field gradient system which provides the spin localisation through a small changes of the static magnetic field, which leads to the change of the resonance frequency (eq.2.4) in relation to the spin position along the direction of the applied gradient.

2.4.1 MR sequences

The second layer is the *MR sequence*, using and working on the hardware layer. In the simplest approach, the sequence is a time-table containing the behaviour of all the hardware components. The sequence describes timings and strengths of the RF pulses and the gradients and also when the MR signal should be recorded. The sequence design is the key in the MR imaging. Different contrasts and information can be retrieved by using properly chosen combinations of the RF pulses and the gradients. The MR sequence can

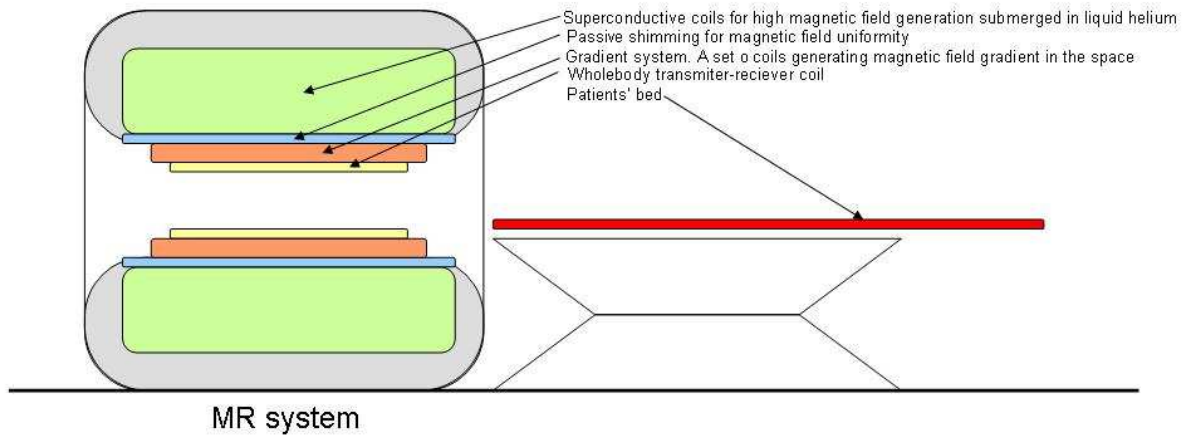


Figure 2.2. A general schema of MR system with main hardware components. A) Super-conductive coils for strong magnetic field generation, B) Passive shimming for magnetic field homogeneity, C) A system of coils generating small magnetic field gradients in the bore, D) Whole-body transmitter-receiver coil, E) Patient's bed.

be described by five time-lines. The first one shows the behaviour of the RF transmitter, the following three describe the field gradient in the laboratory reference frame in three orthogonal direction XYZ (Z is the direction of the static field). The last one controls the receiver coils recording.

After the measurement is completed the *software layer* takes control and it evaluates the requested images. The first part works on raw data, the main aim here is to combine signal into images. Next parts use the calculated images to get additional and more complex information.

The most important part of a MR sequence is a *excitation pulse*, which provides the initial energy to the system. It is an RF pulse with the carrier frequency equal to the resonance frequency of the spins (for the maximal energy deposition). The midpoint of this pulse in the sequence is usually considered as zero time event. There are some parts of the sequence applied before the zero time, they serve as a support for getting better signal quality. They are described in the last part of this subsection.

After the excitation pulse, spin phases and frequencies are changed using field gradients for spatial encoding. The contrast in the image can be changed by an alternation of the timing between the RF pulses and the gradients in the MR sequence. This part also may contain additional RF pulses required for the signal formation. At the end the signal occurs and it is measured by the receiver coils.

2.4.2 RF pulses

The radiofrequency pulses consist of the carrier frequency and the amplitude envelope. The carrier frequency in all sequences used in this thesis was always set to the resonance frequency of the hydrogen. The shape of the envelope in time was set in order to obtain a proper shape of the excitation shape in the space. The excitation pulses flips the magnetization vector away from the equilibrium position, which is parallel to the main magnetic field \mathbf{B}_0 .

The amplitude envelope of this pulse is commonly denoted by $\mathbf{B}_1(t)$. The duration of the pulse has to be short enough, so that T_1 and T_2 relaxation can be neglected during the pulsing. A typical duration times used in the imaging sequences are in range from 200 μs to 5 ms. The excitation pulses are described by their *tip angle* or *flip angle* and denoted as

θ . This is an angle between the direction of the main magnetic field and the magnetisation vector. Each MR sequence has to have at least one excitation pulse. Typically, the flip angles of $\theta = 90^\circ$ are used in spin echo sequences and a flip angle in range $5 - 70^\circ$ are used for gradient echo pulse sequences. The sequences that use spin-echos also require a re-focusing RF pulse ($\theta = 180^\circ$).

The flip angle θ depends on the amount of the electro-magnetic energy delivered to the system and it is proportional to the pulse envelope $\mathbf{B}_1(t)$. This can be derived from the Bloch equations. The angle between the main direction of the magnetic field and the direction of magnetization right after RF pulse is given by:

$$\theta = \gamma \int_0^t B_1(t') dt' \quad (2.14)$$

The flip angle depends on the area under the amplitude envelope of the RF pulse for the standard SINC pulses. In the case of off-resonance excitation, the complex calculus has to be used. The $\Delta\omega$ has to be small, due to a resonance nature of the phenomenon. Using large frequency differences result in a very low energy transfer.

$$I_{SINC} = \frac{\sin(x)}{x} \quad (2.15)$$

Because most of the imaging pulse sequences require RF pulses with a spectral or spatial selectivity, the rectangular shape of $\mathbf{B}_1(t)$ is infrequently used, except of the 3D acquisitions in which sometimes the volume is sufficiently large to cover the entire sensitive region of the coil. Rectangular pulses are also used to create tagging sequences for motion detection. The most widely used pulses for selective excitation, saturation and re-focusing

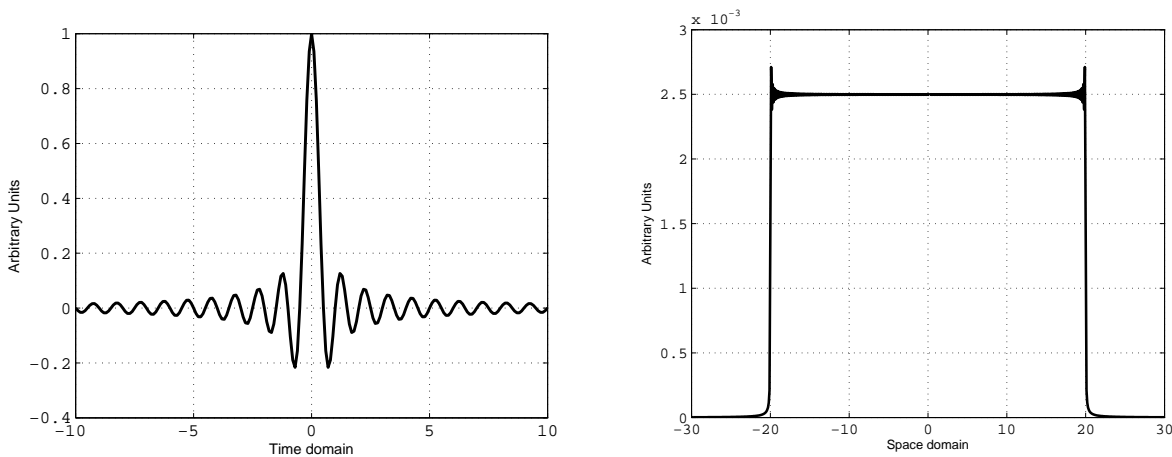


Figure 2.3. The shape of RF pulse in the time (left) and space (right) domain. The spin-pulse (left) is usually used in MRI to create rectangular excitations (right) in space

are the SINC pulses. Those pulses have several adjacent lobes of alternating polarity. The central lobe has the highest amplitude. The amplitudes of the other lobes progressively decrease on either side of the main lobe, as their polarity alternate (figure 2.3-left).

The frequency profile and also a spatial profile are well approximated by the Fourier transform. (The shapes of the frequency and slice profiles are equivalent when a slice-selection gradient is enabled during the RF pulse for small flip angles). The Fourier transform of an infinitely long SINC pulse (figure 2.3-left) is a rectangular form (figure 2.3-right).

2.4.3 Spin echo

The MR signal comes from a sum of all dephasing spins after an excitation pulse. Usually the first pulse has the angle of $\frac{\pi}{2}$ which maximizes the response signal amplitude. The magnetization is aligned after the RF pulse on the transverse plane. Process of spin dephasing starts immediately after the excitation pulse. The frequency of the precession depends on the local magnetic field. In the absence of any interactions, all spins would rotate with the same frequency. Those interactions can be divided into reversible and irreversible. The irreversible have a random nature like temperature and magnetic field inhomogeneities and the reversible can be explained by the local field changes, which can be generated by field gradients.

Spins are experiencing slightly lower or higher magnetic field, so their Larmor frequencies will differ. Spins in one voxel, which are out of phase do not produce any signal on the receivers, since transverse components cancel out each other. Only spin in-phase can produce measurable magnitude of the signal inside a voxel.

2.4.4 Gradients for Imaging

The imaging process in a modern MR scanner is done by exciting a specific volume of interest and then to produce an echo which will contain the information of the imaged object. To achieve this magnetic field gradients have to be applied in order to prepare the spin collection for the imaging. Three following types of gradients can be found in the imaging sequences.

Frequency-Encoding Gradients are commonly used to spatially encode an NMR signal by assigning a unique precession frequency (i.e. Larmor frequency) to each spin at a distinct spatial location along the gradient direction. Under the influence of this gradient, the time-domain NMR signals will consist of a range of frequencies, each corresponding to a different spatial localisation. An inverse Fourier transform of the time domain signal reveals the frequency content. Each frequency is linearly related to the corresponding spatial location along the gradient direction.

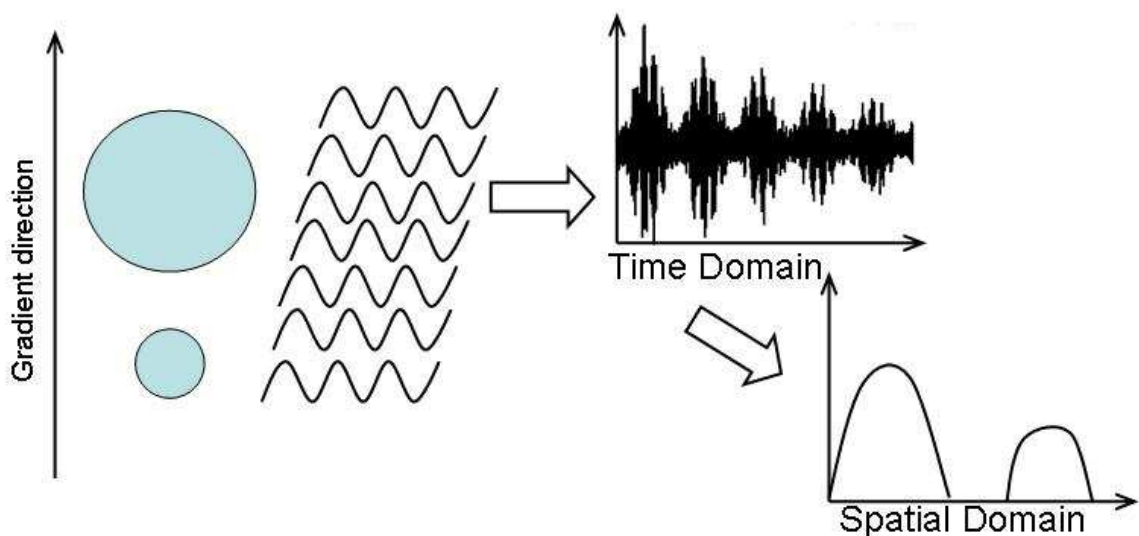


Figure 2.4. Encoding spatial distribution of spins using frequency encoding gradients. The signal received from different positions, in the presence of field gradients, have different resonance frequencies. After the Fourier transform, objects' positions are restored.

The presence of the gradient introduces spatially dependent changes of B_0 . Figure 2.4 shows an example of two spherical distributions of spins in the space (blue circles). Assuming that an excitation pulse was applied before the frequency encoding gradients, the spins in each position will have different frequency. The difference depends on the gradient duration and the amplitude. When the echo appears at the end of the sequence, the signal in the time domain will contain multiple frequencies. The Fourier transform can retrieve the information about the spatial distribution of the spins.

Spatial localization in the MR usually employs both the previously mentioned Frequency-encoding and the *Phase-Encoding Gradients*. With the frequency encoding, the precession of the magnetization is spatially varied across the object in a linear relation with the position. The idea behind frequency encoding is to also create a linear spatial variation of the phase of the magnetization. The phase encoding is implemented by applying a gradient in between the acquisitions. The phase and frequency-encoding gradients are usually orthogonal. After applying both gradients, the imaging object is divided into columns with the same precession frequency, but with different phase in a relation to the position and the row with the same phase shift, but different frequencies. The acquisition of signal is repeated for all phases present in the object. Therefore, multiple excitations are required for phase encoding. Information from each point of object is collected and properly labelled. The spatial image can be reconstructed when Fourier transform is used.

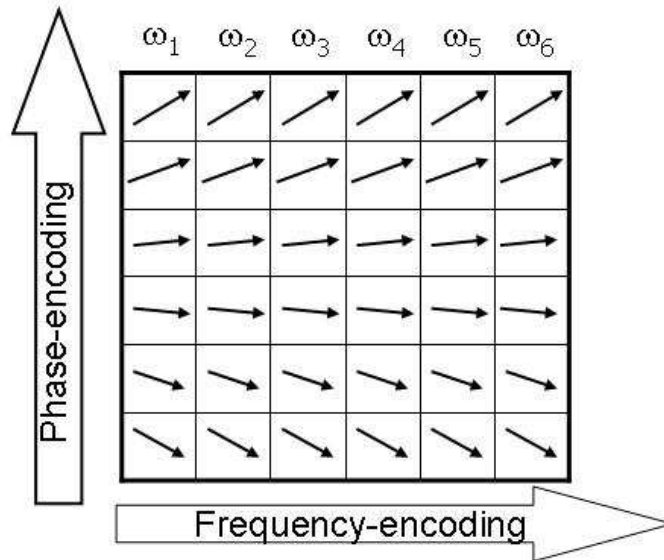


Figure 2.5. Encoding of spatial information using frequency and phase encoding gradients. Application of second gradient (after frequency-encoding) varies the spins phases. This way only spins in one row create an echo with frequency-encoded positions of spins. Whole 2D image can be acquired by repeating the measurements with different phase-encoding gradients

During the application of a y phase-encoding gradient G_y , the angular frequency of precession in the B_0 rotating frame is given by:

$$\omega = \gamma G_y y \quad (2.16)$$

The phase ϕ (in radians) of the transverse magnetisation at the end of the phase-encoding pulse is:

$$\phi(y) = y\gamma \int_0^T G_y(t') dt' \quad (2.17)$$

where T is duration of gradient G_y . The signal detected is the vector sum of the magnetization of all nuclear spins in the object. The effective magnetization is $M_{\perp} = M_x + iM_y$.

The signal is phase sensitive and given by:

$$M(y) = \int M_{\perp}(y)e^{-i\phi(y)} dy \quad (2.18)$$

Labelling of the location in 2D plane was described above. Now, when the spins varies by frequency and phase, there is a need to encode the third direction to have a defined slice in the space. The last direction is chosen by applying a *Slice-Selection Gradients*, which is typically constant gradient that is enabled when RF excitation pulse is emitted. Modulating the RF envelope with a predetermined, such as SINC pulse, generates a selective RF pulse. The bandwidth Δf , which is the range of frequencies present in the pulse (figure 2.3).

The slice-selection gradient translates the band of frequencies into desired band of locations. The frequencies present in the RF pulse can excite only spins that have a specific resonance frequency and since the slice-selection gradient is on, the Δf excites spins in some slab Δz (figure 2.6). The position and the slice position can be altered by changing the RF pulse bandwidth or the gradient amplitude. On the figure 2.6, the same Δf applied with two gradients $G_{z,1}$ and $G_{z,2}$ produces excitation in positions Δz_1 and Δz_2 . Greater gradient amplitudes are producing thinner slices.

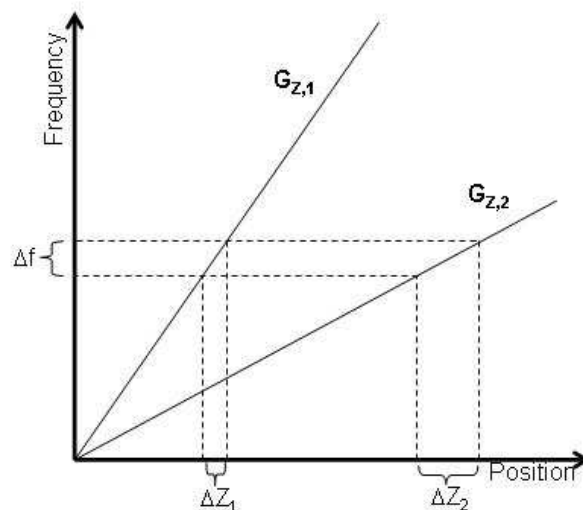


Figure 2.6. Slice thickness in relation to gradient strength. A field gradient present during an RF pulse with frequency range Δf , excites spins in a certain range ($\Delta z_1, \Delta z_2$). The width and position of the excitation range can be controlled by gradient strengths ($G_{z,1}, G_{z,2}$).

Any of the three orthogonal gradient of MR system (or a linear combination of them) can be used for slice selection. The gradient direction determines the *normal* (line perpendicular to the plane of the slice). Usually the desired slice plane does not pass through the point where all three gradients coils produce zero magnetic fields (i.e. the iso-center of the coils). In this case, the desired offset is obtained by shifting the carrier frequency of the RF pulse.

The handling of the received signal is described in the chapter 3.1.1, where the real implementation of the diffusion sequence is described.

2.4.5 Gradient echo

Gradient echo (GRE) is the name for a class of pulse sequences that is primarily used for fast imaging. GRE is used also in 3D volume imaging and other applications that require

acquisition speed. The echoes are also called gradient-recalled echoes, gradient-refocused echoes and field echoes.

A GRE pulse sequence do not have π -refocusing pulse that is used to form a spin echo. Instead, gradient reversal on the frequency-encoded axis forms an echo. First a readout prephasing gradient lobe dephases the spin isochromats, and they are rephased with a readout gradient that has opposite polarity.

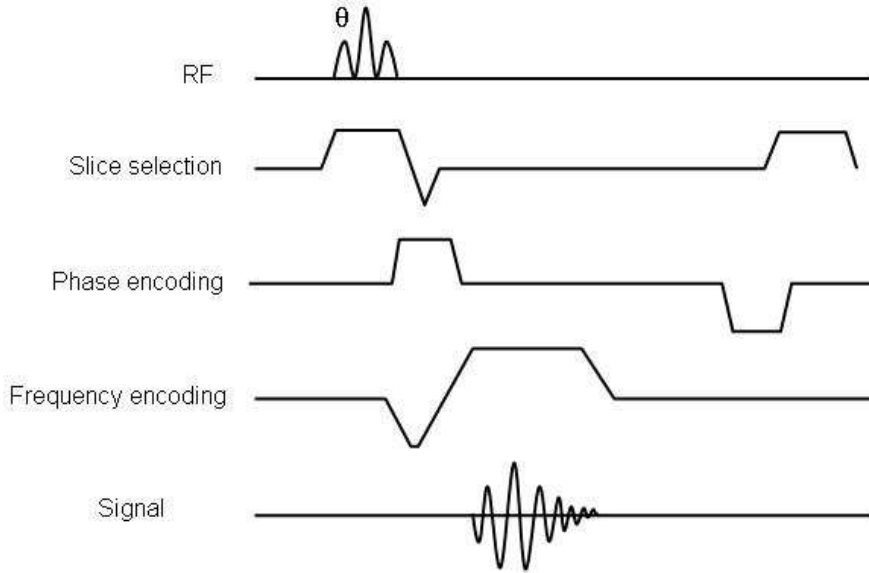


Figure 2.7. Gradient echo sequence. Four time-lines are shown. These five plots describe completely all MR scanner's components and relations between them.

Figure 2.7 shows a typical pulse sequence diagram for a GRE pulse sequence. The common features are illustrated, like gradient reversal on the frequency encoding axis, the echo acquisition, the phase encoding lobe, and the rewinder. GRE acquisitions can be fast because the flip angle can be less than $\frac{\pi}{2}$, so there is no need to wait for T_1 recovery. Since there is no re-focusing pulse, short TE can be achieved (2 – 50 ms). The GRE images are weighted by a factor of e^{-TE/T_2^*} , instead of e^{-TE/T_2} as it was in the case of spin echo. The parameter T_2^* is called *apparent* T_2 and it is related to the spin-spin relaxation time T_2 by:

$$\frac{1}{T_2^*} = \frac{1}{T_2} + \frac{1}{T_2'} \quad (2.19)$$

where T_2' is inversely proportional to the magnetic field inhomogeneity ΔB in each imaging voxel, that is, $T_2' \sim 1/(\gamma\Delta B)$. Whereas T_2 is an intrinsic property of the tissue, T_2' and T_2^* depend on external factors (e.g. susceptibility variations within the patient, how well the magnet is shimmed and the B_0 field strength).

2.4.6 Echo Planar Imaging

A read-out technique called *Echo Planar Imaging* (EPI) is one of the fastest in MR imaging. Full image can be obtained after just a single excitation pulse in less than 100 ms. This ultrafast imaging plays an important role in diffusion imaging, but also finds wide applications in other MR applications [9].

EPI maximally uses the transverse magnetisation by producing a series of oscillating bipolar gradients before the transverse magnetization disappears due to T_2^* -relaxation. Those gradients create a collection of echoes, which are individually phase encoded.

By adding small phase encoding gradients it is possible to cover k-space sufficiently to reconstruct the image. The echo train length refers to the number of k-space lines acquired after the excitation pulse.

2.5 Diffusion theory and measurement

The effect of diffusion was known in MR measurement since its beginning. It was treated as an unwanted effect. The random motion of particles, called also the Brownian motion, is the origin of diffusion that is typically measured in the brain. Spin motion inside the voxel volume in a presence of magnetic field gradient de-phases them. While moving, spins experience different magnetic field strengths during the gradient duration. The path length of the spin traversing during a typical MR measurement is much shorter than the dimensions of the imaged voxel.

Diffusion weighted imaging (DWI)

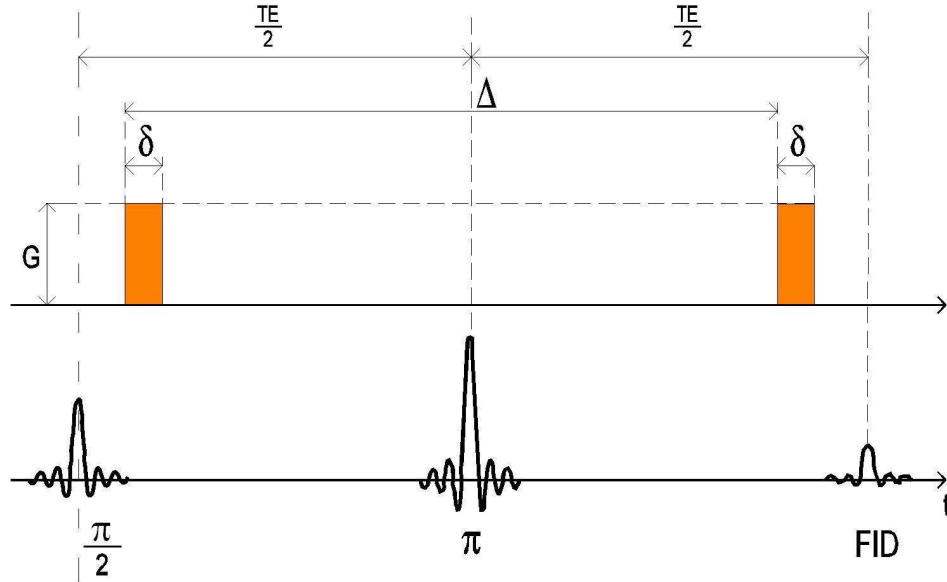


Figure 2.8. Draft of a simple diffusion sequence without imaging gradients. G - gradient strength [$\frac{mT}{m}$]; RF - Radiowave pulses emitted [mV]; FID - signal of free induction decay.

The images obtained with sequences containing diffusion gradients in general are called *diffusion weighted images (DWI)*. The simplest diffusion sequence (figure 2.8) consisting of a $\frac{\pi}{2}$ -excitation pulse, a π -re-focusing pulse and two gradients played between those pulses and between the last pulse and the spin-echo. To induce the diffusion spin coherence loss, additional gradients are applied with the duration of δ . Those gradients often are called *diffusion gradients*. The time from the beginning of the first gradient to the beginning of the second one is labeled Δ .

In the simplest situation, an excited spin is located in the origin of coordinate system. After time δ it reaches position z_1 , and after time of $\Delta + \delta$, the position z_2 .

The phase (ϕ_1) of the excited spin change when field gradient is applied (duration of δ), according with the following equation:

$$\phi_1 = \gamma \int_0^{\delta} \mathbf{G} z dt = \gamma G \delta z_1 \quad (2.20)$$

It is an integral over the duration of the first gradient and the phase change is proportional to the gradient amplitude and the spin position. When the spin is moving in the gradient field, it is experiencing different magnetic strength. It is worth to notice that only motion parallel to the direction of the gradient plays a role. Any perpendicular motion will not affect the spins phase.

Second gradient is played to reverse de-phasing of the spins caused by the first gradient. An inverse pulse (RF) was applied in the meantime, so the second gradient have the same amplitude and duration as the first one. This means, the spin phase given by the first gradient are reversed. It is also described by an integral:

$$\phi_2 = \gamma \int_{\Delta}^{\Delta+\delta} \mathbf{G}z dt = \gamma G \delta z_2 \quad (2.21)$$

Due to π -pulse between the gradients, the spin phase was inverted:

$$\varphi_1 \Rightarrow -\varphi_1 \quad (2.22)$$

The measured signal depends on the sum of phases of all spins. When the influence of relaxation is omitted, than the measured signal is proportional to the number of spins in the system:

$$S_0 = \mu \left| \sum_{j=0}^N e^{i\varphi} \right| \quad (2.23)$$

In an ideal case when spins did not move along the gradient direction. In this case, those two phases add and because z_1 and z_2 are equal then the integral spin phase change due to diffusion gradients is zero.

$$\varphi = \varphi_1 + \varphi_2 = \gamma G \delta (-z_1 + z_2) = 0 \quad (2.24)$$

Therefore, the eq. 2.23 take a simple form shown below. In this case, the signal is maximal, because there is no attenuation due to the diffusion.

$$S_0 = \mu N \quad (2.25)$$

The second option is when the position of the spin was not constant. The eq.2.24 is not equal to zero, moreover it is different for each spin and it depends on the path of the spin. In this case the signal is depending on the average phase shift:

$$S = \mu \left| \sum_{j=0}^N e^{i\varphi_j} \right| \quad (2.26)$$

When a large distribution of phases is taken into account, the total measured signal in MR experiment is proportional to the integral over probability density function (PDF), here denoted as $P(z_2|z_1, \Delta)$. This function describes what is the probability of finding spin at position z_2 , originating from position z_1 after time period of Δ .

$$S(\Delta, z_1) = S_0 \int e^{i\gamma G \delta (z_2 - z_1)} P(z_2|z_1, \Delta) dz_2 \quad (2.27)$$

The probability $P(z_2|z_1, \Delta)$ describes how the particles move in the space. It is a continuous function in 3D space. Usually, the P-function is presented as a 3D shape of point the the same probability of finding a particle diffusing from the origin. The shape is describing a relative extent of spins motion. In the case of free diffusion this shape is a sphere,

because the particle will travel with the same probability in all directions. In the case of obstacles or non-uniform medium the shape will differ. The shapes of iso-probability functions are very important for all diffusion methods. The fiber direction extraction will be discussed further on.

Each measurement (S), with a specific diffusion gradient, will give a projection of P-function depending on the gradient (\mathbf{G}) strength and direction. Currently, there exist two general approaches to this problem. First, it is to assume a type of P-function described by a set of parameters and then to calculate these parameters through the measurements. The diffusion process is described by a second order, symmetric and positive tensor. Therefore, a P-function described by the Gaussian distribution with a tensor as a parameter is the most natural choice:

$$P(\mathbf{r}, t) = \frac{1}{(4\pi t |\mathbf{D}|)^{\frac{3}{2}}} e^{-\frac{\mathbf{r}^T \mathbf{D} \mathbf{r}}{4t}} \quad (2.28)$$

where \mathbf{r} is position, t is time and \mathbf{D} is a second order tensor of diffusion.

The method of retrieving tensor components is described in the next subsection. The second approach is to measure the P-function directly. This method uses the fact that the P-function in eq.2.27 has a Fourier relation to the signal $S(\Delta)$. Similarly like in imaging, where the k-space has to be Fourier transformed to obtain the result in space domain, here the P-function can be achieved by a Fourier transform of measurements in the space of changing gradient amplitudes and directions. Such a space was named q-space [6].

Apparent diffusion coefficient

Each voxel of a DWI image is expressed by eq.2.29. Two compartments can be seen. The S_0 signal depends on the sequence type and timing. As it was mentioned earlier, the MR signal returns to the equilibrium and the diffusion gradients provide additional signal loss. It is therefore important to start data acquisition as soon as it is possible in order to obtain high enough signal-to-noise ratio. Necessary TE times make the contrast on images T_2 -dependent and in the case of single shot sequences T_2^* dependent (see eq.2.19).

$$S = S_0 e^{-(\gamma \delta G)^2 \Delta (ADC)} = S_0 e^{-b(ADC)} \quad (2.29)$$

$$b = (\gamma \delta G)^2 \Delta \quad (2.30)$$

$$ADC_i = \mathbf{q}_i^T \mathbf{D} \mathbf{q}_i \quad (2.31)$$

The diffusion attenuation part of eq.2.29 is connected to the parameters of the diffusion gradients (the amplitude(\mathbf{G}), duration(δ), gap between gradients(Δ), direction(\mathbf{q})). ADC is the *apparent diffusion coefficient*, which is a diffusion coefficient measured along a direction defined by the gradient \mathbf{G} .

All sequence gradients parameters, except those describing the direction are denoted by a new parameter b , called a *b-value*. This coefficient describes the strength of the diffusion weighting with the specified gradient duration and configuration and allows keeping the same diffusion weighting when different gradient directions applied.

Analyzing further eq.2.29, a higher b-value can be achieved by increasing gradient strength or by elongation of gradient duration or by increasing the gap between diffusion gradients. Regarding the whole imaging process, only an increment of gradient amplitude will not provide a signal-to-noise ratio penalty, by longer TE times.

$$\frac{S}{S_0} = e^{-b(ADC_i)} \quad (2.32)$$

To obtain an information only about the diffusion, the measured S signal has to be divided by signal measured without diffusion gradients, but with all sequence timing kept exactly the same. (i.e. $\mathbf{G} = 0$) The attenuation of S_0 signal can be described by the projection of the gradient direction on the diffusion tensor. In the eq.2.32, the ADC can also be denoted as a projection of diffusion tensor on the direction (\mathbf{q}) of the gradient \mathbf{G} :

$$ADC_i = \frac{\ln\left(\frac{S_i}{S_0}\right)}{b_i} \quad (2.33)$$

The apparent diffusion coefficient shows the amount of diffusion in a given direction in space. The tensor \mathbf{D} has six independent components. This equation system has 6 unknown variables; therefore, at least six non-collinear equations have to be found. Each measurement performed gives one equation (using eq.2.33) and the S_0 has to be known additionally to remove T_2^* contrast.

2.5.1 Diffusion Tensor Imaging

The intensity on the images depends on the T_2 -relaxation time and moreover on the attenuation by the diffusion process. The measured signal without diffusion gradients, according to eqs.2.23 and 2.26, is always greater than with the diffusion gradients enabled. The previous section described the general idea of diffusion weighting of an image. Following sections describe how directional information can be extracted from multi-directional acquisition.

The MR signal attenuation and consequently the diffusion coefficient D from the eq. 2.28 depend on the gradient direction.

The level of attenuation for each direction can be estimated using $P(\mathbf{r}, t)$ from eq. 2.27.

In principle, there are two approaches for obtaining P . One can assume some diffusion model with certain number of freedom degrees. The measurements with different diffusion gradients will allow to find all unknown parameters of the model and to find the function P . Alternatively, a large number of measurements can, with certain accuracy, directly show the function P .

In the case of diffusion tensor imaging the P -function is assumed to be an unknown symmetric, positive second order tensor \mathbf{D} and it describes the properties of the diffusion process. Diagonal elements of the tensor describe the diffusivity, projected on the axes of the laboratory reference frame. Off-diagonal elements describe the correlation between diffusion coefficients located on the diagonal. Since the diagonal elements projects on axis of the reference frame, the maximal value of the diffusion coefficient may not be revealed. The reference frame can be changed by applying rotation transformation to the values of the tensor components.

For each tensor there exists such a rotation matrix that the off-diagonal elements become zero after the rotation. This means the tensor can be rotated to such a unique reference frame that diagonal components do not correlate between each other (i.e. they are independent). The operation to find the rotation matrix is called *the general eigenvalue problem*. The diagonal values of rotated tensor are called *eigen-values* ($\lambda_1, \lambda_2, \lambda_3$) and the unit vectors of the new reference frame are named *eigen-vectors* ($\varepsilon_1, \varepsilon_2, \varepsilon_3$). The vectors form a rotation matrix that transforms the eigen-values into laboratory reference frame. The eigen-vectors are orthogonal and the one correlated to dominant eigenvalue points the directions of diffusion. The magnitude of that diffusion is described by the eigen-values.

The general eigen-value problem can be written as:

$$\forall_{x \neq 0} \exists_{\lambda, \epsilon \neq 0}, \mathbf{D}x = \lambda \epsilon x \Rightarrow (\mathbf{D} - \lambda \epsilon)x = 0, \text{ since } x \neq 0, \text{ therefore } \mathbf{D} = \lambda \epsilon \quad (2.34)$$

The explicit form of the final eq.2.34 is given below:

$$\begin{bmatrix} D_{xx} & D_{xy} & D_{xz} \\ D_{xy} & D_{yy} & D_{yz} \\ D_{xz} & D_{yz} & D_{zz} \end{bmatrix} = \begin{bmatrix} \lambda_1 & 0 & 0 \\ 0 & \lambda_2 & 0 \\ 0 & 0 & \lambda_3 \end{bmatrix} \begin{bmatrix} \epsilon_{1x} & \epsilon_{1y} & \epsilon_{1z} \\ \epsilon_{2x} & \epsilon_{2y} & \epsilon_{2z} \\ \epsilon_{3x} & \epsilon_{3y} & \epsilon_{3z} \end{bmatrix} \quad (2.35)$$

The eigen-value λ_1 is a diffusion coefficient in the direction of eigen-vector ϵ_1 and respectively λ_2 and λ_3 show the diffusion coefficient in the directions of ϵ_2 and ϵ_3 . The tensor is very often visualised as an 3D ellipsoid (eq.2.36). The lengths of main axis are scaled to the eigen-values and the axes are parallel to the eigen-vectors.

$$\frac{x^2}{\lambda_1^2} + \frac{y^2}{\lambda_2^2} + \frac{z^2}{\lambda_3^2} = 1 \quad (2.36)$$

Such an approach allows to present the proportions between the diffusion coefficients and the directions of the diffusion process. The decomposition of the tensor into eigen-

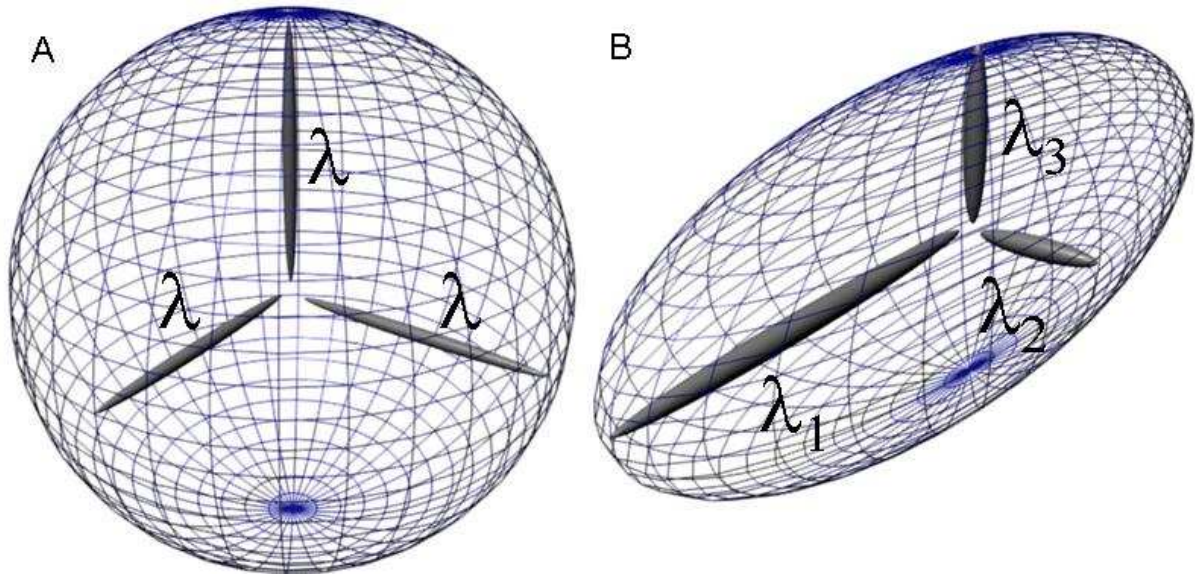


Figure 2.9. Two ellipsoid representing free and restricted diffusion. a) Free diffusion where all λ s are equal, ellipsoid has a shape of a sphere. b) Restricted diffusion, one eigenvalue (λ_1) dominates over the others.

values and eigen-vectors is so important, because the direction in which the diffusion is not restricted. It is described by the eigenvector of the dominant eigenvalue. The eigenvector which corresponds to maximal (main) eigenvalue directly points the direction of the most efficient particle motion.

The ADC_i (eq.2.31) can be expressed as $\mathbf{q}_i^T \mathbf{D} \mathbf{q}_i$ where i is the number of measurement. It is possible to write the general form of the relation, that contains all measurements ($i=1,2,\dots,n$):

$$\mathbf{y} = \mathbf{X} \mathbf{D}' \quad (2.37)$$

where:

$$\mathbf{y} = [ADC_1 ADC_2 \dots ADC_n]^T \quad (2.38)$$

$$\mathbf{D}' = [D_{xx} D_{yy} D_{zz} D_{xy} D_{xz} D_{yz}] \quad (2.39)$$

$$\mathbf{X} = \begin{bmatrix} q_{1x}^2 & q_{1y}^2 & q_{1z}^2 & 2q_{1x}q_{1y} & 2q_{1x}q_{1z} & 2q_{1y}q_{1z} \\ \vdots & & & & & \\ q_{nx}^2 & q_{ny}^2 & q_{nz}^2 & 2q_{nx}q_{ny} & 2q_{nx}q_{nz} & 2q_{ny}q_{nz} \end{bmatrix} \mathbf{q}_i = [q_{ix}, q_{iy}, q_{iz}] \quad (2.40)$$

The vector \mathbf{y} is built out of measured ADCs and it is equal to a product of matrix \mathbf{X} , which elements contain information about the diffusion directions and the unknown tensor components (\mathbf{D}'). Each measurement has some uncertainty and assuming tensor may not fully reflect the reality; therefore, some small part has to be added to balance the equation.

Now, when the relation between the measurements and the tensor is known, it is possible to estimate the unknown tensor components. There have to exist such a $\hat{\mathbf{d}}$ that would be an inversion to the equations above. The tensor components could be calculated with an error of e' by:

$$\mathbf{D}' = \hat{\mathbf{d}}\mathbf{y} + e' \quad (2.41)$$

The matrix $\hat{\mathbf{d}}$ can be estimated with numerical methods. This solution is called *Moore-Penrose pseudo-inversion* [10],[11] after the inventors and it is given by:

$$\hat{\mathbf{d}} = (\mathbf{X}^T \mathbf{X})^{-1} \mathbf{X}^T \quad (2.42)$$

To obtain the final 3x3 tensor form, the \mathbf{D}' components have to be placed in the following way:

$$\mathbf{D} = \begin{bmatrix} D'_1 & D'_4 & D'_5 \\ D'_4 & D'_2 & D'_6 \\ D'_5 & D'_6 & D'_3 \end{bmatrix} \quad (2.43)$$

Matrix $\hat{\mathbf{d}}$ is in practice, estimated by a numerical fit. Therefore, it is sensitive to noise issues. To effectively decrease the error of estimation e' , it is important to provide high SNR images and to provide not only non-collinear diffusion gradients, but their directions should be equally distributed on a sphere [12].

The tensor characterizes the diffusion in a given voxel (see eq.2.35). However, it is difficult to present the tensor characteristics of all voxels as an easy-to-read image, since it has nine components. To achieve this aim several scalar parameters were proposed; their significance lies in being rotationally invariant and independent of the sorting of the eigenvalues. Rotational invariance states that such measure is independent of the orientation of the diffusion ellipsoid. In general, the tensor can be decomposed into an isotropic and an anisotropic component. The isotropic component is characterized by the so-called trace of the diffusion tensor and is proportional to the sum of square of radii of the diffusion ellipsoid:

$$\text{Tr}(\mathbf{D}) = \lambda_1 + \lambda_2 + \lambda_3 = D_{xx} + D_{yy} + D_{zz} \quad (2.44)$$

The most commonly used scalar measure of anisotropy is the *fractional anisotropy*. It is a ratio between the standard deviation and root mean square of eigenvalues (eq.2.45). This way it is restricted and normalized to $< 0; 1 >$ range. In the case of isotropic diffusion all eigenvalues of the tensor are equal, so the standard deviation is zero. The FA equal to zero represents same diffusion in all directions. In the case of strongly anisotropic

diffusion, as one of the eigenvalues is much greater than others, the FA approaches the value of one.

$$\text{FA}(\mathbf{D}) = \sqrt{\frac{\sum_{i=1,2,3} (\lambda_i - \bar{\lambda})^2}{\frac{3}{2} \sum_{i=1,2,3} \lambda_i^2}} \quad (2.45)$$

The factor of $\frac{3}{2}$ corrects the standard deviation in the case of only 3 samples. Fractional anisotropy is a rotational invariant index.

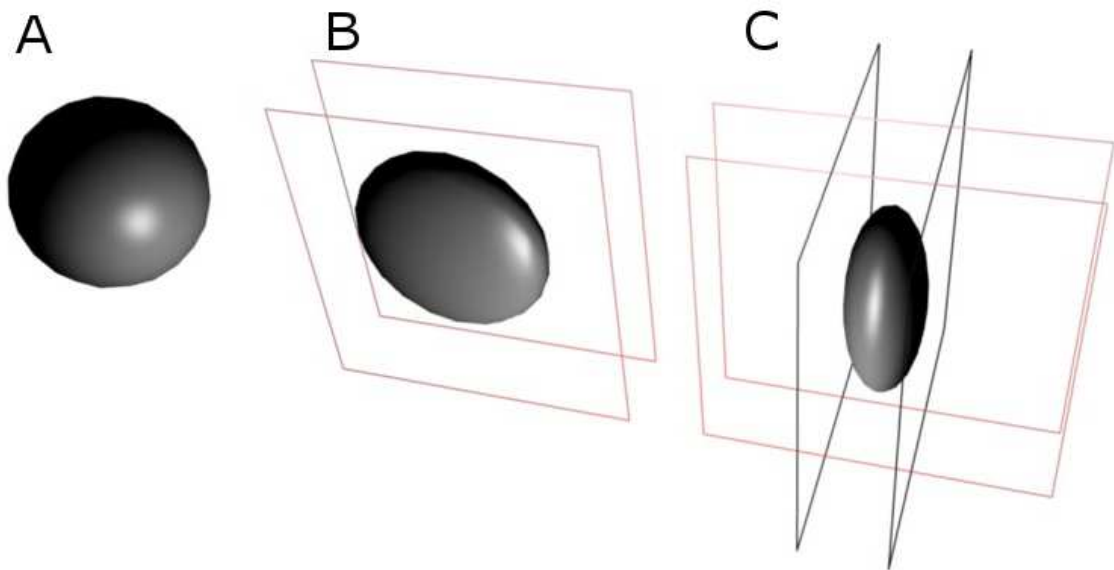


Figure 2.10. Diffusion tensor ellipsoids. a) unrestricted diffusion, b) diffusion restricted in single direction, c) diffusion restricted in two orthogonal directions.

In media where no obstacles are found, the diffusion process has the same properties in all directions. In that case tensor \mathbf{D} consists of three equal eigenvalues. This case is referred as *free diffusion* and it is enough to know diffusion coefficient D , instead of whole tensor \mathbf{D} . The tensor ellipsoid is a sphere as shown in figure 2.10a.

In all other cases *restricted diffusion* occurs. In this case, diffusion coefficient is a function of direction in the space. In this model, it was assumed that the function can be approximated by a tensor. If the diffusion is restricted in a single direction, then the ellipsoid has a disc shape (figure 2.10b). In other words, diffusion occurs with fewer obstacles in plane.

A cigar shape of the tensor (figure 2.10c) can be found where only one direction of diffusion is privileged and all others are restricted.

2.5.2 Q-space description and Diffusion Spectrum Imaging

The term *q-space* in relation to MR measurements appeared for the first time in 1990 and was introduced by Callaghan [13] for porous media measurements. Next, velocity measurements were performed by Xia and Callaghan [14]. In 1994, the idea of q-space brain measurements was suggested by King et al. [15].

To describe the idea behind the q-space measurements, one can remove the T_2^* depen-

dency in eq. 2.27, by calculation the ratio:

$$\frac{S}{S_0} = \int e^{ib(z_2-z_1)} P(z_2|z_1, \Delta) dz_2 \quad (2.46)$$

In this way the PDF function is in Fourier relation with the measurement. Let us take a general expression for a Fourier transform:

$$\hat{f}(\omega) = \int_{-\infty}^{\infty} f(t) e^{-i\omega t} dt \quad (2.47)$$

$P(z_2|z_1, \Delta)$ can be retrieved using an inverse Fourier Transform on measured data over the measured and normalized data. The time t can be replaced by position z and the frequency ω in our expression is a factor $b = -\gamma G \delta$. The last factor contains information about the amount of diffusion weighting present in the signal.

$$P(z_2|z_1, \Delta) = iFFT \left(\frac{S}{S_0}(\mathbf{q}, b) \right) \quad (2.48)$$

With such a similarity to Fourier transform, same approach as in the case of imaging can be used, since temporal MR signal is in Fourier relation to the image. In imaging there is a term of k-space. It is a Cartesian grid, where temporal measurement points are located. Each axis is described by the time units and after Fourier transform of k-space an image is produced. Analogical in the case of diffusion, the space where measurements are placed is called q-space. The axes of this space are described by the strength of diffusion weighting gradients in the base directions. As described in section about DTI, the diffusion weighting is built by gradient amplitude, duration and gap between diffusion gradients. The position of MR measurements in the q-space is described by the directions of the gradients. The radius describes the amount of diffusion weighting (b-values). Vector $\mathbf{b}(b_x, b_y, b_z)$ uniquely describe position in q-space. In the origin of q-space (i.e. $\mathbf{b} = 0$) the un-weighted S_0 is located.

Unfortunately in diffusion spectrum imaging, the measurements are much more difficult than the mathematical framework for reconstruction. As in the case of imaging, the details are located off-centre of the k-space. To obtain detailed information about the PDF function, measurements of high b-values are required. This is different from DTI approach where usually one b-value was acquired in different diffusion directions (at least six). To perform discrete Fourier transform on measured data a Cartesian grid of samples is needed. A grid of 16x16x16 results in 4096 measurements, using half of that resolution i.e. 8x8x8 results in 512 measurements, which is a large number for an *in vivo* study. The measurements of high b-values are yet another obstacle. Due to hardware limitations of gradient system, the time required to build b-value is much longer than T_2^* . Building b-value of 8000 and takes more then 300 ms and T_2^* for 3 T systems is around 63 ms. This fact is raising SNR issues in the images with high b-value. Nevertheless, such approach can be used for samples, phantoms, etc. This straight-forward measurement of PDF in known as Diffusion Spectrum Imaging (DSI).

Figure 2.11 shows a typical sampling scheme in DSI experiment. Each point represents a single MR measurement with diffusion weighting. The vector from the origin of q-space to measurement point defines the diffusion gradient direction and the vector length is the b-value that has to be used in MR sequence. Note that b-values are measured up to 4000 $\frac{s^2}{mm}$, but in some experiments they can be much higher, even up to 20000 $\frac{s^2}{mm}$ [6]. Figure 2.11b shows a cross-section for b_z -value = 0 where the Cartesian grid can be clearly seen. This plot can be compared to trajectory plotting in k-space for imaging.

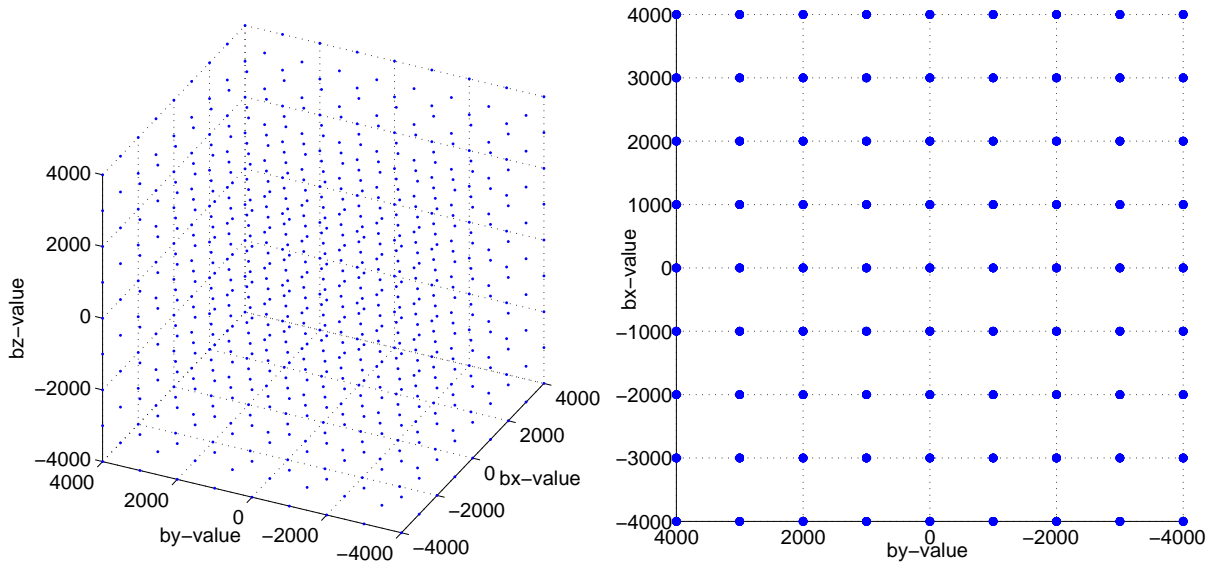


Figure 2.11. Q-space. A typical sampling scheme in DSI experiment. left) 3D visualisation of measurement points, right) cross-section through the $b_z = 0$ plane.

After inverse Fourier transform, obtained PDF can be transformed into a *spin displacement orientation distribution* (ODF) [6]. The transformation is done through a radial projection of the PDF on the sphere. In practice a given point of projection can be calculated as an integral along radius:

$$\text{ODF}(\theta, \varphi) = \int_0^{\infty} \text{PDF}(R, \theta, \varphi) dR \quad (2.49)$$

At the end, fiber tracking algorithms are interested in just the directions and this information can be obtained more efficiently by reducing one dimension. ODF contains also information about diffusion strength, since fiber population with higher anisotropy would have higher integral values. By this way a three dimensional PDF function is reduced into a two-dimensional map. The problem of diffusion directions description comes down to the finding of local maxima on 2D map.

Figure 2.12 shows signal intensities from a simulated measurements of two crossing fibers populations each having FA of 0.75. Since it is a simulation the noise is not present. Each voxel have intensity proportional to the amount of signal measured in a specific position in q-space (see figure 2.11) Lower row in the figure shows a result of discrete Fourier transform over the measurements. As assumed obtained PDF function shows two distinct directions of diffusion.

Concluding, the advantages of DSI are exact, precise and direct measurement of PDF function and easy to handle transformation of measurement data. Very long measurement time and complex sampling scheme with multiple b-values and sequence timings make this approach hard to implement in *in vivo* and clinical measurements.

2.5.3 Q-ball imaging

The DSI approach showed that it is in principle possible to directly measure PDF function *in vivo*. The methods that followed DSI are trying to reduce time of acquisition in order to obtain diffusion information from as large volume as possible. In the previous section the PDF function was projected on the sphere in order to facilitate analysis. The main idea behind the q-ball imaging is to obtain directly ODF i.e. radial projection of PDF.

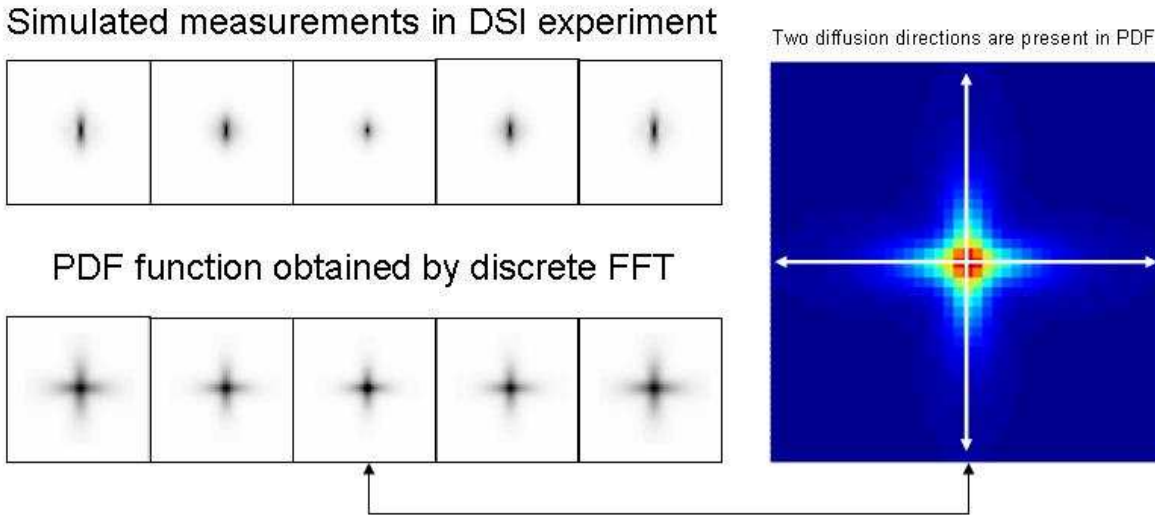


Figure 2.12. An example of DSI measurement and a PDF function obtained by Fourier transform. Selection of planes in q -space and PDF was shown on the left side. On the right side a slice from PDF is shown from the center of space with clearly visible two peaks of higher diffusion.

This way less information is required, but the key features remain (diffusion directions and strengths of fiber populations).

It was proven [6] that the ODF function described as in eq.2.49 can be estimated through the Funk-Radon transform (FR) from the measured diffusion weighted images ($E(\mathbf{q})$). The ODF function can also be described as a convolution of the PDF and a zeroth-order Bessel function (J_0) [5].

$$\text{ODF}(\mathbf{u}) \cong \text{FR}(E(\mathbf{u})) = 2\pi q' \int P(r, \theta, z) J_0(2\pi q' r) r dr d\theta dz \quad (2.50)$$

The Funk transform is a generalization of the Radon transform to the sphere. In practical implementation, a given point of the ODF-function, which is referred as the pole, has a value of the integral over the equator laying on the perpendicular plane. Since Funk-Radon transform maps function described on the sphere to functions on the sphere, the acquisition in the q -space have to be performed on the sphere as well. An example of the sampling scheme in q -space is shown in figure 2.13a. A set of 252 points was equally distributed on the sphere, by five-fold tessellation of icosahedrons. The density of the measurements remains the same in all parts of the sphere. In this example, b -value (sphere radius) is set to $1500 \frac{s^2}{mm}$.

The gaps between the measurement points in figure 2.13a have to be filled by interpolation. Diffusion coefficients from experiment can be integrated by interpolation of the measurement on the reconstruction circle. In figure 2.13b the reconstructed point is marked by an arrow. The PDF projection from eq.2.50 can be obtained by calculation an integral over ADCs located on the equator (yellow stripe).

The ADC measured on a sphere in q -space is transformed into a sphere of radial projection of PDF. The maxima in ODF-function which are called q -ball shapes are extracted using an iterative algorithm. Starting from a random seed point, it is advancing towards the direction of the maximal gradient of ODF function. The procedure is repeated for a hundred times starting from a different seed point each time. In this way, algorithm is independent of seed point position. The resulting directions are grouped into distinct directions of diffusion present in the ODF shape. Each maximum is treated as direction of

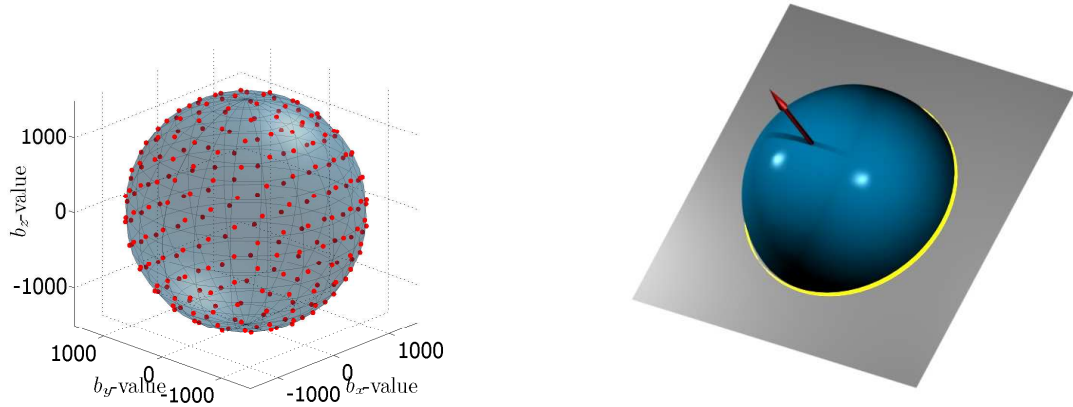


Figure 2.13. Q-ball experiment. left) An example of q-space with 252 measurement points located in a sphere. right) The idea of Funk-Radon reconstruction. Value of ODF function in direction marked by the red arrow is calculated as integral over perpendicular equator – a yellow stripe.

diffusion. The principal diffusion direction in q-ball shape is the direction of the maximum with the highest value of ODF.

The general fractional anisotropy (GFA) for q-ball reconstruction is defined as a ratio between standard deviation and the root mean square of ODF values [6]:

$$\text{GFA} = \frac{\text{std}(\text{ODF}(\mathbf{r}))}{\text{rms}(\text{ODF}(\mathbf{r}))} = \sqrt{\frac{n}{n-1} \frac{\sum_{i=1}^n (\text{ODF}(\mathbf{r}_i) - \langle \text{ODF}(\mathbf{r}) \rangle)^2}{\sum_{i=1}^n \text{ODF}(\mathbf{r}_i)^2}} \quad (2.51)$$

The GFA is derived in the same way as in the DTI, where FA is a ratio between standard deviation and the root mean square of eigenvalues found in the tensor. The eigenvalues can be treated as projections of ellipsoidal PDF in orthogonal directions of the tensor coordinate system. In the DTI those three values describe in unique way diffusion, but here whole ODF function has to be taken into account [6].

Concluding, data for a q-ball reconstruction can be measured faster than for DSI, b-value is constant and we still do not need any model of diffusion. Disadvantage of this method is that only radial projection of PDF can be found and moreover obtained ODF is convoluted with a Bessel function.

2.5.4 Spherical harmonics de-convolution

In q-ball imaging, the acquisition time is counted in minutes per one average. Standard brain acquisition, which is 40 slices with 252 diffusion directions, takes 30 minutes. Further development of reconstruction methods is still focusing on radial projection of PDF, but to save time, the number of measuring points is reduced. The missing information is replaced by assumptions.

Multiple reconstruction methods were proposed: q-ball by persistent angular structure method (PAS-MRI [16]), diffusion orientation transform (DOT [17]) and spherical harmonics deconvolution (SD) [18]. All of them reduce number of points in q-space.

In this thesis, the spherical harmonics deconvolution was chosen as an alternative method for ODF function estimation, because of its speed of reconstruction and significant reduction of data volume required for computation and storage, when compared to Funk-Radon reconstruction of q-balls.

In SD the measured signal is assumed to be a sum of the response functions of each fiber population present in the voxel, weighted by their respective fractions. Like in

q-ball reconstruction signal is measured on the sphere in the q-space with a constant b-value. Therefore, the measured signal can be represented in spherical coordinates $S(\theta, \varphi)$. The response function ($R(\theta)$) represents a signal that would be measured from fibers pointing to a single direction without influence of the noise. We assume that only one unique response function exists. The function $R(\theta)$ can be simulated or measured directly. Measurement should take place from a part of the brain that has fibers going in the same direction. Therefore, the signal in this experiment is given by:

$$S(\theta, \varphi) = \sum_i f_i \hat{A}_i(\theta, \varphi) R(\theta) \quad (2.52)$$

factor f_i describes volume fraction of i-th fiber population and \hat{A}_i is a rotation operator. Equally, it can be expressed as the convolution over the unit sphere of response function $R(\theta)$ with a fiber orientation density function $F(\theta, \varphi)$:

$$S(\theta, \varphi) = F(\theta, \varphi) \otimes R(\theta) \quad (2.53)$$

The fiber orientation density function, described here, is not a radial projection of PDF. This function has everywhere value of 0 except for θ, φ that show directions of diffusion. In other words, it is a sum number of Dirac delta functions pointing along the direction of each fiber population, weighted by respective volume fraction.

If the response function $R(\theta)$ is known, then the fiber orientation $F(\theta, \varphi)$ can be obtained by performing spherical de-convolution of $R(\theta)$ from $S(\theta, \varphi)$. In spherical coordinates, the spherical harmonics form an orthogonal set of basis functions. They are described by harmonic order n ($n \geq 0$) and phase factor m ($-n \leq m \leq n$). Harmonics with even n are symmetric functions and ones with odd n are anti-symmetric. Any function, described over the sphere, can be represented by orthogonal spherical harmonics ($n=\infty$). For finite n is an approximation.

The spherical convolution operation can be formulated as the action of an ensemble of rotations (corresponding to the convolution kernel) on a function defined over a sphere [19]. The n-th order spherical harmonic representation of $S(\theta, \varphi)$ can be expressed as:

$$S^n = \mathbf{R}^n \mathbf{F}^n \quad (2.54)$$

where \mathbf{F}^n is a $(2n+1)$ vector, representing the n-th order spherical harmonic decomposition of $F(\theta, \varphi)$ and \mathbf{R}^n is a $(2n+1)$ by $(2n+1)$ matrix representing the n-th order rotational harmonic decomposition of $R(\theta)$. Because the diffusion process is symmetric about the origin, all odd components have to be zero. The spherical harmonic representation of measured signal \mathbf{S}^n can be calculated by linear least squares fit [20] and fiber orientation function \mathbf{F}^n can be obtained by inverting \mathbf{R}^n .

The higher maximal order of spherical harmonics used, the more reliable estimation one can obtain. For $n_{max} = 8$, there are 45 independent parameters; therefore, sampling scheme must contain at least 45 non-collinear directions. For $n_{max} = 10$, the minimum number of points in q-space is 66 and for $n_{max} = 12$, it is 91 measurements [18].

Concluding, the SD can reveal the most wanted information about the diffusion i.e. fibers direction and differences between population strengths. The time of acquisition can be shortened significantly, but decreasing maximal order of spherical harmonics would decrease reliability. Usually, response function is simulated using the tensor model or measured from *corpus callosum* (see fig. 2.15).

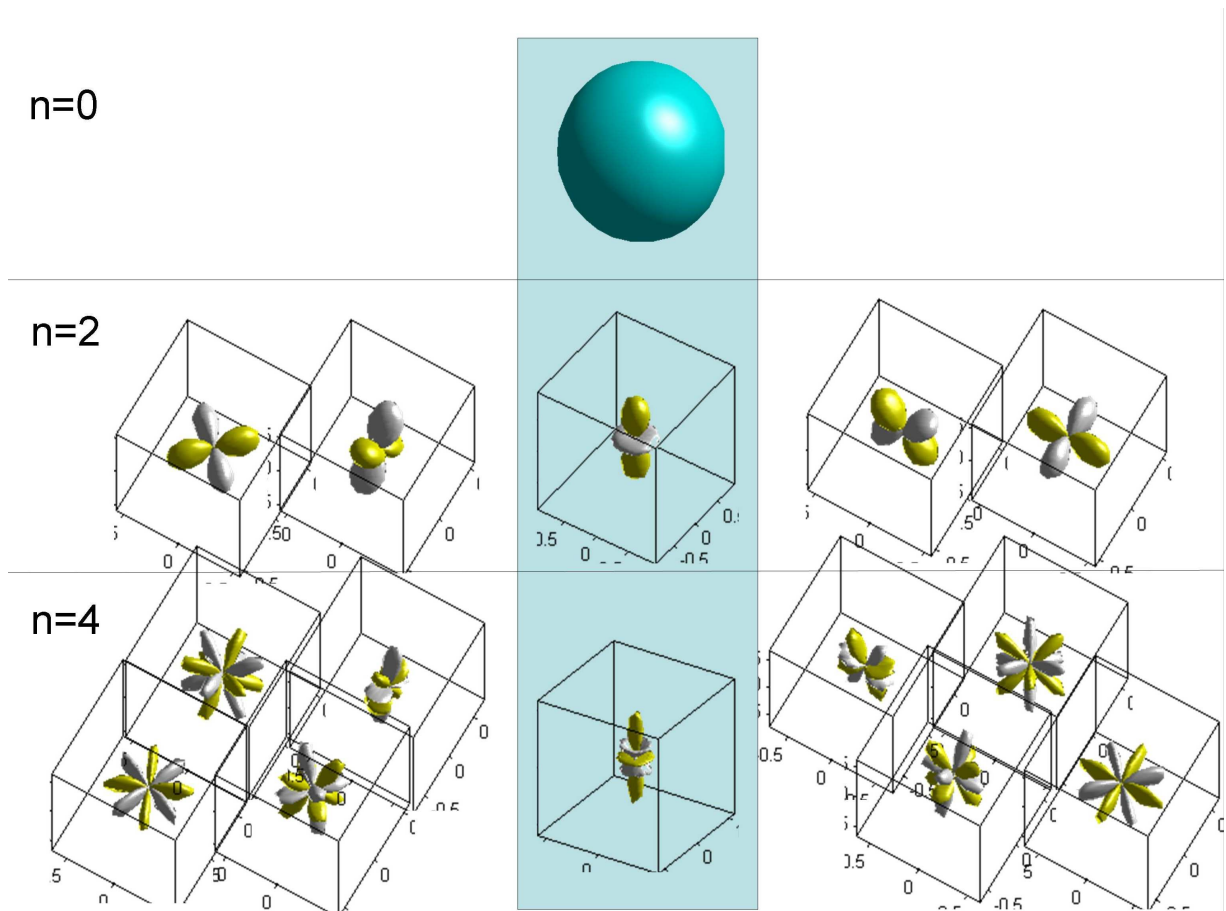


Figure 2.14. The base functions for spherical harmonics decomposition of 1st, 2nd and 4th order.

2.6 Anatomical origin of diffusion in human brain

The central nervous system is built by nerve cells and supporting glial cells. Beside the cell body, the nerve cell has a long fiber which connects it with other cells called *axon*. The brain is organized into two parts: grey and white matter (see figure 2.16). The grey matter contains mainly nerve cell bodies and the white matter is built by axons. Non-uniform diffusion properties (*anisotropy*) of the white matter can be explained by the water molecules motion restrictions. The axons are placed parallel one to each other like small tubes. The water molecules can go more easily in direction of the fibers than to any perpendicular one. The MR signal loss depends on the distance that a molecule can travel (eqs. 2.20 – 2.26), the attenuation of S_0 is greater when the direction of the diffusion gradient matches the local direction of the nerve axons.

2.7 Fiber tracking concepts and strategies

The origin of anisotropic properties of the white matter can be explained by collections of parallel axons, that restrict protons motion (see. 2.5.1). The fiber tracking (FTR) derives from this assumption. This method allows to reconstruct fiber tracts present in the white matter and predicts pathways that connect different regions of the brain. The FTR base on the information provided in diffusion measurements. When information about the diffusion is available, the directions of fiber population have to be extracted for each voxel of the white matter. In the case of DTI, it is the eigenvector direction of the largest eigenvalue. For q-space methods, ODF is calculated and the local maxima point

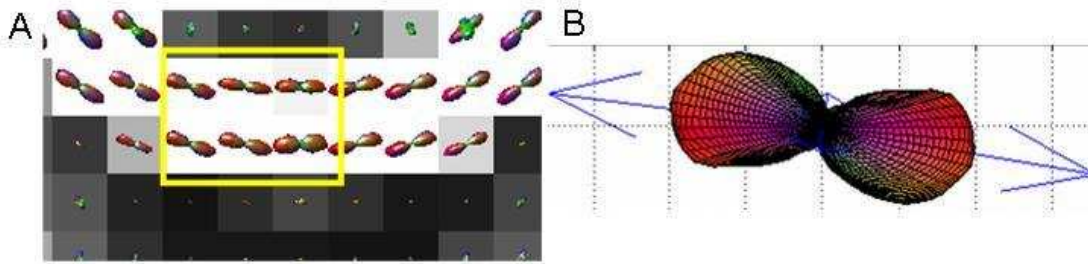


Figure 2.15. Measured data of a response function for spherical harmonics de-convolution. A) measurement of corpus callosum single fiber population (yellow box) B) extracted measurement of the response function.

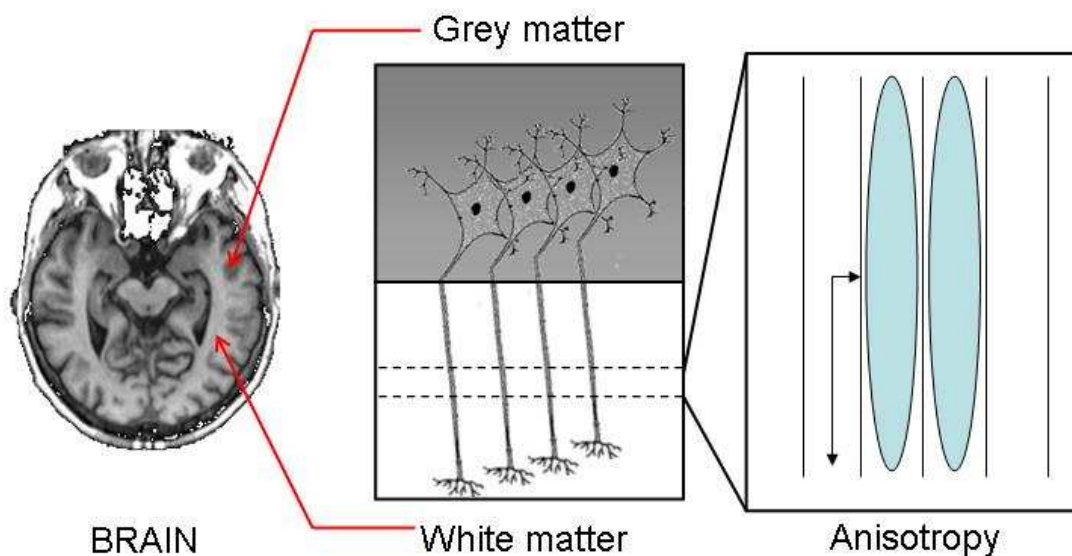


Figure 2.16. The origin of the anisotropy in the central nervous system. Left) MR scan of human brain with contrast exploiting differences between white and grey matters. Middle) Structure of grey and white matters. Right) The length of the free path in the presence of parallel obstacles.

the directions of fibers (more detailed information available in methods part).

The FTR can be divided into two main groups, regarding the output of the method. Deterministic fiber tracking uses diffusion information to reconstruct exact pathways from a starting region. It follows the measured directions of diffusion. The output of this method is a collection of paths connecting two points in the brain. In the probabilistic approaches the diffusion information is used as a background for a Monte-Carlo algorithm that calculates the diffusion direction in each position of the brain with given angle distribution. The process of fiber tracking is repeated many times from the same starting point, each time returning different, probable representation of fiber path. At the end the probable trajectories are counted and positions in the brain that contain larger number of path are described as more probable to contain fibers beginning at starting point. It is possible to divide destination area of the brain into logical regions and count trajectories that end there. In this way one can answer a question about which destination region is most likely connected to starting regions.

2.7.1 Deterministic Fiber Tracking

A streamline approach is very often used in reconstruction of fiber pathways. The fiber is reconstructed in small steps. The diffusion directions present in all voxels describe the next step direction. From an arbitrary chosen starting point the reconstruction algorithm walks along diffusion direction until a stop condition occurs.

Starting points usually are chosen using expert knowledge, when it is expected to find a known fiber bundle in selected region. Starting region can also be chosen on other measurement basis (e.g. fMRI). Special case of starting region is to select all voxels inside the white matter. The last case is usually referred as *brute force method*, because all possible trajectories are reconstructed. By this way, one has a possibility to analyze not only fiber tracts originating from the region, but also tracts that pass through the region. The choice of starting region may provide large bias into any quantitative analysis of obtained pathways, because the local FA value the white-grey matter border are low and provide uncertainty in direction estimation. On the other hand, choosing starting point in the middle of the track is difficult, since one do not knows where exactly it lays.

The streamline fiber tracking equation shown below (eq. 2.55) describe the reconstruction steps. Position of next point (X_{n+1}) of reconstructed fiber is calculated as current position (X_n) plus the diffusion direction (ε_n) found at the position of X_n and with a step length (Δx). The direction of diffusion is provided by DTI or HARDI methods.

$$\mathbf{X}_{n+1} = \mathbf{X}_n + \varepsilon_n \cdot \Delta x \quad (2.55)$$

The step length Δx of the algorithm is a very important factor in the equation. Too large value will mislead reconstruction, too small will create unnecessary data. Factor Δx do not have to be fixed value [21][22]. It can be scaled by the Fractional Anisotropy, coherence with diffusion neighbourhood. This way, when reconstructing through major fiber tracts with high FA, it can be done quicker, because reconstruction will move with less number of midpoints and in the case of small fibers close to grey matter, Δx can be shortened for higher accuracy[23].

The last operation is stopping the reconstruction. Termination of tracking should be performed when reconstruction is outside the white matter. No fibers are expected to be inside CSF or grey matter. These structures can be recognized by fractional anisotropy. Both, CSF and grey matter have very isotropic properties, so when FA is lower then some threshold level, there is no need to continue the reconstruction. The second reason to stop tracking is when the angle between diffusion directions of two successive steps is too wide. The nerves in brain are not prone to turn sharp at level typical resolution (1 – 3 mm).

Figure 2.17 shows a simple example of fiber tracking. For sake of simplicity, assuming to have only one diffusion direction per voxel, like in DTI. Yellow voxel was chosen as the starting point, so it is position X_0 in equation 2.55. In each step, algorithm moves along the directions, bending the trajectory. Finally in voxel marked blue, a stopping condition is met. If it moved forward, the angle between diffusion direction in two successive step would be around $\frac{\pi}{2}$. This is a reason to terminate reconstruction, as described above. The step size Δx is very important factor which have to be adjusted to the actual data resolution. Too big step size will result in a different trajectory, most probably false one. The trajectory that ends in green voxel was reconstructed with step size exceeding the voxel size. Due to increased step size algorithm rendered different trajectory. Small step size results in significant increase of computation time and large data size. Therefore, choice of step size is always trade between computation time and accuracy.

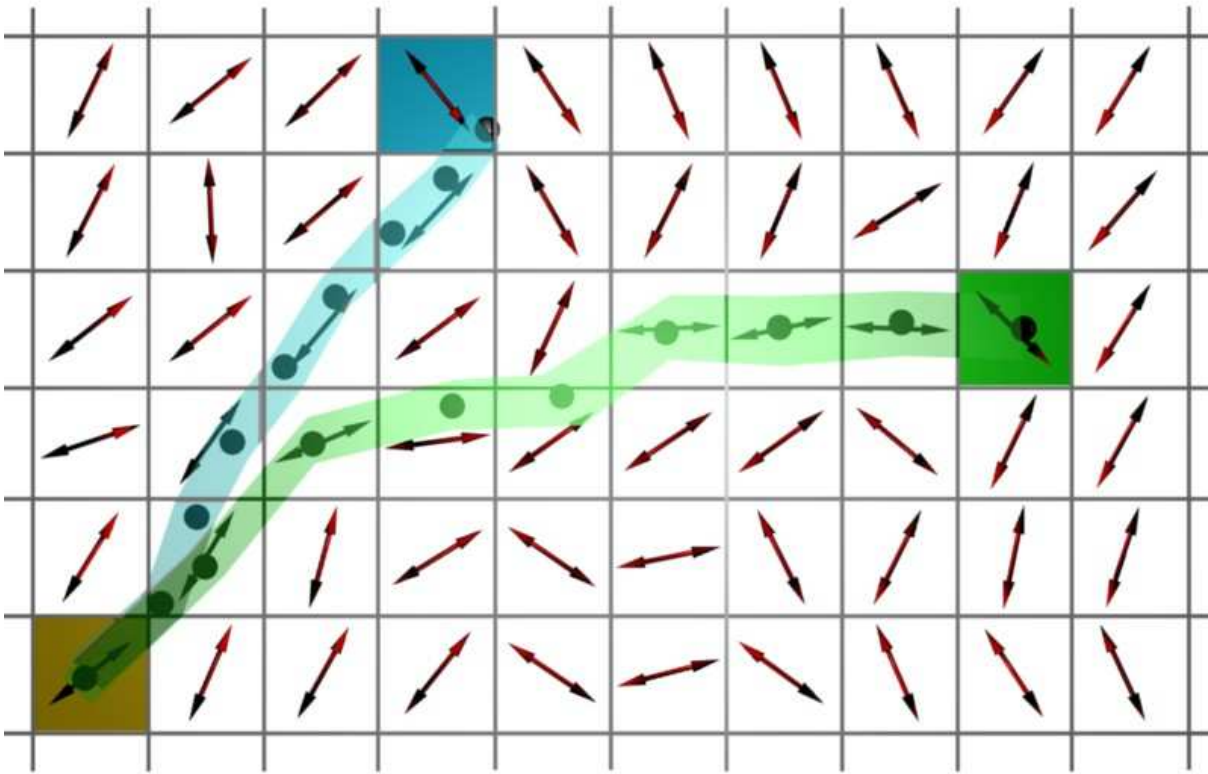


Figure 2.17. An example of deterministic FTR algorithm results. Starting point is marked in yellow, ending point in green and blue. A stripe represents the reconstructed trajectories in presence of a field of diffusion directions (red arrows). Trajectories were reconstructed with different step size. $0.75 \cdot \text{voxel size}$ (blue); $1.5 \cdot \text{voxel size}$ (green)

Second conclusion from this figure is that fiber reconstruction is not a reversible process. It is impossible to start a reconstruction from the ending point and reaches the starting point of previously reconstructed fiber. It is explained by the fact, that even if diffusion direction in voxel X_n points the voxel X_{n+1} , the voxel X_{n+1} can point other voxel on the way back. The discrete nature of the measurement makes it happen as well as low resolution in relation to sizes of imaged fiber structures.

In fiber tracking, there is also a major problem which is worth to be mentioned. DTI was not able to solve it. In figure 2.18 one can see the results from DTI presented as ellipsoids. The tensors have shapes of discs in the central region. Therefore, the direction of fibers is inconclusive. There are two solutions of this situation. One, seen on the left side, where the fibers meet in the central part, but they do not cross. This solution is usually referred as *fibers kissing*. On the left side, the same diffusion configuration leads to a solution where the fibers meet and cross from one side to another. This solution is often called *fibers crossing*. Even direct PDF estimation will not solve it, because PDF function in the central region will have the same shape. The *kissing-crossing* problem cannot be solved by any diffusion methods today. It seems that the only the solution is to refine resolution, but this also have physical limits way above required level.

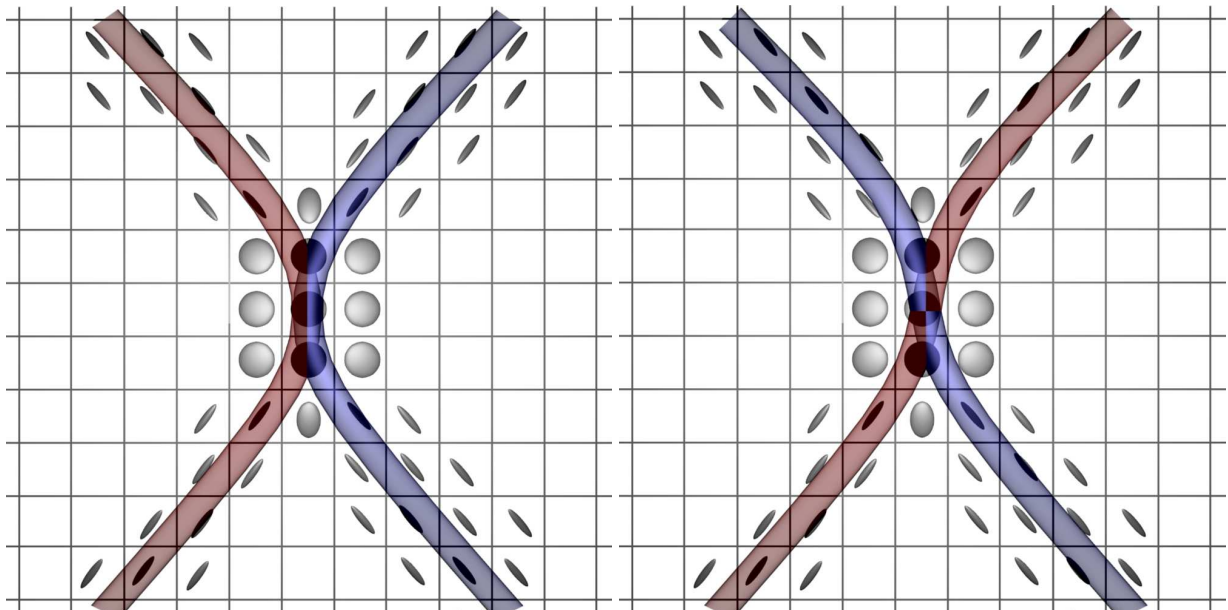


Figure 2.18. Unsolved problems in fiber tracking. Two very different solutions of fiber tracking: fibers kissing (left) and fibers crossing (right) were presented. Both situations provide the same image in diffusion measurements. Therefore, it is impossible to solve this problem basing only on the measurements.

2.7.2 Probabilistic and Stochastic Fiber Tracking

Deterministic approach presents rather straight-forward approach to process diffusion data. However, those methods hardly include noise, uncertainty of direction estimation, probability of other tracts realizations and starting region bias. To incorporate in calculations all those factors, we have to agree that there is only a given probability that voxels at positions X_n and X_{n+1} are connected. This probability can be described by function $P(X_n \rightarrow X_{n+1} | (\theta, \varphi))$. In the case of deterministic fiber tracking this function is a Dirac delta:

$$P(X_n \rightarrow X_{n+1} | (\theta, \varphi)) = \begin{cases} 1 & \text{if the diffusion direction points this direction} \\ 0 & \text{otherwise} \end{cases} \quad (2.56)$$

The function P has to be constructed for each measured voxel. Noise can be estimated from the raw data, uncertainty can be associated with fractional anisotropy [24]. To calculate probability of connection of two distant points in the brain A and B , one would need to integrate probabilities along all possible voxels (paths):

$$P(A \rightarrow B) = \int_0^{2\pi} \int_0^\pi \dots \int_0^{2\pi} \int_0^\pi P(X_1 \rightarrow X_2 | (\theta, \varphi)) \dots P(X_{n-1} \rightarrow X_n | (\theta, \varphi)) d\theta_1 d\varphi_1 \dots d\theta_n d\varphi_n \quad (2.57)$$

Of course, solving this integral in analytical way is very difficult. Therefore, the probability of connection is approximated by Monte-Carlo methods by drawing samples from resulting distribution. Streamline tracking is repeated large number of times always starting for point A . In each step of reconstruction algorithm a random deviation is added to the direction of diffusion. In order to get proper results, one have to make sure that those random deviations have distribution of calculated earlier function P in each voxel. The function $P(A \rightarrow B)$ can be approximated this way with desired accuracy, regulated by number of samples taken.

Chapter 3

Methods

In this part all the steps that have been described in detail in order to obtain the q-ball imaging and the tracking in a clinical conditions. The first part is about the algorithm implementation. This part required a modification to the MR sequence, the data processing framework, new fiber tracking algorithm and a validation of obtained results.

All described step in this part allow to perform a q-ball and the a DTI tracking in clinical conditions using developed copmuter programs and MR sequences.

3.1 Implementation

All code described here was implemented using the MATLAB (Matnick, U.S.A.), unless stated differently. All MR measurements were performed using a 3 T MR Scanner (Trio, Siemens, Germany). However MR sequences were also prepared for 1.5 T Siemens scanners (Avanto and Vision). This section was divided into three parts: data acquisition, data processing and fiber tracking. The first subsection describes how the measurements were performed, what MR sequences were used and how they were modified. This subsection also explains which sampling schemes of q-space were used and how those schemes were calculated. In this part all steps were explained that allow gathering information from real object and transforming it into MR signal (image).

The second subsection explains what happens with the measured data and how to extract diffusion direction as well as other important information. In 'Data processing' all reconstruction algorithms that have been written are presented.

The fiber tracking algorithms were described for both DTI and q-space methods. Deterministic and probabilistic approaches discussed in relation to implementation issues. At the end a unified fiber tracking algorithm is introduced for both DTI (single direction) and q-ball (multiple directions).

3.1.1 Measurement

The measurements were performed using a modification of the Stejskal-Tanner scheme [25]. This is a double re-focusing spin echo sequence with an EPI readout. Two π pulses are used for reduction of eddy-current-induced distortions[26][27]. Data for a whole image slice was acquired after one excitation, resulting in one point in the q-space. Next point in q-space were measured after the repetition time. Each time the diffusion gradients changed, resulting in different position in the q-space. Sequence frames are repeated for

all slices and all q-space points. The standard Siemens MR sequence for DTI was modified for q-ball data acquisition.

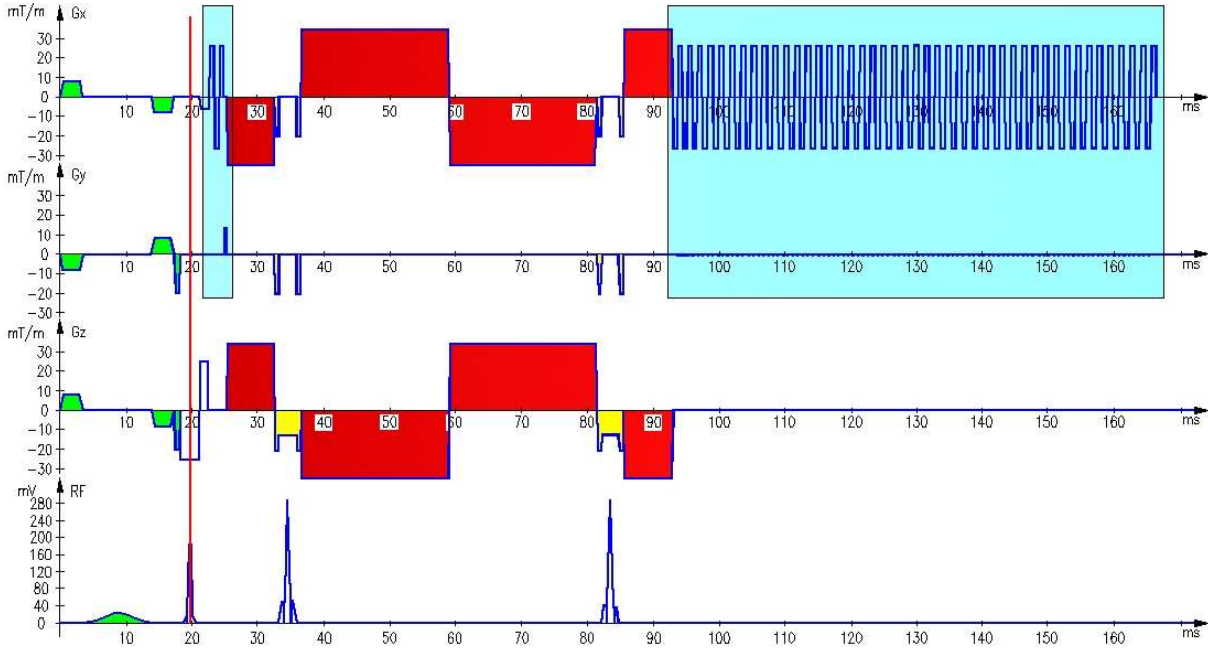


Figure 3.1. Plot of one MR frame from an imaging sequence used during measurements. Gradients and RF are plotted against time. Compartments: green – fat signal suppression, red – diffusion gradients, yellow – crusher gradients for π -pulses, light blue – EPI readout train with navigator echoes.

Each MR sequence can be described by plotting a time dependence of three gradients (in X, Y, Z axis of laboratory reference frame) and of the RF pulse emitter. An example frame from the sequence is shown in fig. 3.1. This plot was created using Siemens’s IDEA software for the MR sequence developing in C++. The frame is constructed with a several blocks. The excitation pulse is marked here with a red vertical line. Before the excitation pulse, a fat suppression block is inserted (green colour). It consists of one wide, non-selective RF pulse with gradient spin rewinders. Along with the RF pulse, one can see a slice selection gradient G_z with re-winder placed immediately after. There are two additional re-focusing π -pulses. In-between them, the diffusion weighting is built by gradients marked in red colour. In this specific frame diffusion gradients are present only in X and Z direction. In general there should be two diffusion gradients positive and negative one. The diffusion gradients are interrupted with re-focusing pulses, which make reverse the phase of spins. To continue de-phasing after the π -pulse the gradient polarity has to be inverted. The same goes for the second refocusing pulse and re-focusing gradient. Just before and right after the re-focusing pulses crusher gradients are performed, in order to eliminate $\frac{\pi}{2}$ -pulse components of re-focusing pulses. When the signal is prepared, an EPI train is performed to form echoes. This part is marked in light blue. There are also three navigator echoes formed after $\frac{\pi}{2}$ -pulse (also marked in light blue). Navigator echoes are needed for proper data positioning in k-space.

The position in the q-space is determined by the direction of diffusion gradient and the b-value as the radius. In the MR sequence the diffusion gradient direction is set by weighting the gradient amplitudes G_x , G_y , G_z with the desired unit vector components. In other words, the integrals over the gradients G_x , G_y and G_z have the same ratios as the components of the vector connecting the origin of the q-space with the measuring point within the q-space. In the example shown in fig. 3.1, the diffusion gradients are located

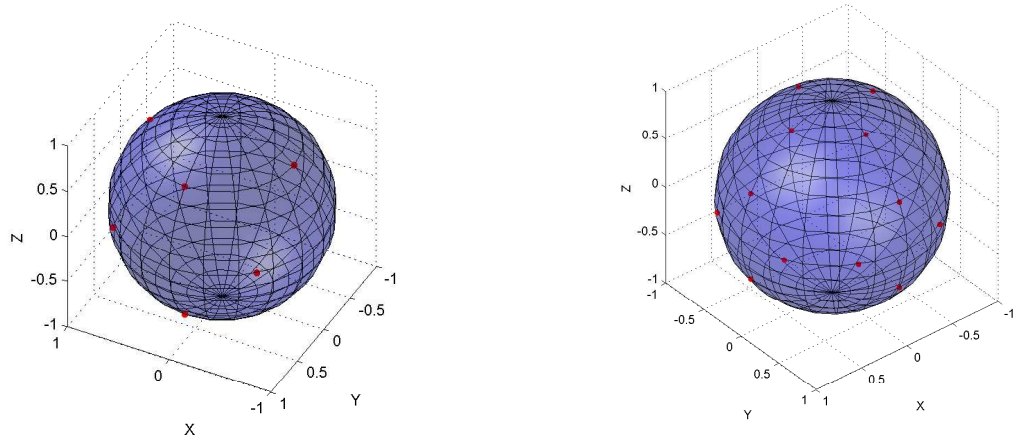


Figure 3.2. Standard Siemens sampling schemes shown in q-space for DTI with 6 (left) and 12 (right) diffusion directions marked as red dots on a unit sphere.

only on G_x and G_z and their amplitudes and duration are the same. This means that the direction of diffusion in this particular case was $[-1 \ 0 \ 1]$, because the polarity of the gradient is inverted.

The b-value in a double re-focusing spin echo scheme can be calculated using the following equation [28]:

$$b = (2\delta\gamma G)^2 \left(\Delta - \frac{a}{2} - \frac{2\delta}{3} \right) \quad (3.1)$$

The parameter δ is the duration of the diffusion gradient \mathbf{G} . The additional parameter a is the duration of the gap for the re-focusing pulses where the diffusion weighting gradients are switched off (yellow colour).

Sampling schemes for the DTI consisting of 6 and 12 diffusion directions of the standard MR sequence are shown in fig. 3.2. New sampling schemes were added for DTI with 12 and 42 diffusion gradient directions, as well as for q-ball with 92, 162 and 252 diffusion gradient directions. The directions were derived from the tessellation of icosahedrons. Non-tessellated icosahedron contains 12 vertices equally distributed on a sphere; however, half of them are co-linear.

Tessellation was implemented by calculating the mid-points of each triangular face of an icosahedrons. Those new vertices created new triangular faces which could be tessellated again. Five-fold tessellation means that procedure was repeated four times resulting with total number of 252 vertices. New sampling schemes were included in standard Siemens sequence, compiled using IDEA software and installed on the scanner.

Figure 3.2 shows both standard Siemens sampling scheme and fig.3.3 the newly implemented scheme. The standard Siemens sampling schemes were created to achieve the shortest possible TE, that why the directions are placed on diagonals in q-space, so the b-value could be build up from three gradients simultaneously. This approach can shorten TE, which result in higher SNR. However, some papers were published showing that rotational invariant schemes are more optimal, because they propagate estimation error in all directions in the same way [12]. Sampling schemes derived from icosahedrons fulfil that condition.

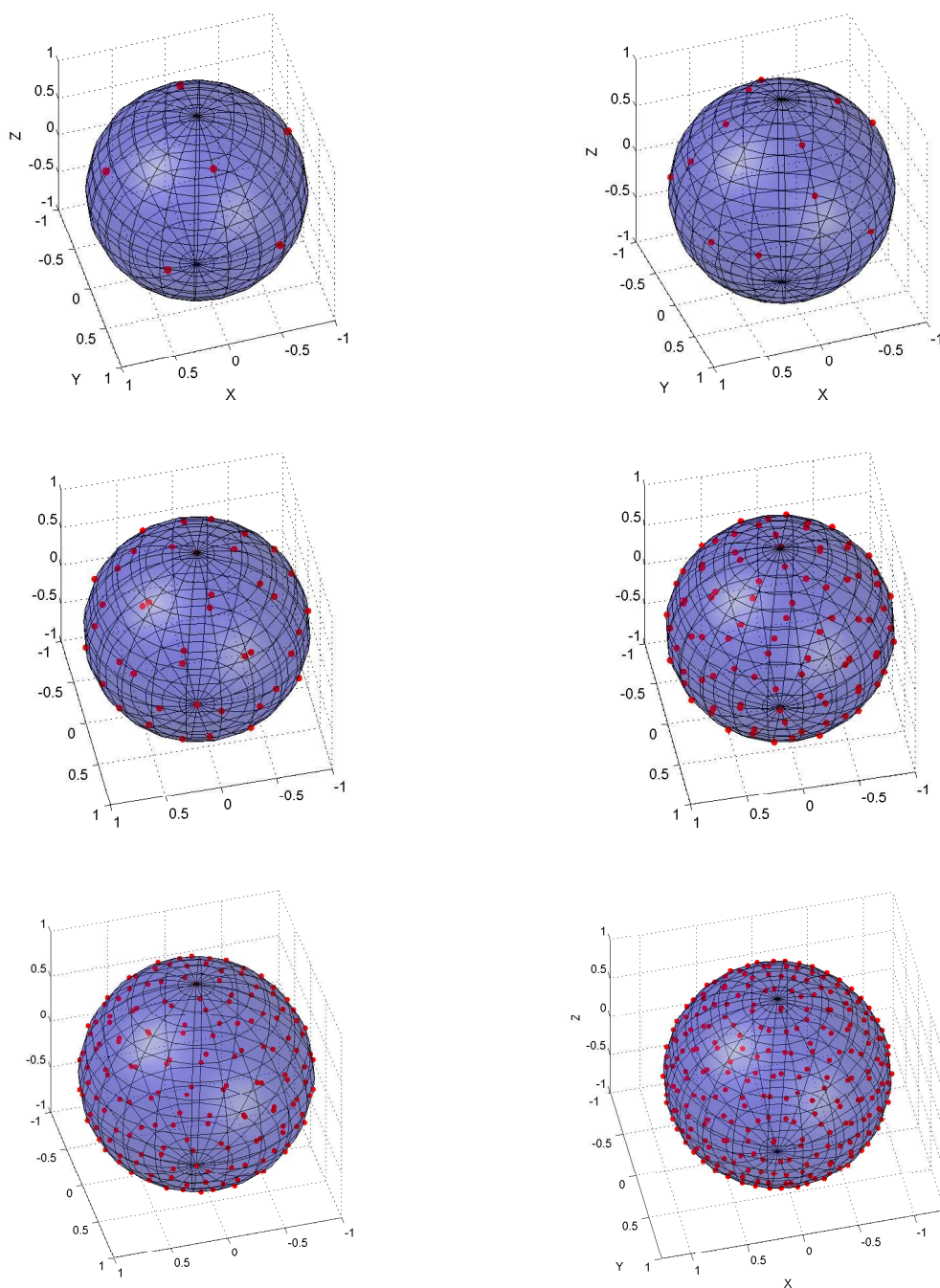


Figure 3.3. Sampling schemes derived from tessellation of icosahedrons and implemented in new MR sequence for q-ball and DTI imaging. Sampling schemes containing (from the top) 6, 12, 42, 92, 162, 252 directions

3.1.2 Data processing

The output of the MR sequence described in the previous section is an image with discrete measurement of signal in space according to eqs. 2.29 and 2.32 described in section 2.5.1. It can be represented as a matrix $S(x,y)$. The MR data are available in a DICOM format. Data are stored as 16-bit unsigned integers, which give 4096 degrees of freedom. MR scanner software scales output of reconstruction of fill the range during inverse Fourier transform over the k-space. A Matlab script was written to import MR data and create proper data structure for further analysis.

DTI implementation

The processing of diffusion data for the DTI processing was prepared as three step procedure. The calculations are performed slice by slice. In the first step input data have to be checked for the consistency. The user has to provide an additional information about the number of directions, the number of slices and which sampling scheme in the q-space was used within the sequence. Next, the cut-off level has to be chosen. A signal histogram from the images without diffusion weighting (B_0) is displayed and a user can enter the threshold value, below which data will not be processed. It makes calculation more efficient, because brain usually occupies only 40 – 60 % of voxels and there is no need to process voxels outside the imaged object.

When all information and data are collected, the main processing program is started. It works in a loop over the number of slices present in the data. Matlab fully supports matrix operations, so eqs. 2.37 – 2.40 can be applied directly. For the calculation of diffusion tensors, apparent diffusion coefficients (ADC) have to be evaluated, as it was described in eq. 2.33, using the measured signals. Matrix $\hat{\mathbf{d}}$, calculated from the normalized diffusion directions of the applied sequence, is calculated with Moore-Penrose pseudo-inversion (eq.2.42).

$$\begin{bmatrix} D_{xx}^{(1)} & D_{xx}^{(2)} & & D_{xx}^{(v)} \\ D_{yy}^{(1)} & D_{yy}^{(2)} & & D_{yy}^{(v)} \\ D_{zz}^{(1)} & D_{zz}^{(2)} & & D_{zz}^{(v)} \\ D_{xy}^{(1)} & D_{xy}^{(2)} & \dots & D_{xy}^{(v)} \\ D_{xz}^{(1)} & D_{xz}^{(2)} & & D_{xz}^{(v)} \\ D_{yz}^{(1)} & D_{yz}^{(2)} & & D_{yz}^{(v)} \end{bmatrix} = \begin{bmatrix} \hat{d}_{(1,1)} & \dots & \hat{d}_{(6,1)} \\ \vdots & \ddots & \vdots \\ \hat{d}_{(1,n)} & \dots & \hat{d}_{(6,n)} \end{bmatrix} \cdot \begin{bmatrix} ADC_{(1,1)} & ADC_{(1,2)} & & ADC_{(1,v)} \\ ADC_{(2,1)} & ADC_{(2,2)} & & ADC_{(2,v)} \\ ADC_{(3,1)} & ADC_{(3,2)} & & ADC_{(3,v)} \\ ADC_{(4,1)} & ADC_{(4,2)} & \dots & ADC_{(4,v)} \\ ADC_{(5,1)} & ADC_{(5,2)} & & ADC_{(5,v)} \\ ADC_{(6,1)} & ADC_{(6,2)} & & ADC_{(6,v)} \end{bmatrix} \quad (3.2)$$

To simplify matrix calculations, all voxels of the image were enumerated with an index v . n is the number of diffusion direction used during the acquisition. For each voxel, there is a vector of n ADC values, which multiplied by $\hat{\mathbf{d}}$, result in tensor components.

Figure 3.4 shows measured data from an example slice as well as calculated ADC values. In the lower row in that figure estimated tensors of diffusion are shown. Each image shows one of the tensor components.

Next important step is the diagonalization of diffusion tensors in order to obtain eigenvalues and eigenvectors. Since tensors are calculated only for pixels above the noise threshold, diagonalization is calculated for each voxel separately. This significantly speeds up the calculations. The example result of diagonalization was shown in fig. 3.4.

When looking on fig. 3.4b,c, the tensors components, eigenvalues or eigenvectors make it hard to read underlying directional information. Therefore, the last step of DTI processing is to make obtained data *human-readable*. Fractional Anisotropy can be

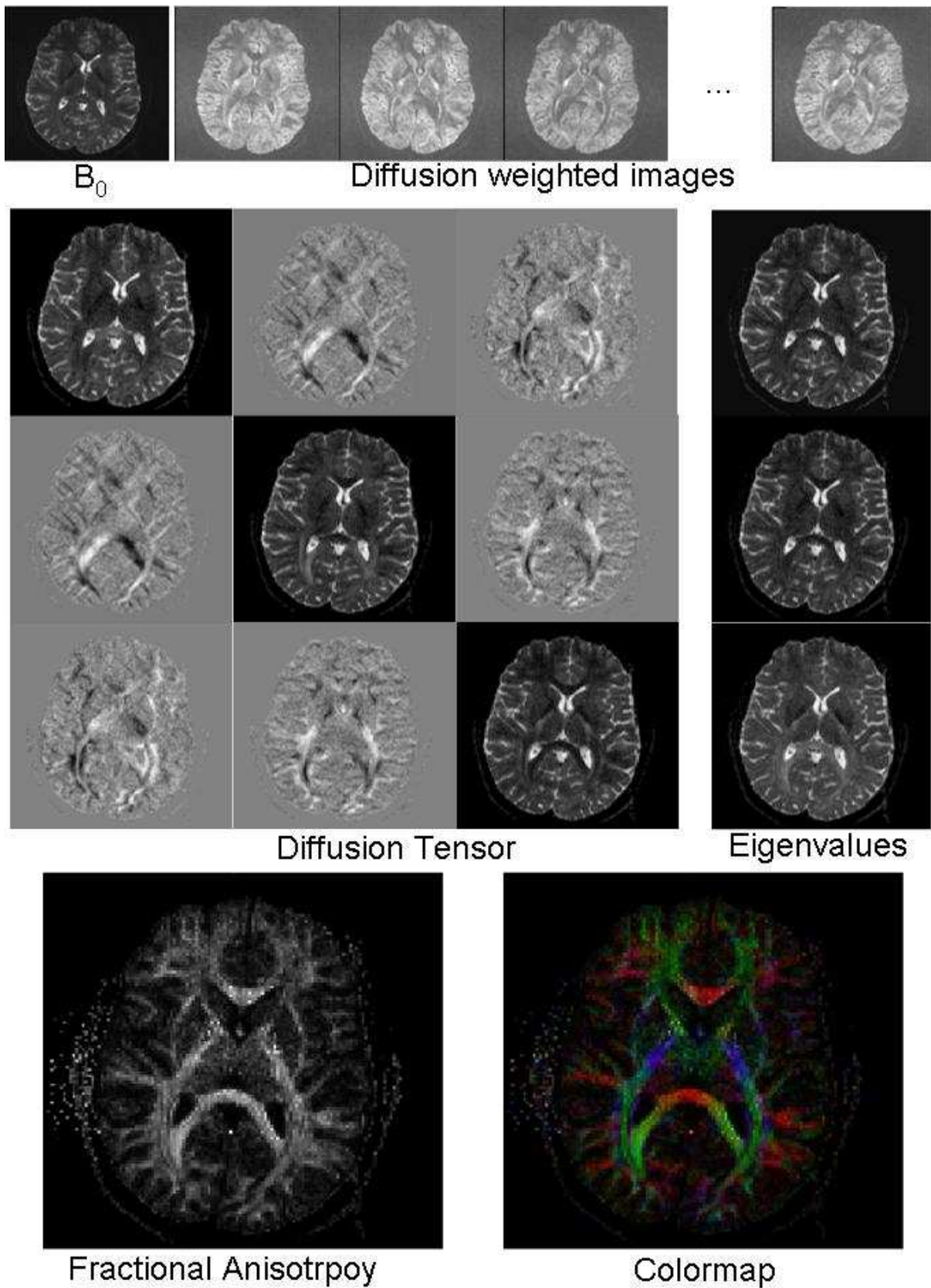


Figure 3.4. MR images of DTI measurements and data processing steps. A) Raw data as measured in the scanner. Each image represents one point in q-space (diffusion direction), B) The components of a diffusion tensor, C) Components of the eigenvalues, D) the Fractional Anisotropy map, E) Colour-map.

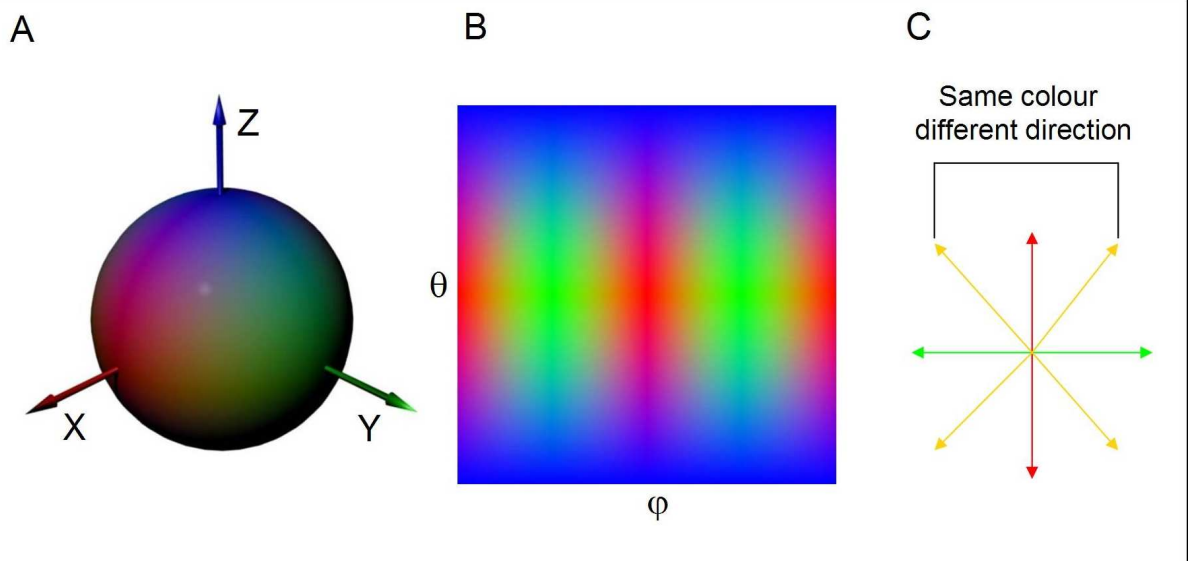


Figure 3.5. Colour encoding of direction in diffusion measurements. A) X direction is red, Y is green and Z is blue, all other directions are a mixtures of colours. B) Colour-map representation in spherical coordinates, C) Equivocal direction encoding may result in assigning one colour to more than one unique direction, as shown by the yellow arrows.

directly calculated using eq.2.45. Note, that we have assumed that diffusion tensor was positive. In some cases, where noise addition is significant, it may happen that eigenvalues are going to be negative. In consequence, the FA value may exceed limit of 1. Those points have to be located and replaced with value of 1. Same slice example of FA is shown in fig. 3.4d.

Up to now, the directional information was not expressed. The diffusion direction has three degrees of freedom, an image only one. To encode the direction the colour is used. The degrees of freedom are red (R), green (G) and blue (B) components. The last part of fig. 3.4e shows an example colormap. Axis of the laboratory reference frame are mapped respectively to colours (i.e. $X \rightarrow R$, $Y \rightarrow G$, $Z \rightarrow B$). In other words, red voxels show fibers that go in anterior-posterior direction, green go left to right subject side and blue go from top to bottom. Colour coding loses directional information and it can be used only for reference and visual inspection. Colour diffusion information is weighted with FA to remove unnecessary colours from regions with colormap in given voxel is calculated as:

$$CM(R, G, B) = (|\varepsilon_x^{(max)} \cdot FA|, |\varepsilon_y^{(max)} \cdot FA|, |\varepsilon_z^{(max)} \cdot FA|) \quad (3.3)$$

where $\varepsilon^{(max)}$ is the eigenvector associated with the largest eigenvalue and FA is the fractional anisotropy value in that voxel. Isotropic voxels, with FA value close to 0 will be greyed out regardless of the direction encoded there. Only anisotropic ones remain.

Taking the absolute value of the vector components makes the process of colormap calculation irreversible, what is shown in fig. 3.5. This representation works well in basis directions. However, in all the other cases, different directions are represented by the same colour. As in example (fig. 3.5c), the yellow colour represents two different directions with 90° in-between them.

A raw data smoothing can be used when signal-to-noise ration is low. It usually happens when data was acquired with high resolution (voxel size < 2.0 mm in 3 T scanner). Smoothing was performed by convoluting the images a Gaussian kernel with width equal to $0.51 \times$ the voxel size.

Q-ball implementation

Q-ball reconstruction was implemented according to [6]. Both DTI and q-ball reconstruction can use the same data-reading script. In general, the reconstruction implementations are similar. In first step, a reconstruction matrix have to be calculated (like $\hat{\mathbf{d}}$ for DTI). This matrix transforms measurement data directly into radial projection of PDF (i.e. ODF). Next, ODFs for all voxels that contain brain have to be calculated. In last step, again *human-readable* images and visualizations have to be produced.

The reconstruction process is more memory demanding than in the case of DTI, since each voxel have now 252 measured values. The coordinates of points on this equator have to be calculated. Let us start in XZ-plane and use the spherical coordinates (θ, R) . The number of steps (k) is set by default to 42. To make a equally divided circle, the radius (R) was set to 1 and the angle θ was calculated as $\frac{k \times 2\pi}{no.ofsteps}$. Now, the spherical coordinates of reconstruction circle were converted to Cartesian coordinates. The points had to be rotated, in the way that the circumference surface is perpendicular to direction of reconstruction \mathbf{u}_i . It can be achieved by applying following transformation over 42 points on the circle that were calculated in the previous step:

$$\mathbf{R}(\mathbf{z} \rightarrow \mathbf{u}_i) = \frac{(\mathbf{z} + \mathbf{u}_i) \cdot (\mathbf{z} + \mathbf{u}_i)^T}{(\mathbf{z}^T \mathbf{u}_i) + 1} - \begin{bmatrix} 1 & 0 & 0 \\ 0 & 1 & 0 \\ 0 & 0 & 1 \end{bmatrix} \quad (3.4)$$

This is a general expression for rotation matrix $\mathbf{R}(\mathbf{z} \rightarrow \mathbf{u}_i)$ that rotates vector \mathbf{z} into vector \mathbf{u}_i . The circle points were generated on XY-plane, so the normal (reconstruction) vector was pointing Z-axis ($\mathbf{z} = [0 \ 0 \ 1]$). Vectors \mathbf{u}_i are the directions in which we want to calculate ODF function value. In all calculations included in this thesis the ODF values were reconstructed in same directions as the directions of sampling scheme. Therefore, 252 rotation matrices were calculated. Previously calculated points on the reconstruction circle in XY-plane were multiplied with each of rotation matrices resulting in a collection of 10584 points located on 252 reconstruction circles (42 x 252).

To calculate ODF, it is required to know the ADC value in each of 10584 points. The measurement was performed only on 252 points, so it is necessary to interpolate. The angular distances between all reconstruction points (**OUT**) and all points of sampling scheme (**IN**) have to be calculated. This operation result in matrix **DIST** containing [252 x 10584] points.

$$\mathbf{DIST} = \arccos(|\mathbf{OUT}^T \cdot \mathbf{IN}|) \quad (3.5)$$

A Gaussian function was calculated for all components of **IN**. The amount of interpolation and smoothing can be controlled by parameter δ :

$$\mathbf{W}^{(Gauss.)} = \exp\left(-\frac{\mathbf{DIST}^2}{\delta^2}\right) \quad (3.6)$$

In this case \mathbf{DIST}^2 means taking power of 2 of each element of matrix **DIST**.

Final form of reconstruction matrix can be obtained by normalizing matrix $\mathbf{W}^{(Gauss.)}$, so the sum in each of 10584 row is equal to one. The reconstruction matrix interpolates 252 measured ADCs into set of 252 circles of reconstruction by dot product. The last step of reconstruction was to add interpolated values on each reconstruction circle. The final result is a collection of scalar values, one for each reconstruction direction. Those values are according to eq. 2.50, a radial projection of PDF convoluted with a zeroth-order Bessel function.

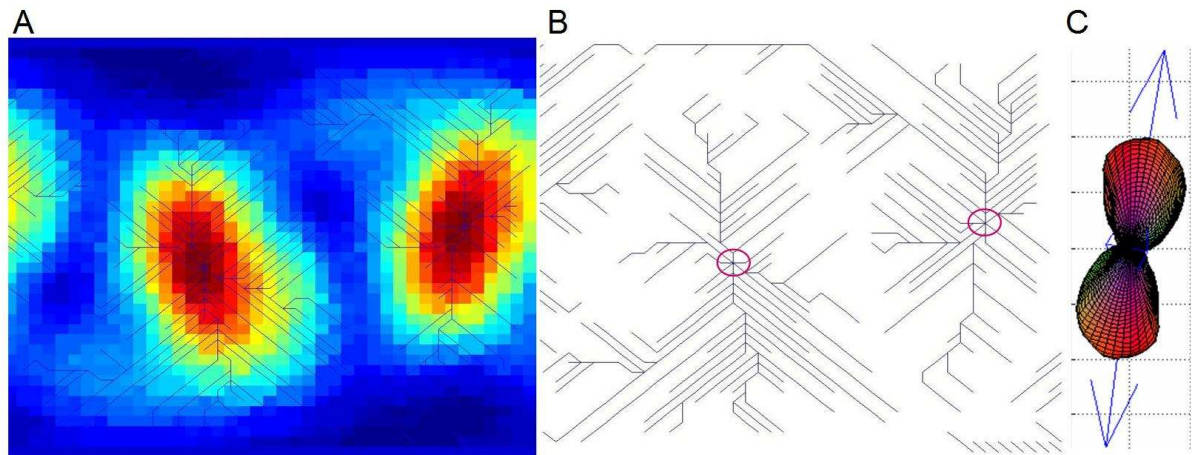


Figure 3.6. Q-ball direction discovery algorithm. A) Q-ball reconstructed values presented in spherical coordinates, B) Result of 100 repetitions for maximum finding algorithm with random starting points. two global attractors are found (red circles). Those points in spherical coordinates represent direction of diffusion, as shown with arrows in C.

When ODF is known in each voxel, like in the case of DTI, diffusion directions have to be extracted and FA and colormaps have to be calculated. Expression 2.51 for general fractional anisotropy allows to calculate it directly from the ODF functions. In DTI there are only three eigenvalues, but in ODF the number of reconstructed points is not limited by any constrain. If there was only one direction of diffusion, it would be enough to find maximal projection value. More directions have to be identified. Therefore, the algorithm has to recognize all local maxima and decide which form diffusion direction in ODF shape.

In this thesis the diffusion direction extraction was implemented as an iterative algorithm that starts at random location on the ODF function and in each step advances in the direction of maximal gradient until a local extremum is reached. It is required to remove starting point bias. This procedure is repeated 100 times starting from different position in each case. Figure 3.6 shows an example of ODF presented as a map in $\theta\varphi$ -coordinates with the trajectories of algorithm 3.6b that was identifying the local maxima. In figure 3.6c a 3D q-ball shape is shown with arrows that point directions of diffusion found in that shape.

3.1.3 Fiber Tracking

Reconstruction of nerve bundles follows directly the estimation of diffusion direction in the white matter. The procedure consists of starting points selection and an iterative algorithm that follows the diffusion directions. In each step termination conditions have to be checked to avoid fiber over estimation and tracking outside the white matter. As mentioned before a starting region is mandatory, unless tracking is performed from all points in the white matter.

Streamline tracking

Implemented algorithm was performed in a continuous space using directly eq.2.55. This means the fibertracking is not binded with discrete nature of MR measurement. The step size (Δx) was constant and set to a half of the voxel size. In the case of non-uniformed data sampling, the ratios between step size components was the same as the voxel sizes in basis directions. No smoothing or averaging was performed. The algorithm was implemented

as infinite loop with break conditions. There were five stop conditions. Three of them were checking if algorithm reached the data volume boundaries (in X, Y or Z direction). Remaining two were checking if FA in current position is higher than assumed limit and if angle $\alpha = \arccos(|\varepsilon_{prev} \cdot \varepsilon_{curr}|)$ is smaller than requested threshold. When one of the conditions was fulfilled, the tracking was interrupted and the trajectory was saved.

Due to diffusion symmetry, tracking have to be repeated from each starting point twice, since the estimated eigenvector and an opposite one are valid diffusion directions. Since each of created fibers may have different length, it is required to store the trajectory positions as a cell array.

An extension for data containing more than one direction of diffusion per voxel (i.e. q-ball) was added. In this scenario, the algorithm has to choose in which diffusion direction the fiber should be extended. The direction chosen in previous step is compared with all diffusion directions present in the current position. The one with the smallest angular difference is chosen to be the one to follow. During q-ball reconstruction, noise in the measured data can result in additional local maxima in the ODF. This may provide some fake directions of diffusion. They are easy to identify, because they have very low ODF values. The algorithm rejects the diffusion directions with ODF values lower than 30% of the ODF value for the main diffusion peak found in given voxel.

Multiple tracks per voxel and other extensions

Voxels have finite dimensions which are couple orders higher than the dimensions of axons. It often happens that the volume of the voxel contains multiple fiber bundles. When the tracking start from a given voxel only one trajectory is realized. Due to the discrete nature of the measurement, starting points have to be set somewhere inside the selected voxel. Usually the voxel centre is chosen. However, if one start tracking from another position inside the voxel, the trajectory can be reconstructed differently. An example of such a realization is shown in fig.3.7. For sake of simplicity the example was shown in 2D. Three fibers were reconstructed from a voxel placed in lower-right corner. The ellipsoids represent the diffusion measurement result. The situation presented here shows two fibers populations joined at the beginning into one bigger bundle and then splitting into two directions. The isotropic diffusion in the middle of the figure represents a region of grey matter of fluid which those two fibers are by-passing. Let us consider three cases, standard approach, starting tracking from the centre and two boundary conditions: starting from the opposite corners of the starting voxel. As shown in fig. 3.7, each reconstruction show different path. Red and blue fibers are bent into separate directions. The green trajectory ends, because the FA value in last step was lower than the threshold.

In order to consider multiple starting points within one voxel, a division factor was implemented in the tracking algorithm to set a division factor. This way the fiber tracking procedure will be repeated n_{dir} times (number of directions) from different positions within starting voxels. Each voxel was uniformly subdivided on basis of Cartesian grid. This approach removes the bias created by discrete measurement and poor resolution compared with size of the imaged structures. In the case of voxels with multiple diffusion directions algorithm have to be started both ways for each of direction found.

Additional extension is available for DTI with poor SNR. In this approach, algorithm tries to maintain the previous direction of diffusion. The direction in which the tracking algorithm moves is a combination of diffusion found in current position and up to 50% of the previous diffusion direction. The amount of previous direction addition was in a linear relation to FA found in previous voxel. Additional weighting parameter is used in tracking. This is scalar factor that is multiplied with the diffusion direction from the

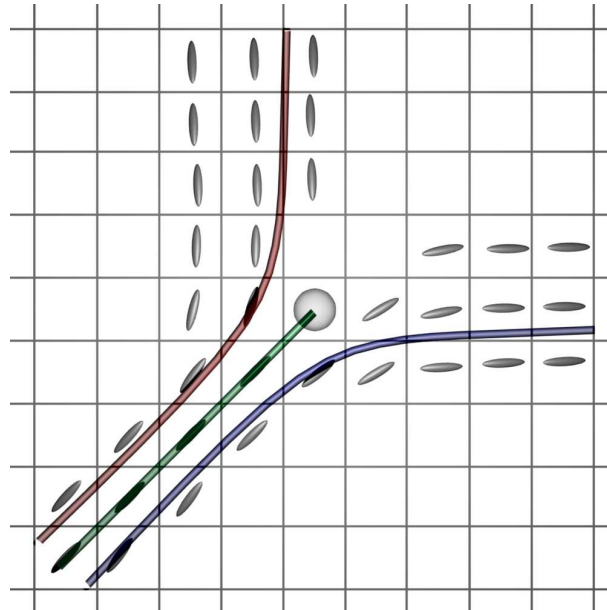


Figure 3.7. Effect of starting point bias. Three fibers trajectories originating from the same voxel are shown. Due to coarse resolution, the reconstructed fiber can have different end-point depending on starting position within the voxel.

previous voxel.

Probabilistic Fiber Tracking (PFTR)

For generation of a random direction of diffusion, two control functions have to be estimated. First, is the function that controls the shape of the distribution of random angles around the main diffusion direction from the measurements, here denoted as $H(\theta)$. Second, a function, that controls the parameters of function $H(\theta)$ is required. This function translates the fractional anisotropy from the measurements into parameters of $H(\theta)$. Here denoted as $\Sigma(FA)$

Probabilistic approach was implemented using previously described deterministic tracking program with one change. When the algorithm made a step, there was a part of code that returned local direction of diffusion and FA. This part was replaced by a routine that was generating a random distribution of directions about the direction of diffusion found in a given voxel. The width of distribution was related to FA value. For FA values close to 1, random direction generator should return only measured directions of diffusion and in the case of FA close to 0, it should return uniform distribution over the sphere, regardless of diffusion direction. The implementation of random direction generator is described in following subsection.

Generation of random directions for PFTR algorithm

To simplify the calculations, the Z axis of the Cartesian coordinate system was assumed to be the main direction of diffusion. The problem of generating random directions is equal to generating the points on the unity sphere. It is easier to solve it in the spherical coordinate system; therefore, the radius (R coordinate) is always equal to unity. If the Z axis points the main diffusion direction, the ϕ -coordinate is responsible for the shape of distribution around the direction of main diffusion and the θ -coordinate responsible for the distribution of the angles between the main direction of diffusion and the generated ones.

The standard random number generators produce random numbers in the range $< 0, 1 >$. The ϕ -coordinate was assumed to be equally distributed in this calculations; therefore, it can be written as:

$$\phi = d * 2\pi \quad (3.7)$$

where d is randomly generated number from $< 0, 1 >$ range. In this way, the random direction will equally distribute around the direction of main diffusion at given angle θ .

For the angle θ , a Gaussian distribution was assumed; however, in spherical coordinates, one has to take into account that density of points in spherical coordinates varies for different θ . To illustrate the problem, let us take the sphere homogeneously covered with random points. This means that the number of points found in some region is proportional to the area of that region and the number of points found on any circle on the sphere is proportional to its length. In the sphere with radius $R = 1$, the length (l) of the circumference found at given angle θ can be written as:

$$l(\theta) = 2\pi \sin(\theta) \quad (3.8)$$

The desired distribution H of θ -coordinate must contain the Gaussian function (G) multiplied by the density function (DF) equal to $l(\theta)$, the length of the circumference:

$$H(\theta, \sigma) = G(\theta, \sigma)DF(\theta) \quad (3.9)$$

which yields:

$$H(\theta, \sigma) = C \exp\left(-\left(\frac{\theta}{\sigma}\right)^2\right) \sin(\theta) \quad (3.10)$$

where C stands for all constants and expressions which do not depend on θ . Since $H(\theta, \sigma)$ is a probability distribution, it has to fulfil the condition:

$$\int_0^{\pi/2} H(\theta, \sigma) d\theta = 1 \quad (3.11)$$

Any constants and expressions that do not depend on θ are irrelevant. Final form of desired θ distribution is written as:

$$H(\theta, \sigma) = \frac{C e^{-\left(\frac{\theta}{\sigma}\right)^2} \sin(\theta)}{C \int_0^{\pi/2} e^{-\left(\frac{\theta}{\sigma}\right)^2} \sin(\theta) d\theta} = \frac{e^{-\left(\frac{\theta}{\sigma}\right)^2} \sin(\theta)}{\int_0^{\pi/2} e^{-\left(\frac{\theta}{\sigma}\right)^2} \sin(\theta) d\theta} \quad (3.12)$$

The random number generators implemented in PCs can return random numbers from the $< 0, 1 >$ range, resulting flat distribution, which is a constant function. It can be transformed into $H(\theta, \sigma)$ using cumulant transformation [29]. This routine requires three steps: First, a cumulant ($F(\theta)$) of desired distribution for a given σ value, has to be calculated as:

$$F(\theta) = \int H(\theta) d\theta \quad (3.13)$$

because the $H(\theta)$ in the range $(0, \pi/2)$ is a positive and normalized (eq.3.12) function; therefore, the $F(\theta)$ is monotonic and has values from the range $< 0, 1 >$. The second step is to find the inverse function of cumulant $F^{-1}(d)$. Both steps can be done efficiently using numerical methods. In the last step, the directions are randomly generated around the Z direction with the assumed distribution, when:

$$\theta = F^{-1}(d) \quad (3.14)$$

The randomly generated point $P_{\phi\theta R}$ has to be transformed to Cartesian coordinates P_{xyz} for compatibility with the tracking algorithm. All calculations above are done with constant, given σ value, because for a single voxel it is constant. Relation between σ and diffusion in the voxel is explained in one of the following subsections.

Control over the random direction generator

The fractional anisotropy (FA) describes the order in the fiber organization inside the voxel and it is calculated from the tensor eigenvalues, providing an experimental measure of anisotropy. To obtain that one must assume some relation between the scatter of random directions and the FA. For the high values of FA (> 0.5), the scatter should be minimal. High anisotropy level denotes that inside the voxel, fibers are aligned and one direction of diffusion dominates; therefore, low scatter is required, in order of degrees. For low FA values (< 0.1), homogenous distribution should be used, because the diffusion in such voxels is close to isotropic. The distribution can be controlled by introducing a functional W :

$$BA(\sigma) = W(H(\theta, \sigma)) \quad (3.15)$$

The border angle (BA) for given σ is calculated as an angle of a cone around the direction of diffusion which covers 95 % of all generated directions:

$$0.95 = \int_0^{BA(\sigma)} H(\theta, \sigma) d\theta \quad (3.16)$$

For each σ value the corresponding border angle can be calculated by numerical solving. Knowing the functional $BA(\sigma)$, one can easily control the extent of random direction generation, just by proposing a relation between FA values and desired radius of random directions scattering.

Referring to the conditions mentioned above, a sigmoid function $S(FA)$ was proposed for modelling the relation between the FA index and the border angle. Almost flat tails of the sigmoid function can model low and high FA regions where one expects high focus of directions for high FA and isotropic distribution of low FA. The middle range of sigmoid is almost linear, which can cover the range of uncertainty of main diffusion direction due to noise, fiber crossing and partial volume artefacts.

$$BA(\sigma) = S(FA) = sgm(FA) \quad (3.17)$$

Having both relations $S(FA)$ and $BA(\sigma)$, it is possible to reconstruct function $\sigma(FA)$:

$$\sigma(FA) = BA^{-1}(S(FA)) \quad (3.18)$$

The DTI provides anisotropy information as FA values; therefore, this relation is required, so the FTR algorithm can use a specific distribution for a given voxel with a specific FA value.

At the beginning of the calculations, the Z axis was assumed to be the main diffusion direction; therefore the resulted random distribution of points generated using eq.3.14 and relation from eq.3.18, has to be rotated to the coordinate system of the reconstructed tensor. The rotation matrix that transforms Cartesian coordinates into coordinates of the tensor is the eigenvector matrix.

After the reconstruction of the DTI measurement, the FA index is taken to calculate the σ parameter. For this specific σ , all calculations in eqs.3.7 – 3.18 will result a random direction distribution. The described algorithm was producing random directions around the Z-axis. The last step was to rotate the obtained random direction to the coordinates of diffusion tensor found in the voxel. The rotation could be achieved by using eigenvectors. Since the eigenvectors are orthogonal, they form a rotation matrix. Therefore, it is enough to multiply randomly generated direction by matrix of eigenvectors. It is important that the eigenvector ε corresponding to the maximal eigenvalue was the last one, since we want to rotate Z-axis into the direction of diffusion.

$$\mathbf{D}^{rand.} = \mathbf{D}^{gen.} \cdot \varepsilon \quad (3.19)$$

This direction of diffusion replaces in the measured direction of diffusion in tracking algorithm. Eq.3.7 does not take second and third eigenvalues into account. In the case of disc-shaped tensor ellipsoids the second eigenvalue can have very close value to the main eigenvalue, showing restricted water motion only in direction of the smallest eigenvector. The distribution should also follow that changes.

Second and third eigenvalues

FA controls the width of the distribution. To quantify the relation between second and third eigenvalue a ratio was calculated: $R = \frac{\varepsilon_{II}}{\varepsilon_{III}}$. This ratio was used to deform ϕ distribution by generating points on a circle and scaling the X or Y component according to:

$$S_f = \frac{1}{R^6} \quad (3.20)$$

Scaling was performed on X or Y axis if eigenvalue in X or Y accordingly was the smallest one. Factor R^6 was empirically tested in phantoms.

Each fiber tracking performed with this approach resulted in one sample of integral defined by eq. 2.57. Repeating this procedure allows estimation of connection probability between the starting region and any other region in the brain. As the number of iteration rises, the convergence of result is reached.

Probabilistic tracking is creating large number of trajectories, much more than in deterministic approach. Keeping them in computer raises a memory issue. Two approaches were implemented to handle the *out-of-memory* problem. The trajectories can be either stored on hard drive for further analysis so only the current one is kept in memory, either each trajectory can be processed on-the-fly. In the second approach, an empty (containing zeros) matrix with size of the analyzed dataset is created. Each time, a trajectory is calculated, voxels in the empty matrix that contain the fiber are set to 1. All trajectories are added up. Final connectivity matrix contain in each element number of trajectories that went through. The matrix was the same size as the dataset, so the elements of the connectivity matrix corresponds positions in the brain.

3.1.4 Fiber Tracts Analysis

Visual Inspection

The most common method for fiber tract analysis is visual inspection, where user can interactively choose a starting region of interest and examine calculated trajectories. The same can be achieved for probabilistic fiber tracking. The connectivity matrix can be visualized by overlaying colour-scaled values over a brain image in grey-scale. Second option is to evaluate iso-probability surfaces and render them above reference image. First option allows for detailed qualitative analysis. Second one allows seeing whole 3D probability shape and examining fiber bundles splitting.

Mask Method

When exact fibers trajectories are available either on hard drive or in memory, the mask method can be used. This methods is most efficient when *brute force* (see 2.7.1 on p.27)

method of deterministic fiber tracking was applied. It allows extracting pathways between multiple regions of interest.

A mask vector with length equal to number of stored trajectories has to be created for each region of interest. A distance between all points of the ROI and each point in each trajectory was calculated and minimal distance was found for each tract. A special threshold distance has to be chosen for each region of interest. If the calculated minimal distance is smaller than the threshold, then the mask element was turned to 1 for respective fiber number. The mask vector contains value 1 for those fibers that cross or pass near by the region of interest. Due to several memory and performance issues, this part was implemented as Dynamic Linked Library (.dll) in C++ and attached to MATLAB code through a 'dll' interface.

The mask of each region of interest is a Boolean variable. To plot fibers that cross only regions of interest it is enough to make a logical sum out of corresponding masks. Logical OR operation answers to question, which fibers directly connect selected regions of interest. When more than two regions of interest are available, then more complex logical operations are possible to narrow fibers selection to a specific connectivity reconstruction.

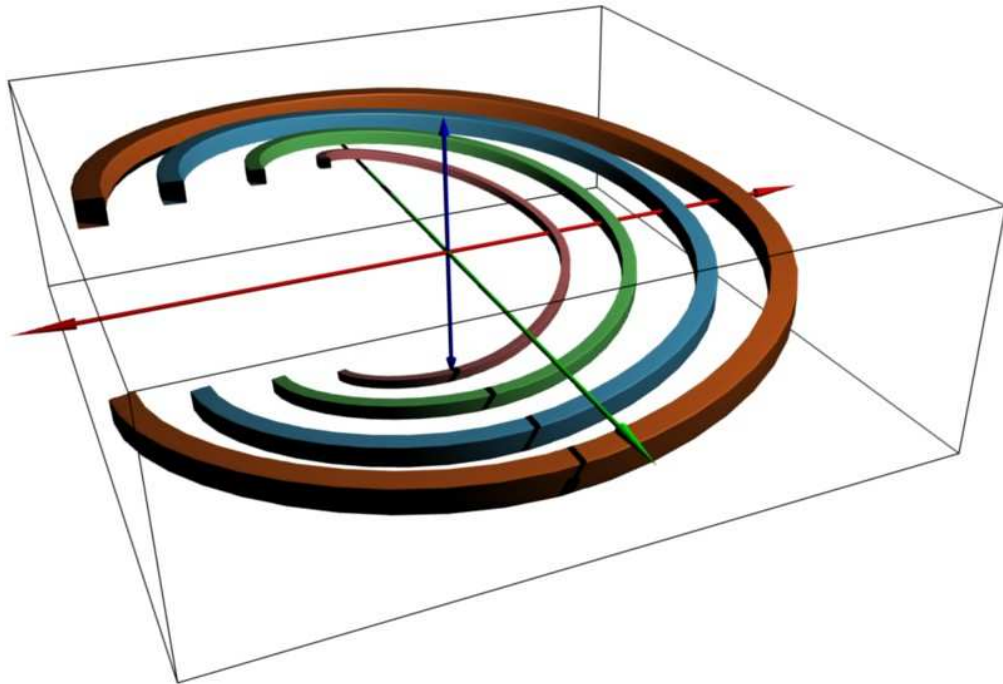


Figure 3.8. Example of an digital phantom for tracking algorithm testing. 3D visualization of simulated fiber.

Probability matrices

The connectivity matrix have to be normalized by dividing all values by the number of repetitions taken times number of voxel subdivisions if the 'multiple tracks per voxel' option was used (see 3.1.3 on p.40). This way the index for the starting point is equal to one and decreasing as the fiber tract propagates and spreads through different branches of white matter. Regions of interest that contain more than one point should be processed voxel by voxel, generating a connectivity matrix for each one. Total connectivity matrix whole region of interest can be calculated by multiplication of all normalized connectivity matrices.

Several destination regions of interest can be chosen in second step. An integral of connectivity matrix values over the area of destination region of interest provide measure of probability of connection between starting voxel and given destination region of interest. It is possible to estimate which connection is more probable by comparing the integrals and choosing the maximal.

3.2 Validation

The prepared MR sequences, implemented algorithms and written programs had to be tested with in well defined laboratory conditions, before they could be used in applications. This section describes all steps that have been taken in order to check propriety of used tools. The section was divided into three parts. First one describes the digital phantoms that test tracking engines. Second part describes an attempt to prepare an artificial phantom, which could be measured in a MR system for testing prepared MR sequence and reconstruction algorithms. The last part describes an *in-vivo* measurement with a healthy volunteer, where all parts were tested and referred to data found in the literature.

3.2.1 Digital phantoms

Digital phantoms are synthetic data imitating the measurement. The purpose of digital phantom creation was to test fiber tracking algorithms. Therefore, only the cell array containing the diffusion directions and FA maps were simulated not the whole diffusion experiment. The first phantom (DP1) was designed for testing if algorithm properly recognizes directions of diffusion. Three synthetic arrays (64x64x64) were created with a one fiber of size of 8x8 voxels going in X,Y,Z in each of the phantoms. Fractional anisotropy in voxels containing the fiber was set to 0.8. No noise was added. Stability of reconstruction was examined by checking the number of fibers reaching the opposite side of volume. In each phantom centre voxels were replaced by FA of 0.1 to check stop conditions handling. In the next step centre voxels were replaced with voxels containing diffusion direction perpendicular to the rest of the voxel.

Next two phantoms (DP2, DP3) had fibers on diagonals of the cube volume defined by phantom cell array. The phantoms simulated to examine, if algorithm handles non-orthogonal diffusion direction the same way as orthogonal. As it was tested for orthogonal directions, gaps of low FA and different diffusion directions were inserted to check stop conditions.

A phantom (DP4) containing four fiber-spirals making 2π turn was used to test how the implemented algorithm handles the curvature of the fiber tracts. Spirals have different radiuses.

The implemented algorithm can handle q-space data with multiple diffusion directions. It was necessary to check crossing regions handling. Two additional phantoms (DP5, DP6) were created with simulated fiber crossing in the middle of the volume. In the first one fibers were located along the basis directions (X,Y). In the second one, two diagonal fibers were crossing.

In all cases, the starting points were placed on one of the volume boundary. The number of fibers reaching the other boundary was check.

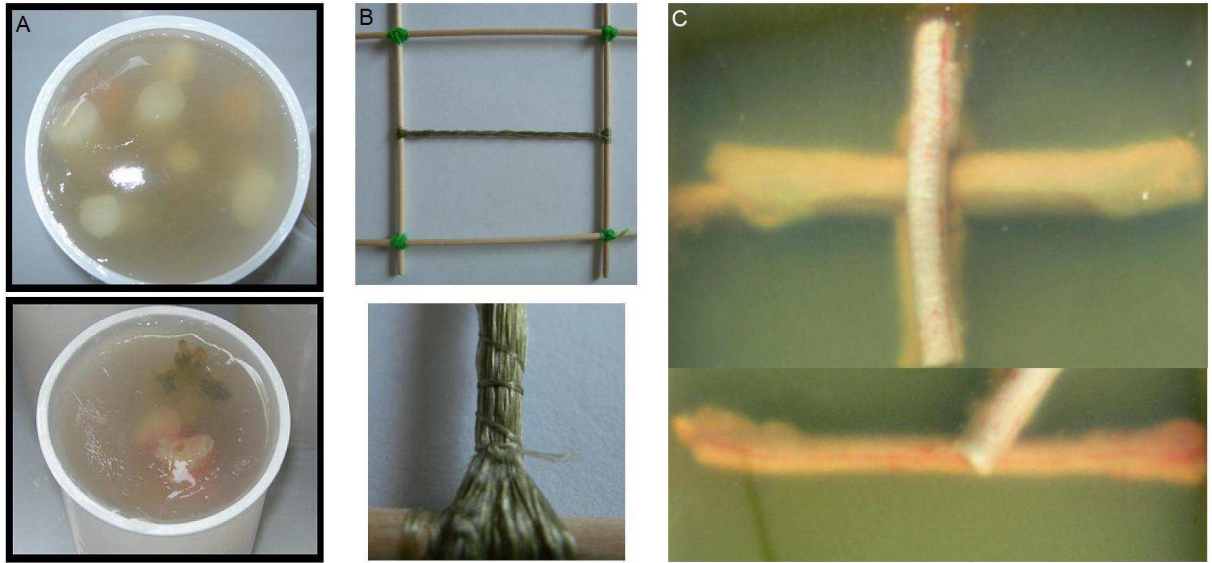


Figure 3.9. Artificial phantom for diffusion measurement. A) Rhubarb submerged in agar gel, B) Dyneema fibers, C) pig's spine cords in agar gel.

3.2.2 Artificial phantoms

The MR sequence and data reconstruction algorithms could be tested in a phantom study. Anisotropy found in the brain is difficult to simulate and there is no ready-to-use phantom for diffusion measurement. Several materials were tested for their anisotropic properties. Organic material from rhubarb and asparagus were tested. Second group were synthetic, non-organic materials as capillaries and Dyneema fibers. Last material for a phantom was pig's spinal cord.

A phantom simulating fiber crossing was made. The pig spinal cords were fixed in 2% agar-agar solution in a rectangular container suitable to insert into the head coil of the MR scanner. Spinal cords were inserted into the container in order to create a cross. The spinal cords were put in two layers - one above the other. Only one spinal cord went through the crossing area on each layer, spinal cords in second direction were just approaching crossing region. This way of construction was minimizing the partial volume effects and it was assuring no fibers had to be bent during preparation.

One unweighted image and 252 diffusion weighted images were acquired with following parameters: $TE = 126$ ms, $TR = 2000$ ms, b-values: 1000 and $2000 \frac{s^2}{mm}$. The slice thickness was set to 10 mm in order to cover fibers from both layers of phantom. The diffusion measurement returns an average signal over all volume of voxel, in this way crossing area contained two populations of parallel going fibers. Phase-read plane was aligned to XZ plane of the MR system.

The directions of diffusion were obtained from the orientation distribution function (ODF). Voxels from the crossing area for each direction and from the arms were analyzed separately. Therefore, directions of diffusion were divided into four groups:

1. Voxels with single fiber population pointing X direction, voxels with single fiber population pointing Z direction,
2. voxels with two fiber populations pointing X direction and voxels with two fiber populations pointing Z direction.

Averaged directions of diffusion were calculated in each group as well as the dispersion from the average diffusion direction. The results from the arms (single fiber population)

were compared with the corresponding diffusion directions found in the crossing area (two fiber populations).

The average directions of diffusion found in the arms of the cross served as references in analysis of reconstruction stability against the smoothing factor used for measured data interpolation in q-ball reconstruction algorithm. The angles between reference direction and directions of diffusion found in each of voxels belonging to the crossing area were calculated. To estimate the angle dispersion in a given diffusion direction, a median from all angles was calculated. The standard deviation cannot be used since the distribution of angles is not a Gaussian one. Measure of median angle has a simple physical explanation and it shows a cone around the reference direction that contains half of angles in the distribution. In other words, half of the diffusion directions in the explored collection fall into a cone with a median angle. Here, it is referred as dispersion cone angle (DCA). The more stable direction, the narrower the cone is.

3.3 Design of human brain experiments

The following section describes the application of presented methods in various experiments with *in-vivo* materials. The methods of diffusion evaluation were compared with human brain data. The deterministic tractography was used for reconstruction of connection between thalamus and the primary visual cortex. Thalamus was also segmented with probabilistic fiber tracking. As a proof-of-concept whole brain of q-ball data was analyzed. It was shown how q-ball imaging resolves fiber crossing in tracking.

3.3.1 First experiment: q-ball, Tensor and SD comparison

The aim of this experiment was to examine stability of diffusion direction estimation in diffusion tensor imaging and q-space methods (q-ball reconstruction by Funk-Radon transform and spherical deconvolution).

A double refocusing spin-echo sequence [27] was used for data acquisition. Diffusion weighted images were acquired in 252 gradient directions, equally distributed over the entire sphere.

Acquisitions of three healthy volunteers were performed on a 3 T MR scanner. First two subjects were measured at $b=1500 \frac{s^2}{mm}$ with $TE = 103$ ms, $TR = 1200$ ms, six slices with no distance factor and $3 \times 3 \times 3$ mm³ voxel size. Six successive measurements of each subject with the same parameters were performed for reproducibility estimation. Heads of the subjects were fixed to the coils by using hard foam pillows and holders to minimize the head motion during the measurement. The last subject was measured with four different b-values (from 1000 to $4000 \frac{s^2}{mm}$) with the shortest TE possible (82-126 ms), 6 slices, $3 \times 3 \times 3$ mm³ voxel size and three averages.

Data processing was performed as described in chapter 3.1, except spherical deconvolution.

Analysis of diffusion directions and model of distribution of angle differences

The different evaluation algorithms (e.g. Tensor model or q-ball reconstruction) or different acquisition modalities (e.g. number of acquisitions) led to different calculated diffusion directions in corresponding pixels. The diffusion directions in each voxel were compared and the angle between them was calculated:

$$\alpha = \arccos(|\mathbf{q} \cdot \mathbf{t}|) \quad (3.21)$$

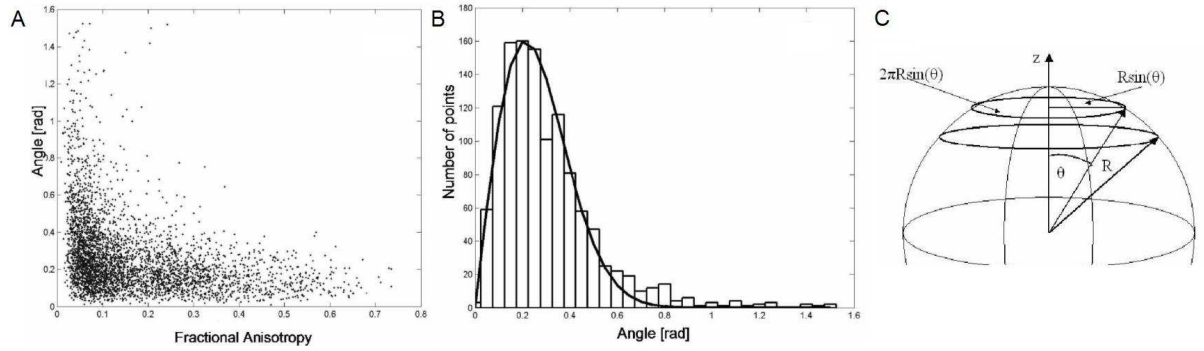


Figure 3.10. Method of the evaluation of angles differences model, a) Example of an angle distribution between q-ball reconstruction and the tensor model, b) Histogram of the angle differences for FA range 0.1 – 0.2, c) Calculation of the density function.

where \mathbf{q} and \mathbf{t} are vectors pointing the directions of the main diffusion in two different sets of diffusion angle reconstructions. The angle differences α were recorded for all voxels within the brain and plotted against the FA-value of the voxel. An example of an angle distribution between q-ball reconstruction and the tensor model is presented in figure 3.10a. The resulting angle differences were divided into small FA-ranges of 0.1 widths. Distributions in each of FA-bin were a subject of modelling. An example of such a distribution from one of the FA-bins was shown in fig. 3.10b.

It should be possible to model the distribution by a Gaussian model. However, the Gaussian shape had to be modified due to different point density for different angles. To explain that, let us consider a hemisphere with a number of random points with isotropic distribution. Next, let us calculate an angle between axis Z, which goes to the top of the hemisphere (fig. 3.10c), and each of the points. When the points have isotropic distribution, the number of points with given angle difference, which one can find, is proportional to the length of the circle drawn at this angle. (see fig. 3.10c). The desired distribution F should contain two parts: assumed Gaussian distribution (G) and the density function (DF):

$$F(\delta, \theta) = G(\delta, \theta) \cdot DF(\theta) \quad (3.22)$$

As described, DF depends only on the angle difference (θ), and it is given by ($R = 1$):

$$DF(\theta) = 2\pi \sin(\theta) \quad (3.23)$$

All constants can be omitted, due to further normalization. The final model of the angle differences, for a selected range of FA:

$$F(\delta, \theta) = e^{-\left(\frac{\theta}{\delta}\right)^2} \sin(\theta) \quad (3.24)$$

This is a one-parameter model and delta (δ) describes a position where 67% of results can be found for lower angles than δ . This statement is valid for δ from 0 to ca. 1 rad. (0 - 60 deg.), where Gaussian part dominates over sine. The δ parameter can represent the level of agreement.

The reproducibility was examined by fitting proposed model to angle difference distributions obtained from repeated measurements. Both, DTI and q-ball algorithm were examined in this way. Moreover, those two reconstruction techniques were compared between each other.

Smoothing effect and datasets comparisons

During the reconstruction of q-balls, sampled diffusion data have to be interpolated to the point located on the circles perpendicular to the direction of reconstruction. The interpolation in our case was done by a weighted sum of signals, where the weights were Gaussian functions dependent on angular distance between measured and interpolated points. The sigma of that function was set to 0.009 and in this case, the reconstructed point was a weighted sum of few (2 - 10) neighbour points. This value is the smallest possible due to the distances between reconstruction points.

In the case of the tensor model and 252 diffusion directions, the system of equations for calculation components of the tensor is highly over-determined. The tensor estimation returns the best fit of an ellipsoid to the obtained data, which are not ellipsoidal. In the case of a single fiber population, the both approaches may result in pointing the same direction of diffusion. However, in the case of multiple populations, the q-ball reconstruction shows the ODF with two directions of diffusion and the tensor model shows the averaged direction.

3.3.2 fMRI and DTI in optic radiation

The aim of this experiment was to reconstruct optic radiation connecting LGN located in thalamus with the primary visual cortex (V1) using only measurements for cortex region localization and fiber reconstruction.

Five health subjects were studied. Informed consent was obtained from all subjects before entering into the study. All measurements were performed on a 3 T MR-Scanner (Trio, Siemens, Germany) with an 8-channel head phased array coil. Each subject underwent measurement of T1-weighted anatomical images (3D MP RAGE) with a voxel size of $1 \times 1 \times 1 \text{ mm}^3$ were acquired (field of view, 256 mm; TR = 2300 ms; TE = 3.930 ms; TI = 1100 ms; flip angle = 8°).

Functional MRI measurement

The primary visual cortex (V1) was identified by fMRI-mapping of the cortical representation of visual angularity ([30][31][32][33]). The cortical map of polar angle representations changes its direction at the borders between neighbored visual areas. So V1 can be reliably separated from higher visual fields.

To map angular positions a conventional rotating wedge was presented (fig. 3.11a). The span width of the wedge was 12 deg, the wedge angle 45 deg. It rotated round the fixation point in 64 sec. The wedge itself had a dartboard pattern flickering with 8 Hz. The background luminance and the mean luminance of the dark and bright segments of the dartboard pattern were kept constant at 50 cd/m^2 . The dartboard used covered 24 deg of visual angle and consisted of 24 rings and 40 annular segments. Two sessions were measured with each 7 cycles. Mapping angular representations allowed not only identification of V1 but also its separation in an upper part and lower part representing inferior and superior quadrants of the visual field.

Blood-oxygen-level-dependent (BOLD) signal changes during stimulus presentation were measured by an interleaved spiral-trajectory gradient echo pulse sequence (TR 2000 ms; TE 34ms; flip angle, 90°). The voxel size was $2 \times 2 \times 2 \text{ mm}^3$; 25 slices were positioned perpendicular to the calcarine sulcus.

The left and right lateral geniculate nucleus (LGN) were identified in additional fMRI-session. Dartboard stimuli were presented in alternation to the left and right visual hemifield in blocks of 16 seconds (fig. 3.11c). Left and right LGN stimulation was repeated

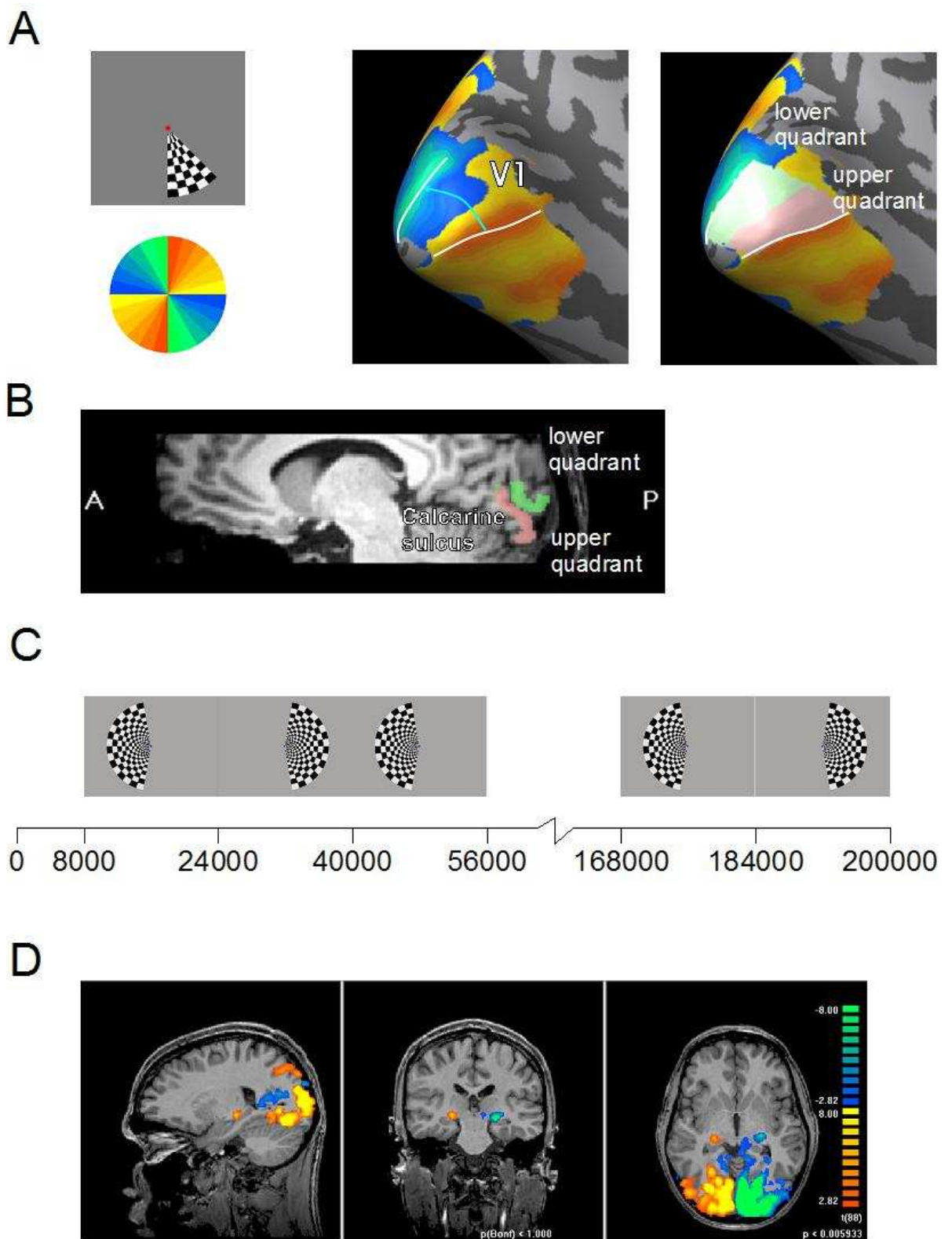


Figure 3.11. fMRI-Mapping of primary visual cortex and lateral geniculate nuclei (LGN). a) Mapping of cortical representations of visual angularity by rotating wedge stimulus. The primary visual cortex (V1) of the left hemisphere contains a mirrored representation of the right visual hemifield. On the basis of the angular map V1 can be identified and further partitioned into a dorsal and ventral part. b) The identified parts of V1 were projected back into 3D-space defining the underlying white matter as seed points for fiber tracking. c) Stimulation procedure for identification of right and left LGN. d) Typical activation pattern to the stimulation described in C.

4 times. BOLD signal changes were measured by echo pulse sequence (TR 2000 ms; TE 34ms; flip angle, 90°) with a voxel size of 3x3x3 mm³.

DTI measurement

The diffusion data were acquired with a spatial resolution of 1.4x1.4x1.4 mm³ using a double refocusing spin-echo sequence[27]. Dataset, containing 40 slices through the visual cortex and CGL was measured with the following parameters: TE = 94 ms, TR = 6000 ms, b-value: 800 s²/mm, GRAPPA parallel imaging with an iPAT factor = 2. Data was composed of 16 averages measured in four acquisitions. Diffusion images were measured in 12 non-collinear and equally distributed directions derived from the vertices of an icosahedrons. Such an acquisition was repeated four times for better signal-to-noise ratio. The four data sets were motion corrected and coregistered to each other by using routines of Statistical Parametric Mapping software (SPM2, Welcome Department of Cognitive Neurology, London, UK) and then averaged.

fMRI analysis

For preprocessing, analysis and visualisation of the fMRI-data Brain Voyager QX 1.38 (Brain Innovation, Maastricht, The Netherlands, www.BrainVoyager.com) was used. Retinotopic maps were projected to and analyzed on inflated representations of the cortical surfaces. In Brain Voyager an automatic procedure is implemented to segment the white matter from the anatomical volume and to identify the border between white and grey matter. A triangular mesh of this border can then be created and used as a surface model. After the automatic procedure each segmented hemisphere was controlled for topological errors and carefully manually corrected. In additional steps, the cortical surfaces were inflated.

For the analysis of the retinotopic mapping experiments, cross correlation analyses were applied. Polar angle representations were determined by finding the time lag values at each voxel that maximized the correlation between signal time course and model function. The borders of the visual fields (V1, V2, V3, V3A and V4) were identified by manually tracing reversals in the pattern of the polar angle maps [34]. On the basis of the angular maps the representations of upper and lower quadrants within V1 corresponding to the dorsal and ventral lip of the calcarine cortex were identified, too. The surface representation of V1 was projected back into 3D-space and the underlying white matter was defined as region of interest (ROI) (fig. 3.11b).

Right and left NGL were identified individually by contrasting BOLD-signals to right and left hemifield stimulation by calculating simple t-tests. On the basis of the activation pattern ROIs for the left and right NGL were defined (fig. 3.11d).

Structural data were carefully coregistered to DTI-data and coordinates of detected ROIs were converted into Matlab-format establishing the seed points for fiber-tracking.

DTI analysis and tractography

The dataset were de-noised by a convolution with a Gaussian kernel. Tensor data were obtained by means of Moore-Penrose pseudo-inversion and diagonalized for obtaining the eigenvalues and eigenvectors, according to the frameworks given in [5, 7, 10, 11]. Fiber tracts were calculated using self-written program, partially running under MATLAB and partially as a compiled C++ code. Fiber tracking algorithm was following the main direction of diffusion, defined as the direction of the eigenvector corresponding to the largest eigenvalue of the diffusion tensor. The step of the fiber tracking algorithm was

fixed to the value of the half of a voxel size (0.7 mm). The computer program was stopping tracking when the FA was lower than 0.1 or the angle difference between two consecutive steps were larger than 55 deg. The fiber tracking algorithm was starting from 27 seeds equally distributed within each starting voxel and the seed points were arranged in a Cartesian grid. The voxels with $FA > 0.2$ were chosen as the starting voxels. The voxels lying beyond the anterior boundary of CGL as well as the voxels above and below the VC were excluded from the starting points. The hemispheres of the brain were processed separately. Only fibers longer than 15 voxels (c.a. 22.5 mm) were stored for further analysis. The optic radiation was reconstructed by selecting only those fibers that cross or end in the surrounding of both ROIs. The margin for VC ROI was set to 5 - 8 voxels (7 - 11.2 mm) and for the CGL ROI was set to 1 - 2 voxels (1.4 - 2.8 mm). The resulting fiber tracts were converted to BrainVoyager's format and separated into bundles, according to the dorsal and ventral segmentation of V1.

3.3.3 Third experiment: Probabilistic/Stochastic approach

The aim of this experiment was to examine connectivity of thalamus with other cortical areas in the brain, using probabilistic fiber tracking.

Diffusion weighted images using 12-directional sampling scheme were obtained from three healthy volunteers. Before each measurement, an informed consent was obtained from the subject. The acquisition parameters were: TE = 90 ms, TR = 12000 ms and b-value = 800 s²/mm, GRAPPA parallel imaging with an iPAT factor = 2. The subject's head was fixated in the head coil using pillows and a cotton belt. Images were acquired with an isotropic resolution of 2 mm.

The thalamus area was manually selected slice by slice to create a starting region of interest. Probabilistic fiber tracking algorithm was started from each voxel of selected thalamus area for 1000 times. Connectivity matrices of all voxels were calculated as described in sections 2.7.2 and 3.1.3.

The destination regions of interest were manually selected as well. Four regions were marked: *prefrontal-temporal area*, *motor area*, *somato-sensory area* and *parieto-occipital area*. The regions contained the gray matter as well as 3 mm of underlying white matter, because the tracking algorithm cannot enter the grey matter area, due to low FA value. The regions were stored as Boolean matrix with size equal to the size of images volume. Regions were exclusive.

The connectivity matrices were multiplied by the Boolean masks of destination region of interest. In this way only counts that were present in given destination area remained. In the next step, the integrals were calculated for each voxel and each destination area. All thalamus voxels were classified to one of four groups, depending on the highest connection probability with destination regions.

3.3.4 Fourth experiment: q-ball whole-brain fiber tracking

The aim of this experiment was to make a proof of the concept, that q-ball imaging can be performed for the brain volume in time suitable for clinical applications. Moreover, the second aim was to show examples for cases where standard DTI fails due to multiple fibers populations, which cannot be properly analyzed.

Diffusion weighted images of five volunteers were acquired in 252 diffusion directions with TE = 90 ms, TR = 14000 ms and b-value = 1500 s²/mm, GRAPPA parallel imaging with an iPAT factor = 2. Imaged volume was sampled with isotropic resolution of 2 mm.

Whole cerebral volume was acquired. As in previous experiments, subject's head was fixated, using foam pillows and a cotton belt.

The dataset were reconstructed using both DTI and q-ball reconstruction by Funk-Radon transform as described in sections 3.1.2 and 3.1.2. The direction of diffusion were extracted and the deterministic fiber tracking algorithm was applied as described in sections 2.7 and 3.1.3.

The starting regions were chosen in vicinities of regions known for fiber crossing, like corona radiata or pons. The extent of tracts was compared between methods. Crossing regions were found and the behaviour of tracking algorithm using DTI and q-ball were compared.

Chapter 4

Results

In this chapter, the results from the experiments are presented in two parts: validation and application. The order remains from the methods chapter. In next sections from 4.1 to 4.3, the examination of different materials and tracking algorithms is described.

A validation of the implemented algorithms was also performed. The fiber tracking algorithms were tested using digital phantoms. The quality of results obtained with the DTI, the q-ball and the SD method was evaluated using pig's spine phantom and an *in-vivo* measurements.

The application part starts in section 4.4 with an *in-vivo* deterministic (section 4.5) and probabilistic tracking (section 4.6). Finally in section 4.7, the tracking results from the whole brain imaging with the q-space methods are presented.

4.1 Digital phantoms

Digital phantoms can test the implemented algorithm. They allow easily adjusting the program code by comparing an output with well known input. Mistakes and program bugs can be removed. A tracking algorithm may return a false-positive result. Therefore, it is important to test tracking algorithm (here called *the tracker*) before it is used on measured data. This assures the user that obtained result is a true-positive one.

Each simulated phantom consists of three matrices describing three eigenvalues, three eigenvectors and one FA value in each of 64x64x64 simulated points. Key results from the tracker validation through the digital phantoms are presented in fig.4.1. The planes on plots are the cross-sections through the FA matrix. In those examples the FA is constant in all voxels and it equals to 0.8 with single fiber population. In dual fiber population voxels FA was set to 0.63 and in case of triple fiber population was set to 0.43.

The step size of the fiber tracking algorithm was 0.5 of the voxel size. The angle threshold was set to 0.3 rad and FA cut-off value was 0.1. Since this was synthetic data, thresholds did not play a role and step size was important only in case of spiral phantom. The starting points were always selected at one of the volume boundary.

Basis directions phantom

The tracker returned perfectly straight fibers in assumed directions. As shown in fig.4.1a, the fibers fulfil the artificial fiber bundle, here marked as white areas. Fiber's colours are represented like on colormap. The number of fibers started equalled the numbers of fibers that reached the other volume boundary. The stop conditions worked as assumed in case

of low FA voxels insertion, as well when diffusion direction was replaced in some voxels to a perpendicular ones. Fiber tracking was terminated in those areas.

The tracker responded as planned to the input data set, reconstructing straight fibers.

Diagonal directions phantom

The single population fibers were simulated in those phantoms. The simulated tracts were placed on the diagonals of simulated volume. The tracker returned, as in previous case, the number of fibers reaching the opposite boundary of the volume was the same as the number of the starting points. Figure 4.1b shows two examples of diagonal fibers reconstruction. This test shows that the algorithm properly deals with diffusion directions with all non-zero components.

Spiral phantom

The curvature handling was the last feature tested in phantoms with single fiber population. The fibers curvature were successfully restored, as shown in fig.4.1c. That result should be compared with fig.3.8, showing the assumed phantom model.

This test proved that tracker is able to reconstruct not only straight fibers but also wide spectrum of curves. The fibers deviate from the assumed track, but for range of 2π (full rotation) it is two voxels. It can be observed at the fiber ends (top of the volumes in fig.4.1c).

Crossing phantom

Figure 4.1d shows results of the crossing test. The crossing region was placed in the centre of the simulated volume. The tracker was able to reconstruct fiber paths in both cases of two fibers and three fibers crossing. All fiber tracts reached the opposite side of crossing area. The presence of second diffusion direction in a voxel did not distract or interfere with the fiber reconstruction for q-ball evaluation.

Performed tests show that implemented tracking algorithm properly reconstructs fibers using diffusion directions and the crossing regions can be solved. The number of fibers that successfully passed the crossing region is the same as the number of starting points.

4.2 Comparison of artificial phantoms quality

Artificial fibers used in a MR phantom allow testing the MR sequence and diffusion calculation routines. Presented results show examinations performed in order to simulate anisotropy environment.

Rhubarb and asparagus

An example of colormap measured using rhubarb submerged in agar gel is shown in fig.4.2a. The diffusion direction was calculated properly. The green colour represents Y axis of laboratory reference frame. The obtained mean FA level was **0.14** for rhubarb in water for b-value $400 \frac{s^2}{mm}$ and **0.09** for $800 \frac{s^2}{mm}$. In case of phantom made of asparagus the FA values were obtained at similar level, **0.09** and **0.05** respectively. The agar gel fixation did not improve the mean FA value, which both were below 0.1. However, agar gel minimized the motion induced ring artefacts.

Some voxels showed high FA (> 0.4), but this should be rather related to noise, than to actual measurement.

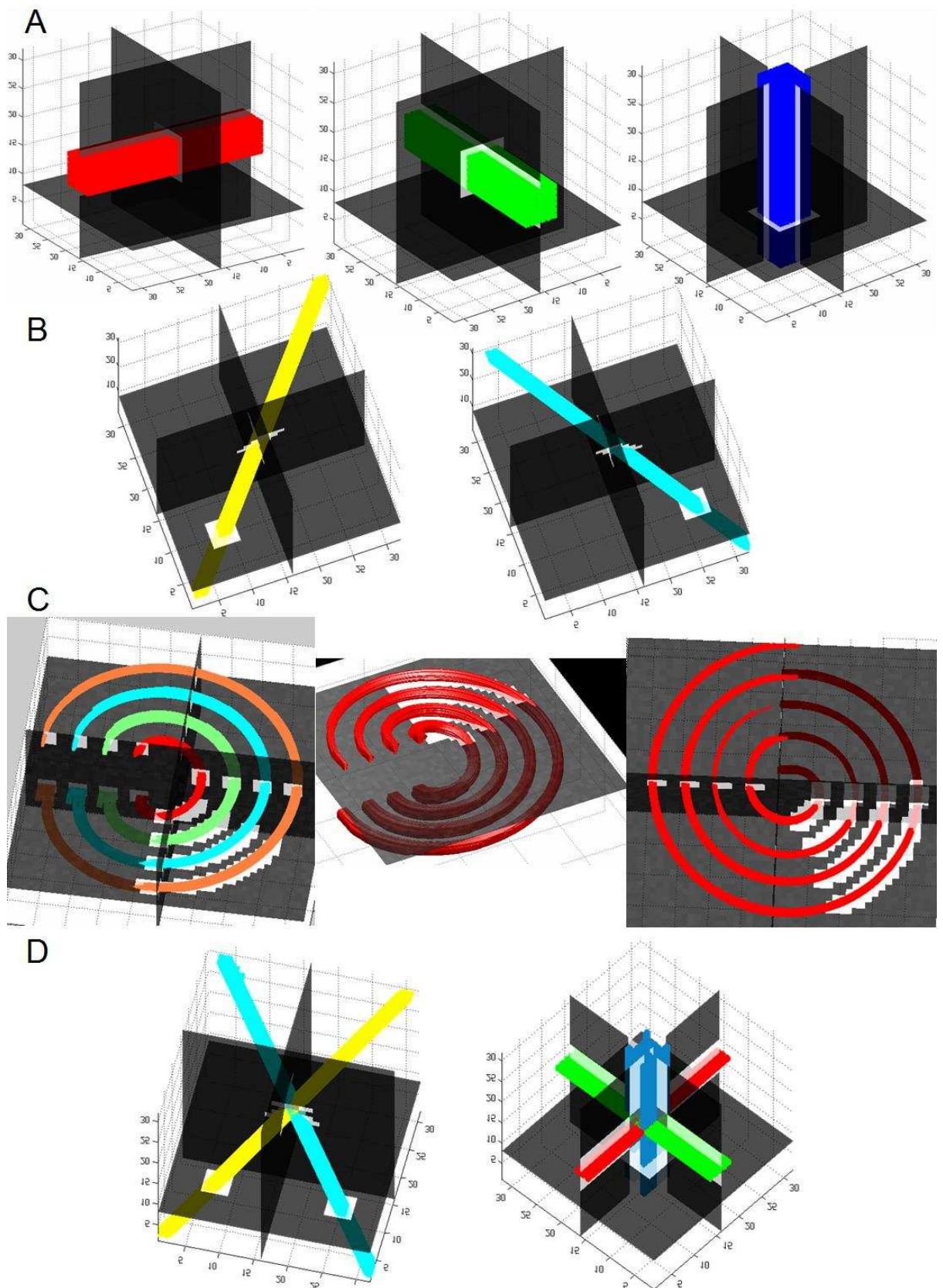


Figure 4.1. Digital Phantoms. Selection of results of tracker in digital phantoms showing the capability of algorithm to move through crossing regions. a) Tracking results in basis (X,Y,Z) directions from 6x6 starting region. b) Diagonal fibers. c) Spiral fibers, showing proper curvature reconstruction. d) Crossing fibers. Two diagonal populations and three populations in basis direction, showing algorithm's capability to reconstruct crossings.

Table 4.1. Results of FA measurement in biological phantoms. The range describes the minimal and maximal mean values among different phantom regions.

	Mean FA range
Rhubarb in water	0.087 – 0.142
Rhubarb in agar gel	0.051 – 0.051
Rhubarb in water (with leaf)	0.045 – 0.09
Asparagus in water	0.095 – 0.1
Asparagus in agar	0.07 – 0.08

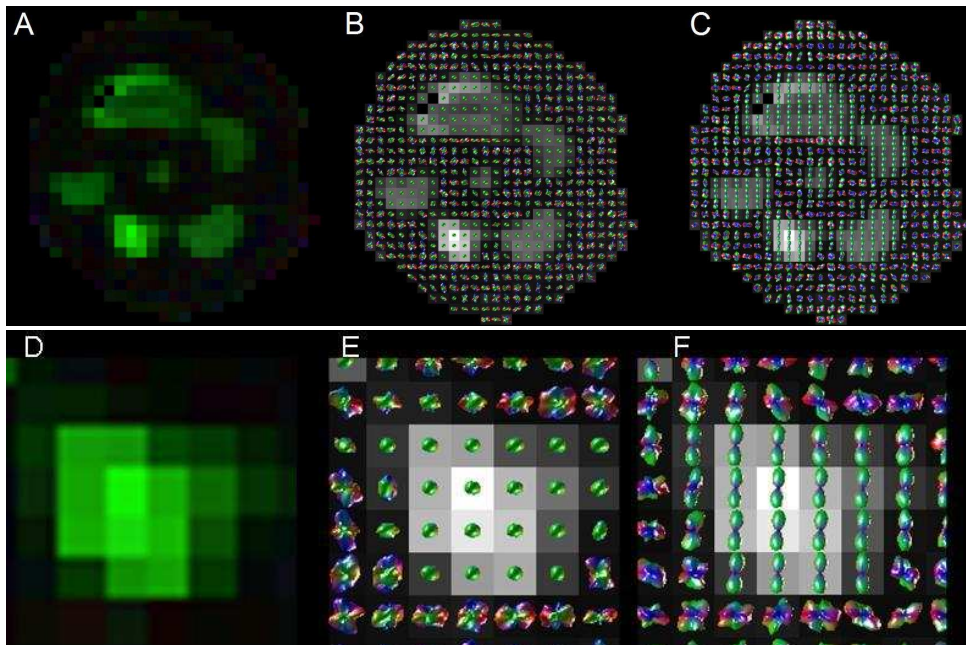


Figure 4.2. Results of rhubarb in agar gel measurements. a) colormap from DTI b) ODF from q-ball c) rotated ODF from q-ball for better shape visualization, d,e,f) magnification of selected rhubarb for better visualisation.

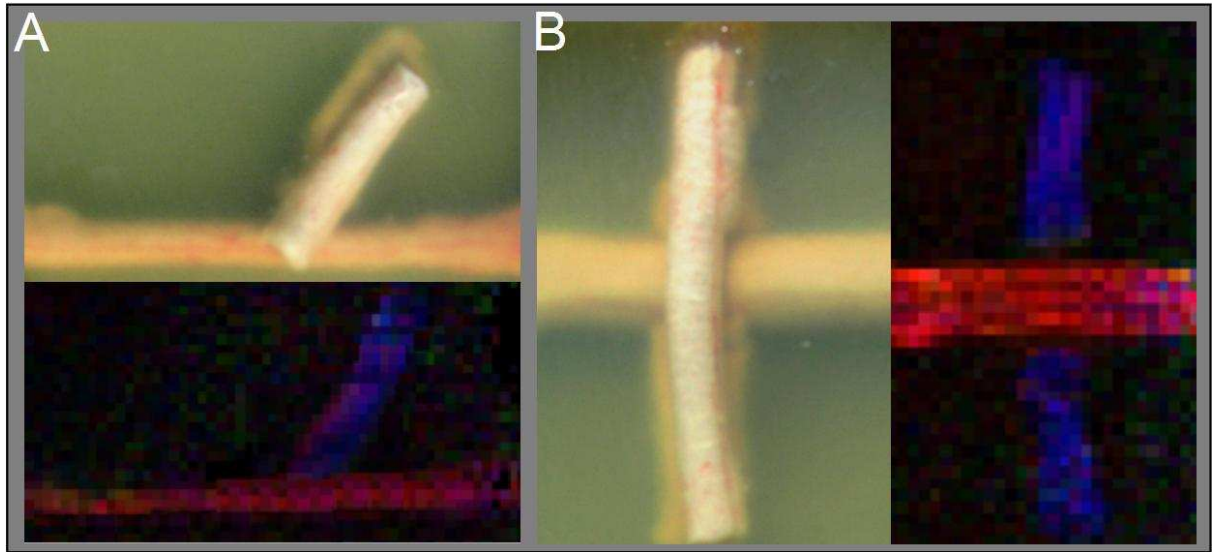


Figure 4.3. Photos of spinal cords in agar gel compared with the resulting colormap from DTI experiment.

The obtained FA values are much lower than FA values usually found in the human brain. Therefore, such phantoms should not be used for anisotropy testing. The FA results for testes phantoms were listed in table 4.1

The direction of diffusion was recovered in case of tensors and q-ball reconstruction. Figures 4.2b and 4.2c show q-ball shapes. For better visualization of the q-ball peanut shapes the Y axis was rotated $\frac{\pi}{2}$ on 4.2c, so the diffusion direction is now parallel to image axis.

Dyneema and capillaries

The usage of non-biological material did not bring expected results. No signal were found in bundle of capillaries with internal diameter of $9 \mu\text{m}$. This can be explained by the small effective density of protons in the bundle and by susceptibility inhomogeneities. The signal loss in the bundle area destroyed the measurement. No FA or colormap could be evaluated.

The Dyneema fibers were fixated on a wooden and plexi-glass frames. The measurements showed only motion artefacts. Even if signal was found in some voxels, the diffusion direction was not properly calculated.

Spinal cord

The best results were obtained from the genuine axons. The prepared pig's spinal cords render consistent and homogeneous FA values similar to those normally found in the human brain. The FA vaules were found in range from 0.4 up to 0.6. The colour matches the direction orientation of the phantom in MR scanner.

4.3 Fiber crossing phantom

The crossing phantoms were built using fresh pig's spinal cords submerged in agar gel. The colour maps, derived with the tensor model were presented in fig. 4.3C and D. The colours in the arms of the cross have direction corresponding to the position in MR

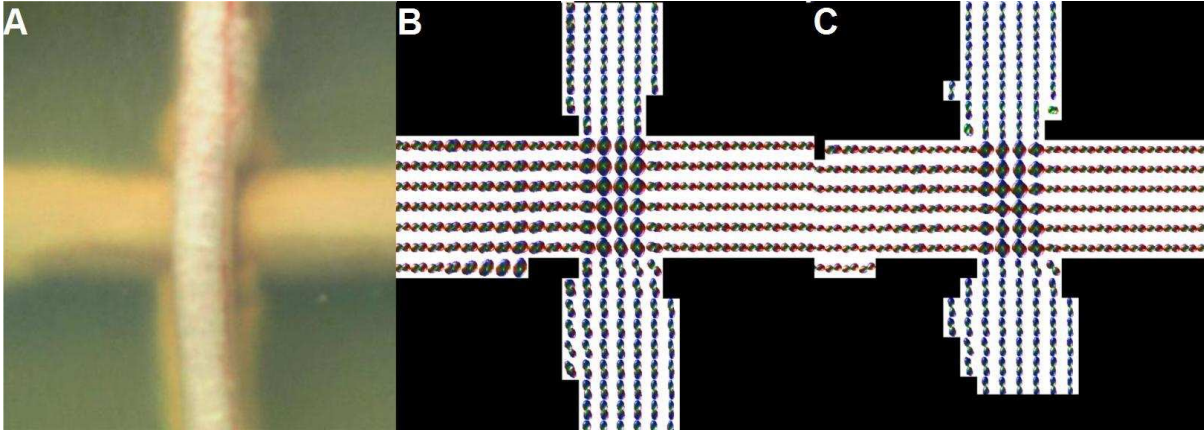


Figure 4.4. Phantom for simulation crossing areas and visualization of q-balls. A) Photo of pigs spinal cords submerged in agar gel used in measurement. B) Q-ball shapes obtained with b-value of $1000 \frac{s^2}{mm}$ C) Q-ball shapes obtained with b-value of $2000 \frac{s^2}{mm}$.

scanner. However, in the crossing region dominates red colour. Tensor model was not able to resolve the crossing and the resulting direction of diffusion in that region is determined by dominating fiber. In this case, the red (axis X) direction rule out the other direction of diffusion.

Q-ball reconstruction was able to identify regions containing the spine properly. Figure 4.4 shows the photo of the crossing phantom aligned to the MR image and q-ball reconstruction. Both low b-values visually reveal the directional structure of the phantom. The ODF in arms of the phantom have a peanut-shape, which represents the single fiber population, as assumed. The directions of diffusion are parallel.

The analysis of directions acquired with b-value $1000 \frac{s^2}{mm}$ in arm-regions with standard reconstruction parameters ($\sigma = 0.009$) shows that the dispersion cone angle (DCA) is equal to 4.03° (degree) for X direction (group A) and 4.42° for Z direction (group B). In case of b-value $2000 \frac{s^2}{mm}$ those values are equal respectively 3.80° and 3.80° .

The crossing region of the phantom is resolved by the q-ball approach. The q-ball shapes have two distinct peaks pointing in both directions of the fibers.

Stability of diffusion direction estimation in case of double fiber population (group C) resulted in a DCA of 12.7° in X direction and a DCA of 10.8° for $1000 \frac{s^2}{mm}$. For b-value of $2000 \frac{s^2}{mm}$, those DCAs were equal to 6.6° and 5.5° .

Q-ball reconstruction incorporates data interpolation and smoothing or measured signal blurring (figure 4.5). The influence of the reconstruction stability was examined by calculating DCA in the crossing area against the smoothing kernel σ from reconstruction algorithm [6]. The blurring influence is shown in figure 4.5 for both b-values and directions in the crossing area. The influence of smoothing was moderate up to a kernel of 0.25° . For larger smoothing kernel, the DCA increased. A smoothing kernel of 0.6° led to an increase of DCA values by about 60 %.

4.4 SD, q-ball and tensor results comparison

The following comparison was performed on human brain data. When a visual inspection of colourmaps provided by DTI, q-ball and SD is performed, the differences between the colours are not noticeable. However, differences between those methods exists.

The level of signal attenuation is used in all reconstruction techniques. On the other hand, an MR signal cannot drop below the noise level, so the level of attenuation may not

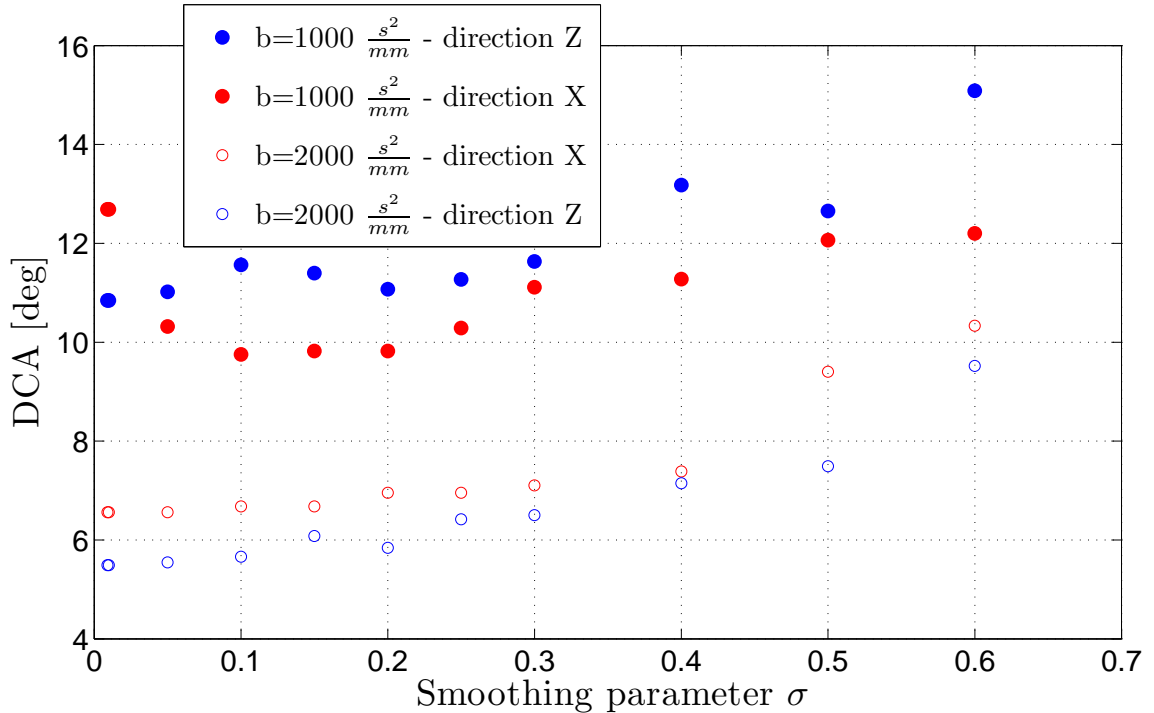


Figure 4.5. Values of the dispersion cone angle calculated from the crossing area voxels. Results for b-values of 1000 and 2000 $\frac{s^2}{mm}$ were plotted against smoothing parameter used in q-ball reconstruction algorithm.

be properly measured in some voxels. Voxels, in which more than 10 % of measurements among 252 diffusion directions were below the noise level, were rejected from analysis. It is easy to observe that most of them are located for low FA ranges (fig. 4.6a).

The general fractional anisotropy (GFA) shows complete linear dependence on FA, as shown in figure 4.6b. Only points, which do satisfy the 'noise condition', were shown. The noise effect leads to decrease in GFA.

The histogram in figure 3.10b (p.49) shows the angle distribution between FA 0.1 and 0.2. The result of fitting is presented as a solid line. The proposed model fits to the resulted distribution of angles which suggests that distribution is governed by a Gaussian behaviour.

The agreement between the tensor model and q-ball evaluation was checked by analyzing the δ value of the fitted Gaussian line. From six successive measurements, the main direction of diffusion was calculated by means of the tensor model and the q-ball reconstruction. The results are compared within the following subchapters.

4.4.1 Main direction of diffusion

A direct comparison of evaluated main directions of diffusion between the tensor model and q-ball reconstruction, the tensor model and SD, as well as between the q-ball and SD is presented in fig. 4.7a. For this comparison, a b-value of 1500 $\frac{s^2}{mm}$ was chosen. This makes measurement time suitable for clinical applications. The highest observed differences were for comparison between the tensor model and SD. Comparison between q-ball and SD shows the best agreement.

The differences are present only for low FA regions. Above a FA of 0.3, the differences between methods do not change with FA.

Figure 4.7b shows the reproducibility of reconstructed directions of diffusion obtained

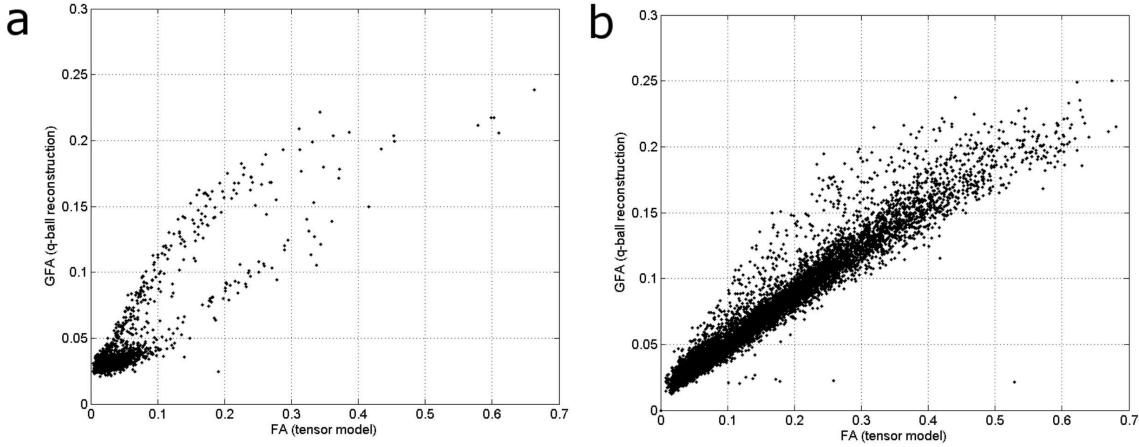


Figure 4.6. Relation between general fractional anisotropy obtained by means of q-ball reconstruction and fractional anisotropy provided by the tensor model shows linear behaviour. a) Points, which do not satisfy the noise condition (see text). b) Remaining points, after rejection of the points influenced by the noise.

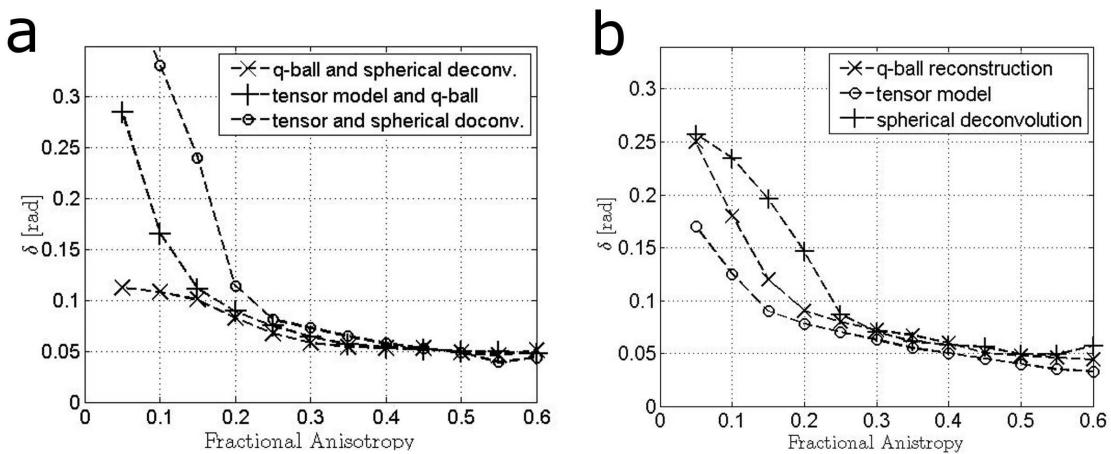


Figure 4.7. Main direction of diffusion. a) Differences in main diffusion direction between reconstruction methods using the same dataset. b) Reproducibility of main diffusion direction estimation calculated by comparing results from successive measurements.

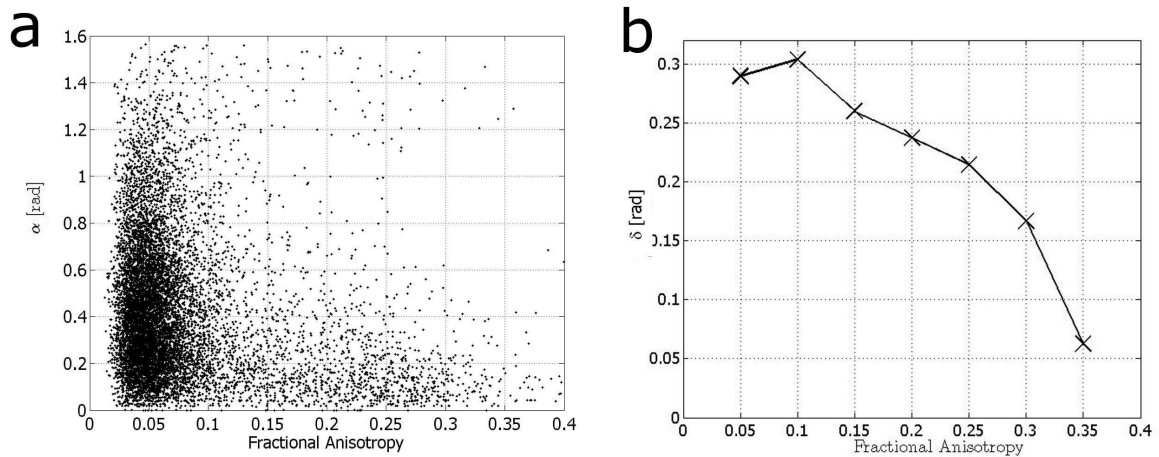


Figure 4.8. Results for second direction of diffusion. a) Angle differences distribution found for q-ball reconstruction in successive measurements. b) Consistency of second diffusion direction when comparing q-ball reconstruction and spherical deconvolution.

in successive measurements of the same region. The highest reproducibility was obtained by the tensor model. All methods show similar reproducibility in regions with single fiber population (high FA).

For low FA values, the tensor model shows the most stable behaviour.

The results of main diffusion direction estimation of q-space methods described here do not differ more than 3 - 6 degrees. The major differences are observed for FA in range from 0 to 0.2 where methods had to deal with significant noise influence and isotropic diffusion situation.

4.4.2 Second direction of diffusion in q-ball reconstruction and SD

A second direction of diffusion can be revealed by q-ball reconstruction and SD, but not by means of the tensor model. The grading of diffusion directions in the q-ball/SD shape was according to the peak value in the reconstructed shape. The second main directions of diffusion underwent the same methodology like in case of comparing the main directions of diffusion in q-ball datasets. One reason for observed large angle values can be an exchange of directions priority in the successive measurements. Therefore, in the next step, the angles between the second main direction of diffusion from the first dataset and all directions of diffusion from the second dataset were calculated and the minimal angle was chosen.

The angle distributions of differences between second directions of diffusion in case of q-ball and SD measured in successive acquisitions were similar. As an example of angle distribution, the results for q-ball reconstruction is presented in figure 4.8a.

Second directions of diffusion were also compared between q-ball reconstruction and SD in same way the main directions were compared in fig 4.7a. In this case voxels with crossing fibers were found for FA values up to 0.4. Figure 4.8b shows that, like for main diffusion directions agreement increases with FA value.

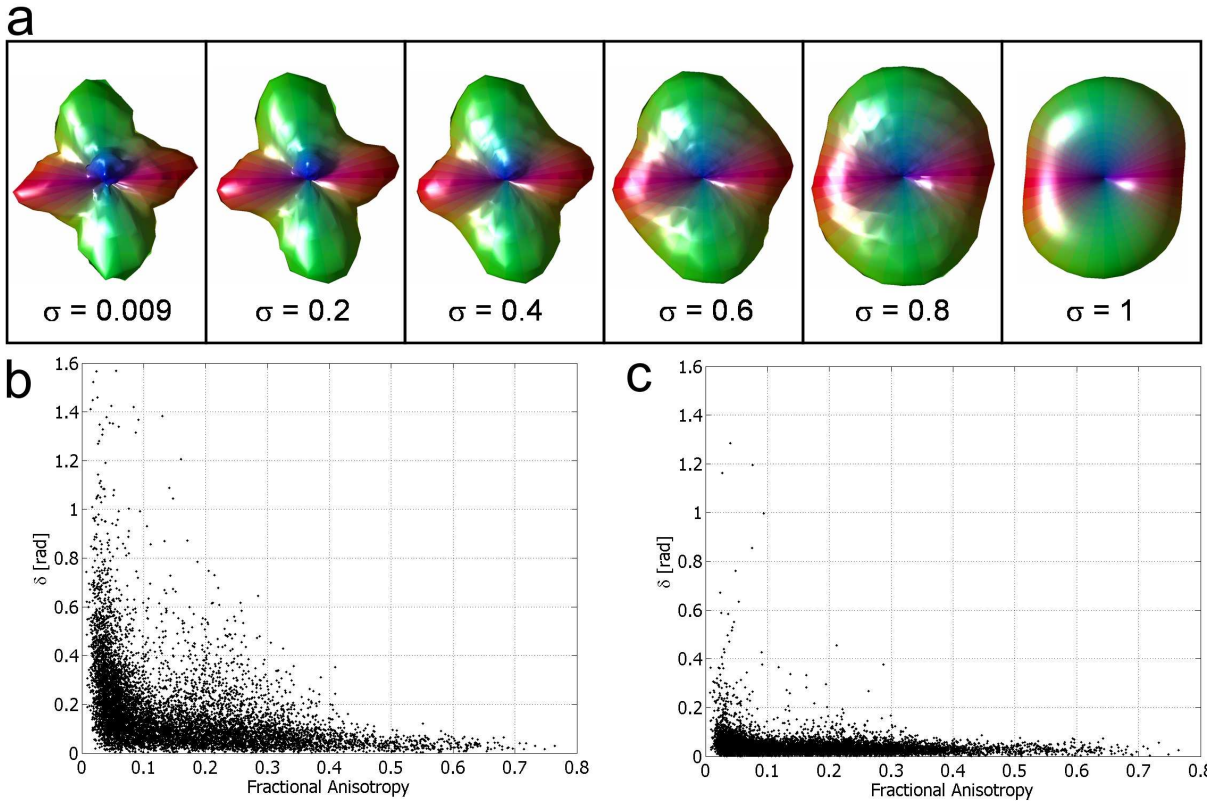


Figure 4.9. Q-ball function changes as interpolation kernel increases a). Distribution of angle differences between main directions of diffusion from the tensor model and q-ball with b) standard interpolation kernel and c) high-smoothing interpolation kernel.

4.4.3 Influence of smoothing and b-value

The evaluation of the agreement between DTI and q-ball evaluation was then repeated, but using large interpolation kernel (σ) for the Gaussian weighting, while reconstructing the q-ball data.

Two distinct directions of diffusion in q-ball shape disappear when the σ is increased (fig. 4.9a). As we can observe, the two directions are replaced by the averaged direction of diffusion.

Two results of q-ball reconstruction, with a standard interpolation kernel ($\sigma = 0.009$) and highly smoothed ($\sigma = 1$) one were compared to the main direction of diffusion of the tensor model within one dataset (fig 4.9b,c).

The described comparisons between tensor model and q-ball evaluation and between tensor model and SD were repeated for different b-values. The distributions of angle differences change slightly in relation to b-value (fig. 4.9). The results included in fig.4.7 and fig.4.10 come from different subject, this can explain slight difference for $b = 1500 \frac{s^2}{mm}$. No trend could be found for the change of δ -values in dependence on the b-value.

4.5 fMRI and DTI

The described approach was able to reconstruct the optic radiation in 7 out of 10 acquired hemispheres. In 6 hemispheres separation of the resulting fibers into an upper bundle and lower bundle was possible. In some cases, the evidence for a third bundle connecting LGN with central part of V1 was found.

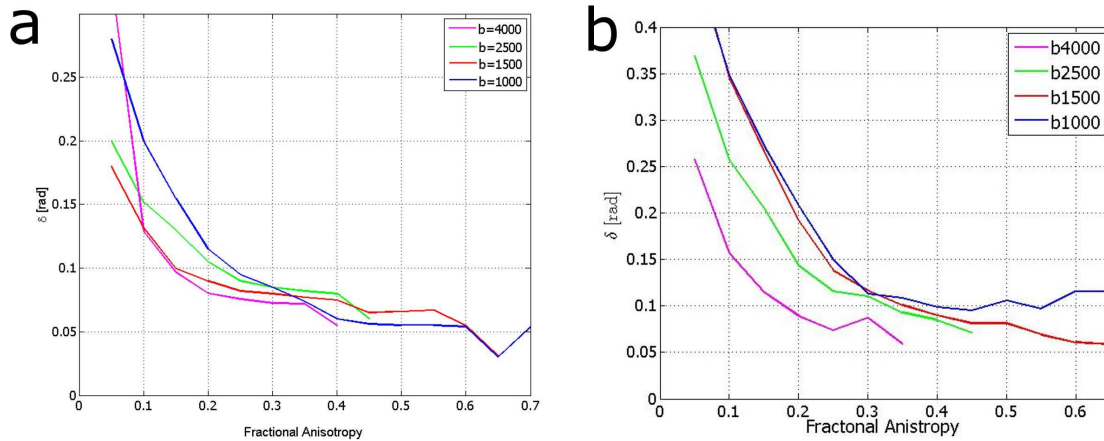


Figure 4.10. Reproducibility of main diffusion direction estimation calculated by comparing results from successive measurements. Evaluation for different b-values and for q-ball reconstruction (a) and for spherical deconvolution (b).

4.5.1 DTI results

After calculation of eigenvalues and eigenvectors and FA index, all voxels within the white matter were selected from the posterior half of the processed hemi-sphere of the brain using a simple FA threshold (> 0.1). Multi-seed fiber tracking from all points of the white matter would result in a large number of fibers, which major part of them is not in the scope of interest. Most of them do not cross both LGN and V1. Therefore, only voxels from one hemisphere were taken as the seed points. Hemispheres were analyzed separately. Multi-seeding factor was reduced to four starting points per one voxel.

The ventricles and the ROIs for the DTI tracking were shown in figure 4.11a. According to the anatomic information the fibers should be rather in the transversal plane and go around the ventricle forming sort of semicircle called the Mayer's loop and then straight to the visual cortex.

All the fibers tracked from all points within the brain were filtered out to only those, which cross the vicinity of the ROIs provided by the fMRI. The average total number of fibers of c.a. 70.000 was reduced to range of 1000 - 5000 valid fibers, satisfying the condition mentioned above.

The resulting fibers connecting the CGL with the primary visual cortex are shown in figure 4.11b. The bundle consists of two parts (red and green) described in the following section. The shape of the resulting fibers is fulfilling the expectations derived from the anatomical knowledge.

4.5.2 Segmentation of the fiber bundle

Fibers connecting the CGL with V1 were divided according to their end position in the visual cortex area. This division is shown in figure 4.11b by different colours of the fibers and then on following figures. The projection of the fibers to coronal and axial slices is presented in figure 4.11c, showing the separation of the fibers. Figures 4.11d and 4.11e show two compartments of the fibers separately. The composite 3D reconstruction of optic pathways from both hemi-spheres is presented in figure 4.11f. The ROI from fMRI calculations are shown on subplots of figure 4.11, as well as, reconstruction of CSF in the ventricles is shown in figures 4.11a and 4.11b.

The reconstructed fibers match data from post-mortem studies presented in anatomic

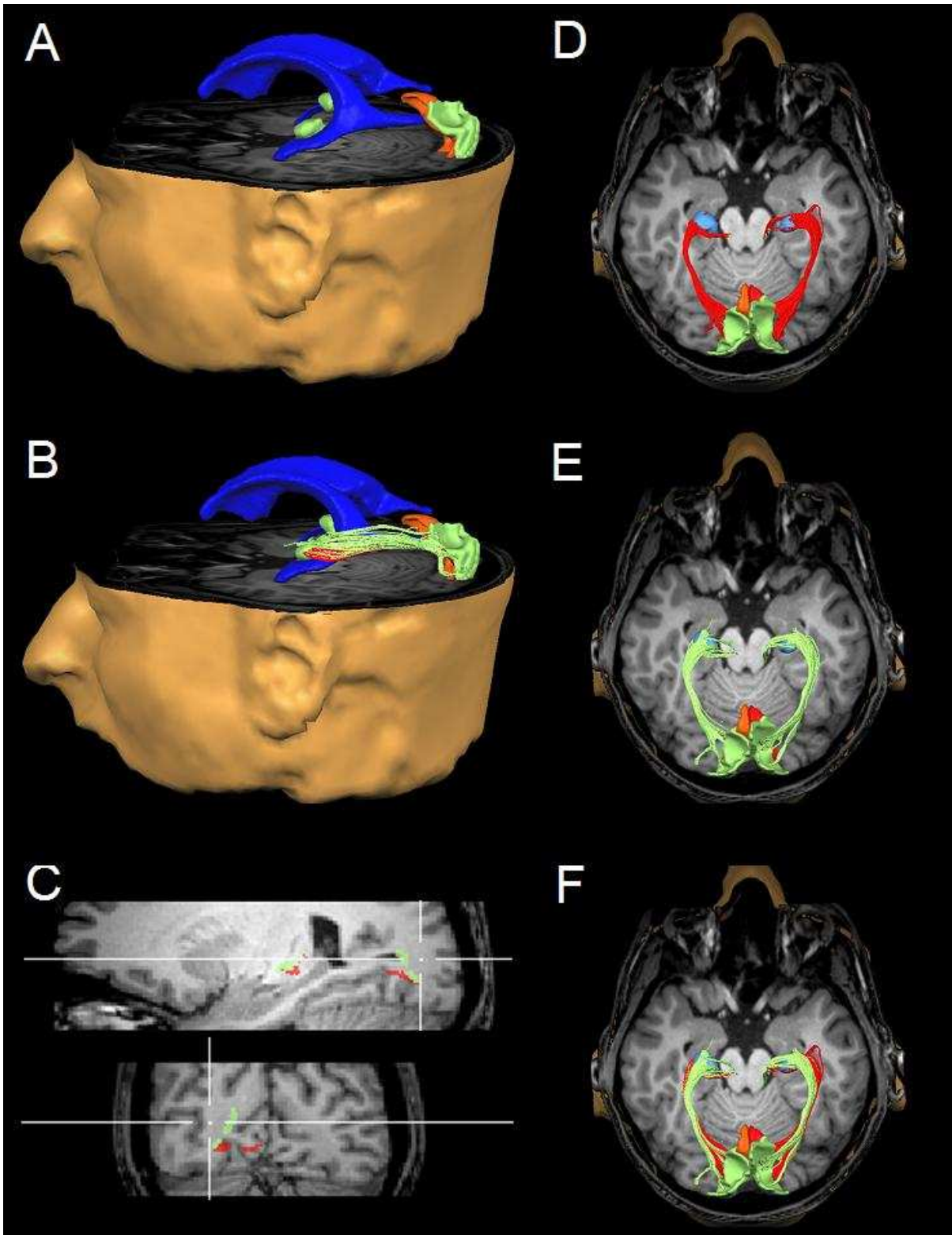


Figure 4.11. Left and right optic radiation in a typical subject. a,b) Regions of interests (upper and lower part of V1 and NGL) as seed points for fiber tracking, in B with the resulting optic radiation of the left hemisphere. c) Segmented fibers of B overlaid on a sagittal and axial slice demonstrating a clear separation in different bundles projecting to the dorsal and ventral part of V1. d,e,f) Ventral (D), dorsal part (E) and both parts (F) of the optic radiation in both hemispheres.

atlas. The curvature, starting and ending points are reproduced. The atlas data is an averaged image in population. Here, the pathway is reconstructed in-vivo. Therefore, one can be quite sure that reconstructed volume of fibers connects the CGL with V1 in each of volunteers.

4.6 Probabilistic approach

The results of the probabilistic fiber tracking in this work are described in three subsections. First one describes the parameters used to adjust tracking algorithm parameters such as the step size, discrimination angle, FA threshold (section 4.6.1.)

In the second phase (section 4.6.2), the proposed algorithm was tested in digital phantoms. The coherence of fiber tracts for various FA levels was checked as well as influence of crossing regions.

The last part in section 4.6.3 was an application of the algorithm to clinical data. The probability of connection between the thalamus and cortex was examined.

4.6.1 Adjustments of the random direction generator

The distribution of directions represents the shape of a PDF from DSI experiment; however there are differences between voxels with well organized fibers, crossing regions and voxels containing mainly the fluid. The width of presented distribution is controlled by the σ parameter; therefore, it is possible, by changing the σ parameter, to change the scatter radius of distribution.

The mathematical framework described in section 3.1.3 describes the general problem of generation of the random angle deviation. The optimal function choice should propagate fibers along the directions diffusion where FA levels are high. Alternatively, the scatter of random should increase as anisotropy disappears.

The most natural way of generation scatter generation is Gaussian. Two Gaussian curves are shown in figure 4.12a. The blue one represents the desired histogram of angle differences from the main diffusion direction located in position 0. The high FA values should result in directions generated close to the main direction. Therefore, the Gaussian function is narrow (small FWHM).

The yellow curve represents the desired distribution for significantly lower FA than in the previous case. Angles with higher values should be generated. The desired distribution is wider. This example represents a Gaussian (function G) in fig. 4.12.

For the reasons described in the methodology subsections 3.1.3 and 3.3.1, the desired distribution have to be corrected by the density function. Figure 4.12b presents both desired Gaussian distribution corrected in order to be used in the spherical coordinates. Note that the number of generated points decreases around value 0° .

In this approach, the number of generated points per area unit decreases as the distance from the main diffusion direction increase. In this way, the overestimation around the main diffusion direction is removed. With corrected the Gaussian distribution the generated random diffusion directions form a probability distribution function (PDF) which reflects the PDF obtained by HARDI measurements.

The presented corrected Gaussian functions are normalized, so the function's integral is equal to 1. It fulfils the form of the eq. 3.12.

Since the numerical forms of the desired distribution are known, the cumulant and its inverse form have to be calculated. Both functions can be found using numerical

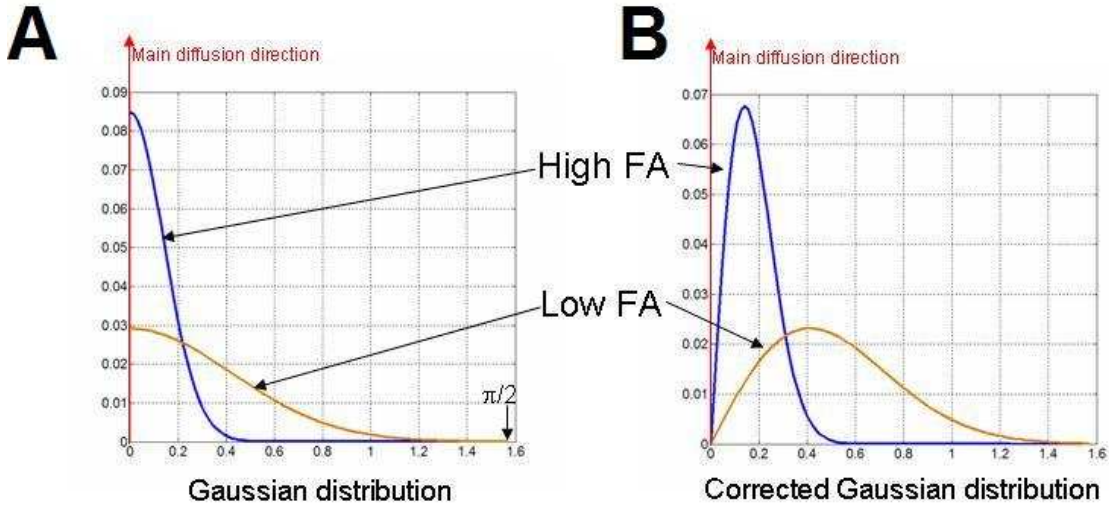


Figure 4.12. Probability distribution function of finding a diffusion direction with a certain deviation from estimated main diffusion direction using DTI. A) Gaussian function for high FA and low FAs values. B) Gaussian distributions, which were corrected (adjusted) to spherical coordinates.

approaches, so the explicit analytical forms are not required. A desired Gaussian distribution of the random directions was corrected by adding a part responsible for the spherical coordinate system (function H) is described in eq.3.12. Since the function H presented here is a positive and a non-zero, the cumulant have to be monotonic. This property assures that an unique inverse function exists.

Figure 4.13 shows the inverse cumulant function obtained from the corrected Gaussian distribution from figure 4.12b for high FA case. The distribution was normalized; therefore, the cumulant have the values from 0 to 1. It is then the domain of the inverse cumulant function.

The distribution generated using a standard random number generator is a constant function. To transform it into the desired corrected Gaussian distribution, each generated number has to be transformed through the inverse cumulant function. This operation was marked in figure 4.13 with red arrows.

If the numbers are generated from 0 to 1, then most of them would be transformed into small range of angles. In presented example in very less probable to generate angle deviation higher than 0.6. To do so, the generated random number would have to be very close to 1. In this way, the equally distributed random number will form the assumed distribution from figure 4.12b.

It was proposed in the methodology to introduce a functional W (eq. 3.15), called the border angle, for facilitate the control over the generated distributions. It is defined as the angle range about the main diffusion direction which includes 95% of generated random directions. In other words, it is cone angle outside which no more then 5% of directions is going to be generated.

Figure 4.14a shows again a corrected Gaussian distribution for high FA value. The 95% of function area is colored in red and the border angle is marked. The value of border angle can be easily found, since the inverse cumulant is known. The functional value is equal to the inverse cumulant value for $x=0.95$.

The final result of this subsection is shown in figure 4.14b. The proposed sigmoid function that varies the border angle in relation to FA. It cannot be fixed, because the observed FA depends on the used acquisition parameters and sequence used, the data pre-

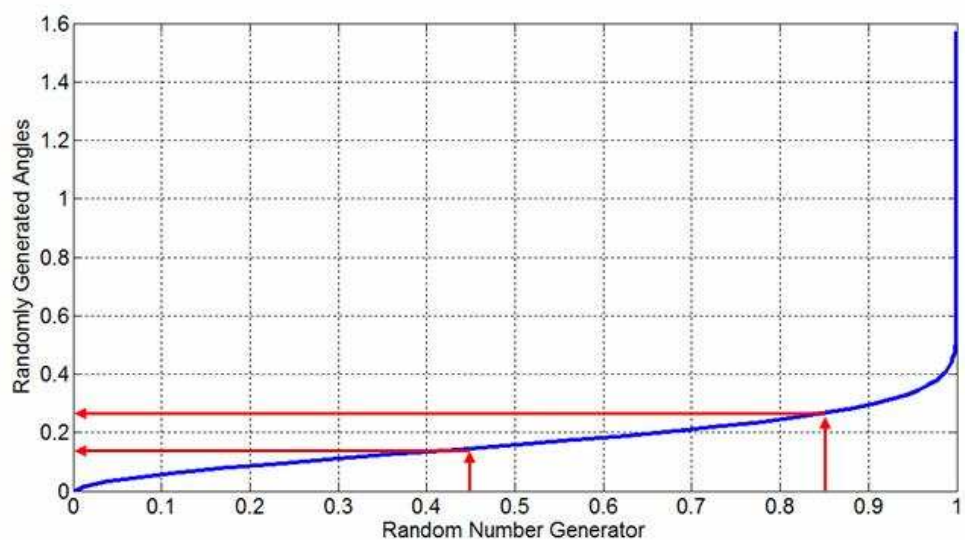


Figure 4.13. An example of inverse cumulant. This function transforms randomly generated numbers from 0 – 1 range into assumed distribution of randomly generated angles.

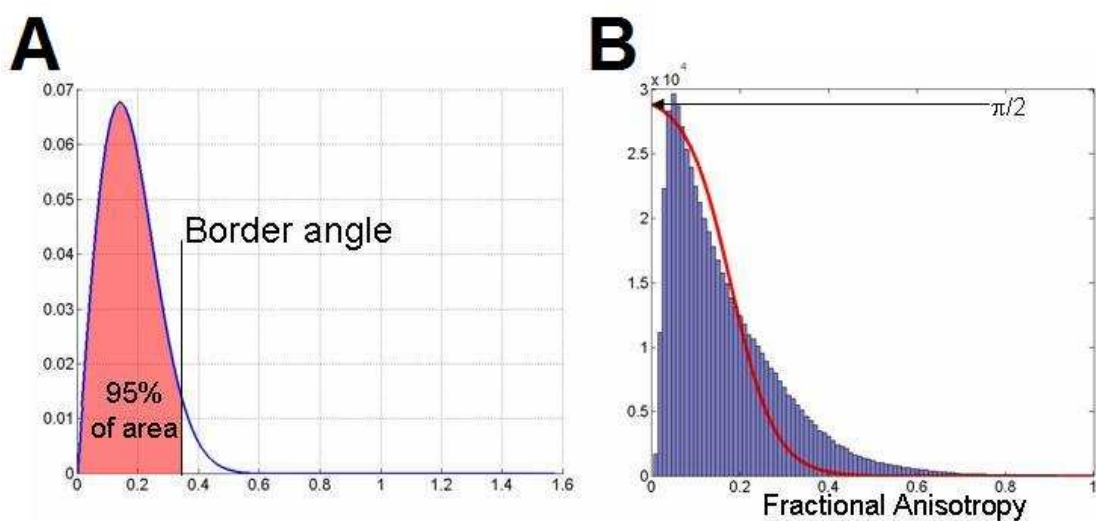


Figure 4.14. Border angle helps to control the spread of randomly generated angles about the main diffusion direction. BA is defined as angle at which the area under the distribution is equal to 95 %. B) The assumed sigmoid dependence between the border angle and the fractional anisotropy.

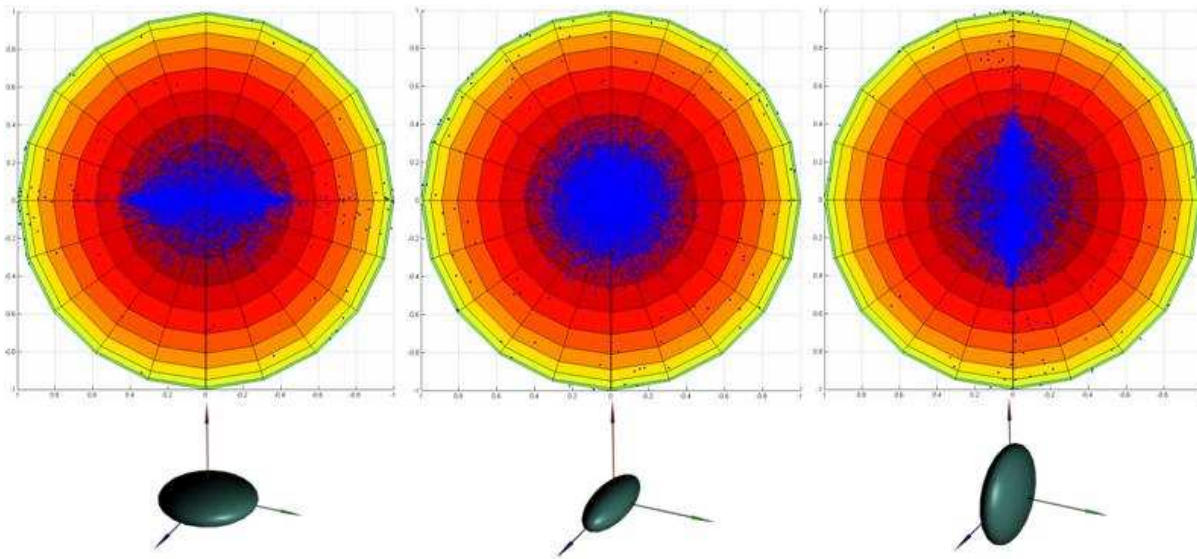


Figure 4.15. Examples of random distributions of diffusion direction in dependence of ratio between the eigenvalues. This model varies the extend of direction scattering, depending on ratio between second and third eigenvalues.

processing and inter-subject variability. Therefore, for each subject this function has to be adjusted. The FA value found in *corpus callosum* can be used as an internal reference point. Voxels which have at least 50% of FA value found in *corpus callosum* should be considered as voxels with single fiber population. Therefore, the direction estimated there can be trusted and there is no need to generate directions with large border angle. The scope of interest should be in range between the FA threshold level of fiber tracking algorithm and 50% of FA value found in *corpus callosum*. The slope of the sigmoid function should be adjusted in order to go smoothly from close to zero up to $\frac{\pi}{4}$. There is no need to generate completely random distributions (as the function approaches value of $\frac{\pi}{2}$). The values of the border angle are irrelevant below the FA threshold of the tracking algorithm, because the algorithm will never go through those voxels.

The last, but not least important, modification of the random direction generator is to take into the account the whole shape of the tensor. In practice, the second and third eigenvalue have to be investigated. If those values are similar, then the diffusion is equally restricted in others diffusion directions than the main one. When there is a disproportion between the second and the third eigenvalue, it means that the diffusion is more restricted in the direction correlated with the smallest one. It may happen, for example if fibers are crossing. In this case, the direction of the smallest eigenvalue has to be restricted.

Figure 4.15 shows the collections of random directions generated for the same FA value with different relations between the second and third eigenvalues. Under each distribution there is a visualization of tensor's ellipsoid. The restrictions in directions generation reflect the shapes of ellipsoids.

4.6.2 Digital phantom

During the preparation of probabilistic fiber tracking algorithm, it was tested using digital phantoms in similar way like in case of deterministic fiber tracking.

The probabilistic approach results in a connectivity matrix instead of strict trajectories, like it was in case of deterministic fiber tracking. Tracking algorithm was started from the centre of a digital phantom, build of parallel fibers. The influence of FA changes

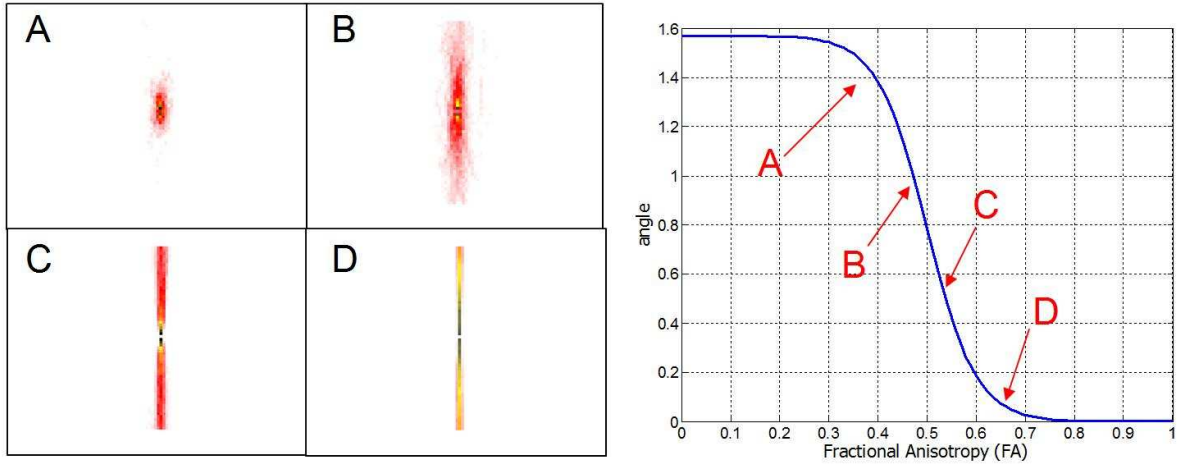


Figure 4.16. Connectivity matrix calculated with digital phantom. All diffusion directions were parallel. The position on BA function was changed in A – D.

is shown in figure 4.16. The subfigures A – D shows cross-sections through the connectivity matrix in plane that contain the seed point. As it is shown on the plot, the image A was derived with assumption of low FA value. In this position on the sigmoid function, all generated directions are random, because the border angle is close to $\frac{\pi}{2}$. The plot A shows only round spot in the centre of the image. The most of the tracts were quickly terminated because of the angle between the two successive steps was too wide.

In image B of figure 4.16 the border angle was slightly higher than $\frac{\pi}{2}$. The directionality of the phantom can be noticed. As the border angle is narrowed, the resulting image of connectivity is sharpening. In image D of figure 4.16d almost no variability of main diffusion direction was allowed. The reconstructed connectivity matrix shows one coherent fiber connecting the opposite ends of the phantom.

The border angle (see eq. 3.15) should be significantly lower than angle threshold used in tracking program, otherwise valid fiber trajectories will be lost, producing a false-negative result.

The ability of using second and third eigenvalues in fiber tracking was also tested in a digital phantom. For this purpose the centre of the phantom was filled with a region of disc tensors. Those tensors were having similar first and second eigenvalue, as shown in figure 4.17a. The expected result was the broadening of the reconstructed fiber bundle only in plane of the discs.

The connectivity matrix was not calculated in this case. For visualization purposes, all trajectories were shown. Figure 4.17b show no significant fiber bundle distortion in the centre of the phantom. When the same fibers are presented in plane of the disc tensors, a widening of the bundle can be easily noticed in the centre of the phantom.

This confirms the assumed behaviour of the tracking algorithm.

4.6.3 Thalamus segmentation

A human thalamus is a very complex structure. It is a mixture of white and gray matter located deep in the brain under the corpus calosum. Figure 4.18A shows the T_1 -weighted images of the thalamus structure. In MR imaging, the thalamus is a homogeneous structure with a strong insertion of fibers connecting motor cortex with the spine. Although, the thalamus is build of several nuclei, but their small size makes it impossible to contrast differences in T_1 and T_2 dependent images.

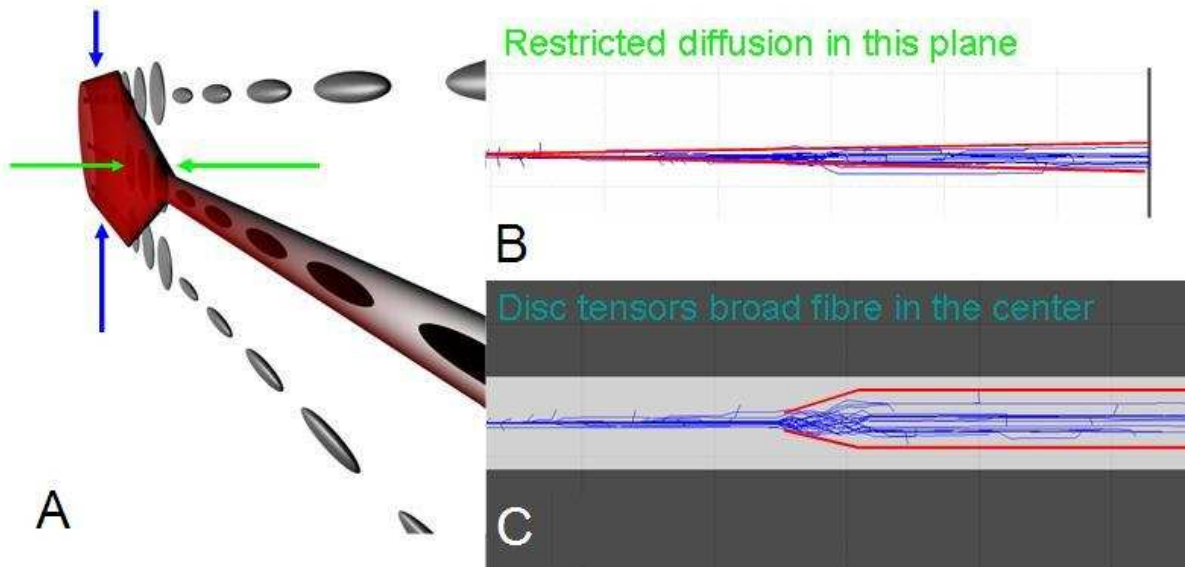


Figure 4.17. The second and third eigenvalues influence on probabilistic fiber tracking algorithm. A) A visualization of a region with only one restricted diffusion direction (disc-shaped tensors), B) Fibers representation of PFT in plane of restricted diffusion, no disc-shaped tensors influence is visible, C) the same representation in disc plane, fiber bundle widening is visible in center region, where disc-shaped tensors are located.

The uniform structure of the thalamus, also in FA images, can be segmented by classifying voxels according to the probability of connection to the upper cortex areas. In this experiment the upper cortex was divided into four regions. The red region marks the *prefrontal-temporal* area. The green colour encodes connectivity to the *motor area*. The *somato-sensory area* is presented in the blue colour. The last, *parieto-occipital* area in this image was shown in yellow colours. The scheme for the destination regions was presented in figure 4.18B.

The ability of the probabilistic fiber tracking algorithm to classify the regions in thalamus was verified. The result of this segmentation is shown in figure 4.18C. Each voxel of the thalamus was colored according to the highest connection probability to one of the defined regions of cortex. A selection of three slices was presented with corresponding region of FA map.

From each voxel of the thalamus originates 100 randomized fiber tracts. The end point was analyzed whether it is inside of one of the designated cortical areas. The winning region was the one with the maximal number of the fiber ends. The voxels on the border between the regions have a similar number of the ends for both the regions. The border is not smooth because there exist uncertainties in those voxels.

A density function of the connection probability was drawn in figure 4.18D. The arrow points to the starting point. The main (solid green) tract connects thalamus with the cortex. This is the most probable tract pathway. In the upper part the probability spreads into the cortical lobes.

The thalamus as complex brain structure, renders very homogeneous images in conventional T_1 and T_2 . The DTI combined with the information about the cortex functionality can reveal the underlying structure.

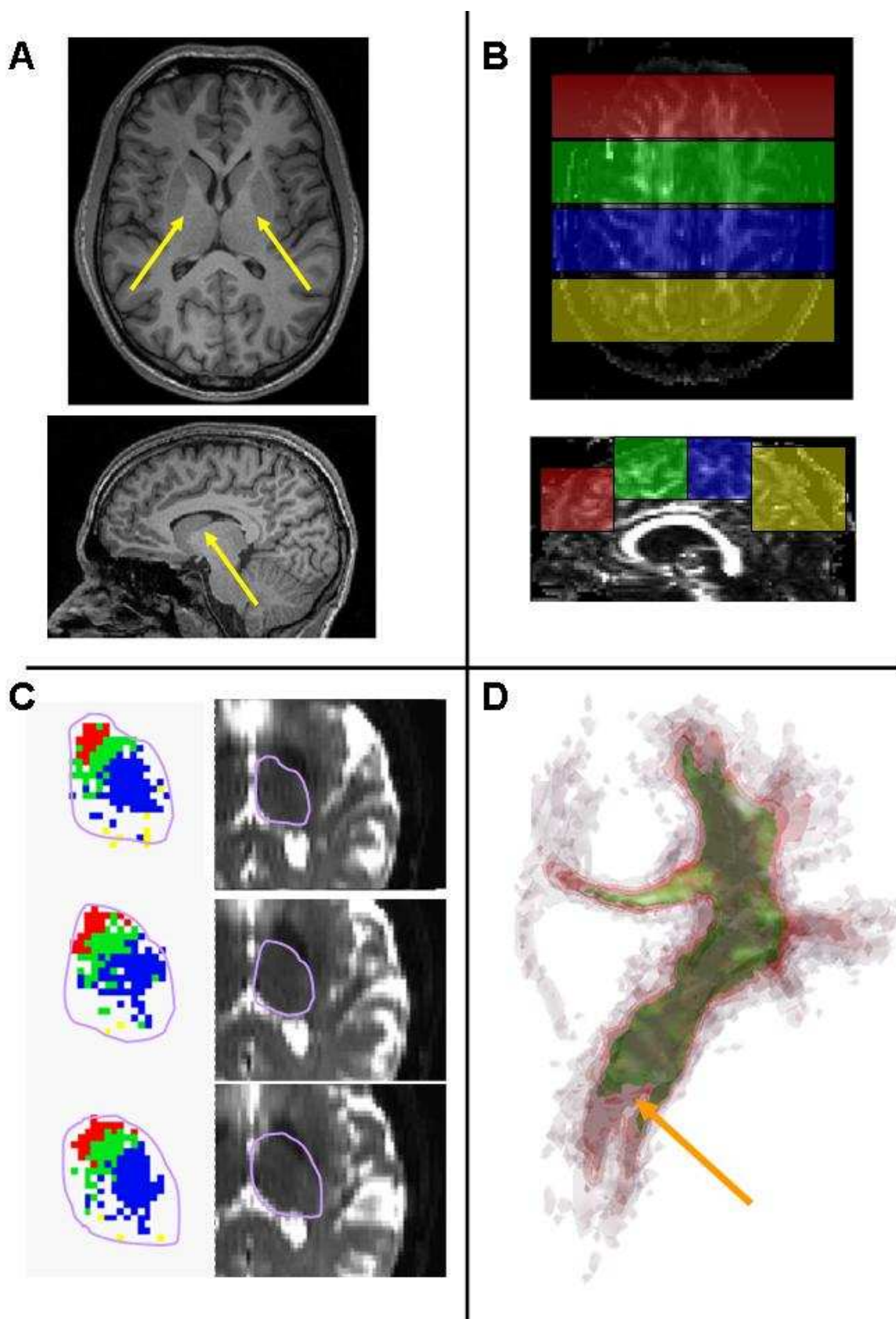


Figure 4.18. Thalamus segmentation result using probabilistic fiber tracking. Colors represents connectivity to different part of the cortex. A) T₁-weighted images B) Cortical regions of fiber destination C) Thalamus segmentation with corresponding T₂ image D) Visualisation of 3D density function of probability of connection between one of the thalamus voxels with the cortex.

4.7 Q-ball tracking

The last experiment concludes all efforts presented in this work to implement, verify and apply a multi-directional diffusion weighted imaging in clinical conditions. The results presented here directly answer the main question of the thesis, that it is possible to perform a HARDI experiment in suitable time for a clinical investigation.

Two main advantages over the DTI are shown in the following subsections. The first advantage is the presence of multiple diffusion directions in a single voxel and the ability to use it for fiber tracking. The second advantage is the ability to reconstruct long fibers that go through crossing regions; in this case it is difficult to reconstruct it correctly by the DTI.

The comparison of reconstructed data with both DTI and q-ball is shown in figure 4.19 A and B. The arrow shows the crossing region of the corona radiata. In the case of DTI (fig.4.19A) the region consist only of poorly defined spherical-shaped tensors. It is difficult to recognize the structure on the white matter. The tensor data are similar to q-ball in diffusion directions only in case single fiber population. In this case both methods give same results. DTI is not able to resolve crossing. Presented tensors have low FA and it is difficult to see main diffusion direction. In opposition, the q-ball reconstruction reveals the structure clearly (fig.4.19B). The crossing voxels are visible and it is easy to identify both connections from the corpus callosum and from motor fibers.

4.7.1 Crossing regions

The fiber tracking algorithm has to handle all significant diffusion directions found in a given voxel. Figure 4.19 show an example situation where a crossing voxel was chosen as a seed point for deterministic tracking. Subfigures C and D show tracking results with different levels of seed point subdivisions.

In figure 4.19C the subdivision level was 2, it means that 8 projections were calculated with slightly different starting positions inside the chosen voxel. Figure 4.19D shows the reconstruction for subdivision level of 4 (64 projections). All four branches could be reconstructed.

The ability to handle the crossing regions was examined in the regions near the *corpus callosum*. Figures 4.19E and F show two large fiber bundles known to cross. Blue colour represents projections of fibers that connect the motor cortex with the spine. Seed point subdivision revealed branching of the tract to different parts of the cortex. The red fiber bundle represents the connection between both hemispheres of the brain through the *corpus callosum*. Figure 4.19E shows the reconstruction in coronal plane and 4.19F shows the fibers from above for better exposition of the crossing region.

4.7.2 Tracking results

The acquired data set has an isotropic resolution 2mm, which is typical for DTI experiments. Data collection was shorter than one hour for three averages at b-value of $1500 \frac{s^2}{mm}$

In previous subsections it was shown that the HARDI method provides better quality of data. The last subfigures of 4.19 show the reconstruction of the optic tract. Two fiber bundles that connect primary visual cortex with lateral geniculate nucleus and with anterior part of the brain to chaisma and eyes.

Figure 4.19G shows reconstructed fiber bundles in transversal plane, 4.19H shows sagittal projections. The last figure 4.19I shows the reconstruction with a colormap as

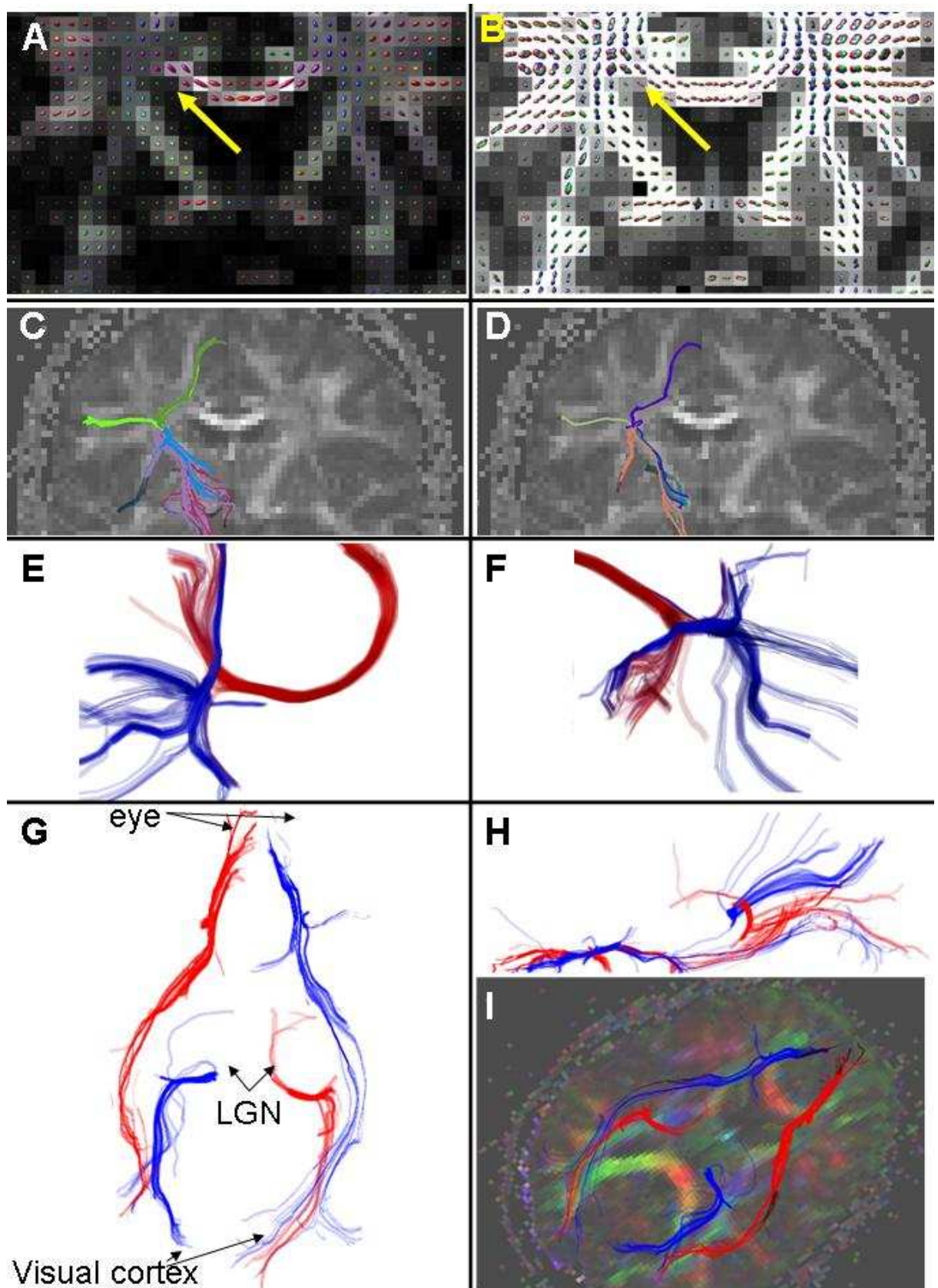


Figure 4.19. Results of whole-brain q-ball data acquisition and fiber tracking. A) Dataset reconstructed with DTI - visualization of the tensors, B) Dataset reconstructed with q-ball - visualization of the q-shapes C) Fiber reconstruction from a crossing voxel - Four fibers per voxel D) 64 projection from single, crossing voxel with slightly different starting positions, E,F) Direct fiber crossing in corona radiata, G,H,I) Optic tract reconstruction with means of q-ball imaging.

reference point for localisation. The underlying image was chosen from the level that LGN is located.

Full reconstruction of the optic tract was possible only by q-ball method. The starting points were selected manually and located close the eyes in the case of long tracts. The second part was reconstructed by selecting the LGN nucleus in the thalamus. The tracking was performed using 64 seed points per starting voxel. The important message is that no fibers were deleted to clear the images. It is shown that the reconstruction is stable even for long fibers that go through a crossing areas. Also curvature is not a problem in this case, because the Meyer's loop was correctly reconstructed in connection. However, this part can be also reconstructed by means of DTI, as it was shown in earlier subsections.

Chapter 5

Discussion

A microscopic tissue properties influence the MR measurement. In many cases, the image produced by an imaging system is just an approximation, an average over all matter properties that were found in the voxel. The image resolution offered by the state-of-the-art hardware is too coarse to measure an homogeneous material.

A researcher is forced to work with a not perfect measurement conditions. The measurements of the diffusion attenuation exploit the microstructural influence on the MR signal formation in order to reconstruct information laying a couple orders of magnitude below the resolution of the equipment used.

The material, here presented, focuses on the brain. This is the main stream of the diffusion methods. The white matter offers the highest degree of the anisotropy in the human body. It is worth to mention that several groups are developing diffusion measurements in other parts of the body. The liver is extensively explored [35], [36] and [37] as well as prostate in an oncology aspects [38] and [39]. However, those applications use rather simple data processing in comparison to the diffusion measurements of the brain, since mainly an apparent diffusion coefficient is used. Measurements of the fiber directionality and the fractional anisotropy is used in muscle examination [40].

The directional structure of the brain in the most complex; therefore, it requires the most advanced processing and reconstruction algorithms.

5.1 Implementation

As a part of this thesis a software that covers all the steps of the data gathering, the processing, the reconstruction and the visualization was developed. In this way, it is possible to modify freely any step of the data processing. A double-refocusing sequence with an EPI readout was used for the data acquisition. This sequence strategy can be found as recommended in the literature [41], [42]). The same authors pointed that a steady-state free precession strategy can be used as an alternative to the EPI readout, they suggest a PROPELLER trajectory. Recently introduced a key-hole [43] technique was suggested for the acquisition speed up and the higher resolution. However, it is still questionable, if the k-space combined from two parts acquired with a long time gap can give reliable results.

5.1.1 Data processing

The data processing in this thesis was performed as described firstly by Basser et al [5]. Some details were taken also from following reviews: [7, 44, 45]. The Moore-Penrose pseudo-inversion matrix was obtained using least-square fit, which is the most common approach. Due to noise in the data, some of the eigenvalues can be negative. Therefore the fractional anisotropy can have value over 1. However, it is impossible to have this situation in area of the brain. It is more likely to have unnatural high FA (noise effect) at the border of brain. Those values have to be set to either 0 or 1. However, tracking procedure do not enter those areas, because it is gray matter and surrounding FA values are below the threshold of tracking algorithm.

The tensor describes well situation where a single fiber population is present. There is an easy way to find the dominant direction of diffusion. It was shown that it is possible to predict multiple diffusion directions using a combination of tensors or tensors with a higher order than 2 [46].

The q-space methods presented here are mainly organized around the q-ball approach presented and implemented according to [6]. This methods allow directly (without any model) to extract the diffusion directions from properly designed experiment. There were presented numerous methods for the measurement speed up like for example [16] PAS-MRI. All those methods assume some of the properties and on that basis the required data amount can be reduced.

One of those methods, which is very popular is spherical harmonics decomposition [47][48] and the constrained version [18][49]. In this approach, it is assumed that all measurements can be described as a linear combination of the response function. It is still in question, how a response function should be obtained. The easiest way, it is to simulate it, but it is also possible to measure it directly from a region of the brain in which it is known that there is only a single fiber population. Usually this region is the *corpus callosum*.

5.1.2 Fiber tracking

A streamline version of the fiber tracking was implemented according to Mori [50]. An additional modification was made to enable the algorithm to recognize more than one diffusion direction per voxel. Also step size was reduced for better accuracy and a sub-voxel division of the starting points are competitive solutions, partially described in [50] and [23].

It was also proposed to remember the previous direction of diffusion and alter the current one in tracking algorithm [23].

The probabilistic version of the tracking algorithm is relying on the streamline version. The random direction generator was implemented as described in methods part. In subsection 4.6.1, the adjustments of tracking algorithm was discussed. More information about uncertainty and error propagation can be found in [24].

In the thalamus segmentation experiment the connectivity matrix was calculated and normalized according to a probability index of connectivity [51]. Also it was tested with digital phantoms that proposed mathematical framework and implementation that follows the assumptions of probabilistic tracking. The algorithm changes its behaviour regarding the FA in the voxel changing generated angle distribution, as it was shown in figure 4.16. Moreover, the usage of all three eigenvalues instead only dominant diffusion direction enable the algorithm to properly deal with 'disc' tensors. Figure 4.17 shows how generated fiber realizations spread only in the plane of a disc tensor. In a perpendicular plane fibers

are coherent, because such a tensor gives an information that in the perpendicular plane is restricted.

5.2 Validation

Testing revealed that the implemented procedures deal correctly with all the primary tasks. Reconstructed fibers follow directly the assumed direction in the digital phantoms (4.1a and b). The test showed that no fiber were lost and that the tracking software developed here can be used for applying in the brain. However, the nerve bundles usually are bent, so it was shown that the tracking algorithm can resolve a wide range of the nerve curvature in the fig. 4.1c. Due to the step size, which is not infinitely small, the tracking algorithms on curves can deviate from an primary track. The algorithm implemented here is recovering up to 50 % fibers in a full angle turn. However, since the fibers in the brain rarely turn back (Meyer's loop) and never make full turn, this deviation is an acceptable error.

Developed algorithm is the same for the DTI and the HARDI methods. Therefore, it was shown that it can successfully handle crossing fibers. The synthetic data proved that even a crossing of three fibers can be resolved in this way (figure 4.1d). The fiber tracking optimization was performed. The best results were obtained with a step size Δx equal to half of the voxel size. Also sub-division of the starting points enhanced the quality of the results, especially in the optic radiation reconstruction, where the starting regions were small and submerged in the gray matter.

The development of bio-phantoms was successful, the material and the preparation routines allow for a simulation of a high anisotropy. The performance of the bio-materials was found better in this application. None of the synthetic materials were not capable of building high enough FA, in comparison to brain values (see table 4.1). The directions of the structures could be extracted as shown in figure 4.2, but the low FA disqualify that materials. However, some groups were able to use synthetic fibers to simulate a high FA, like presented in [52].

The best results were obtained with pig's spinal cord and in following discussion all artificial phantoms were build out of this material.

After gaining a confidence in the implemented procedures, it was possible to perform the *in-vivo* experiments and to compare *in vivo* the results of most commonly used methods i.e. DTI, q-ball, and SD.

5.2.1 Artificial phantoms

The tensor model for a single fiber populations works very well. The error estimation and its propagation in a relation to the acquisition factors such as sampling directions, the b-value or the SNR was shown in [12] In the case of multiple fiber population the tensor model showed a decrease of fractional anisotropy and two eigenvalues of similar amplitude. In this way only a plane of crossing was determined, but it was impossible to retrieve information about the directions of the crossing fibers. The tensor approach successfully used in clinical routine was not fulfilling all of the assumptions of the theoretical model. For instance, the duration of the gradient pulses should be significantly shorter than gap in-between them. Default MR sequences provided by manufactures, however, build-up strong diffusion weighting by filling all possible time elements between excitation and data acquisition with the diffusion gradient of the maximal strength in order to have the shortest possible time of echo. Diffusion directions provided by tensor model were

nevertheless successfully applied, despite the fact that voxels with crossing fibers could not be analysed properly. In a similar way as in the tensor approach, the q-ball algorithm has assumptions, which cannot be completely fulfilled. Clinical routine always have to consider a trade between quality of measurement and what a patient can stand during the measurement.

It was shown here, that even not being strict with the assumptions of the q-ball measurement theory the DTI gives coherent results. When acquiring patients, which are not the healthy volunteers, it is important to reduce the time of the acquisition as much as it is possible. In many cases, the condition of the patient makes even a half an hour measurement difficult for them, not only in the aspects of remaining motionless. It was shown in the results that data from measurements with a decreased b-value, which have a major impact on the acquisition time, still provides data that can be used to resolve fiber crossing problem.

In analysis of reconstruction stability, the half of the diffusion directions fell into 5 degree wide cone for a single fiber bundle case. The fiber crossing area were successfully resolved. Two pairs of maxima were present in all voxels.

The use of low b-values and smoothing operations during the postprocessing introduces a smoothed and blurred ODF-function, which renders an increase of the uncertainty of diffusion direction estimation.

It could be shown here that an increase of the interpolation kernel degrades the result quality. This effect can be present in other steps of the postprocessing as motion correction. Data re-gridding interpolates measured signal and provide an additional smoothing effect.

Perrin et al. show for b-value of 1000 s²/mm that angular error is better than 30 deg [52]. Also experiments made with a high b-values (up to 4.4 *10⁴ s²/mm) show that the HARDI methods are able to differentiate crossing fibers angles as small as 30 deg [53]. The uncertainty provided by the reconstruction methods provide smaller angle deviations.

To conclude, even if the assumptions of a high b-value are not met in the clinical routine q-ball measurement, this method can successfully retrieve proper directions of the diffusion in a single as well as in a multi fiber population case. The stability of this evaluation is in range of degrees. Therefore, the fiber tracking algorithms can have good quality data, which was measured for lower b-values ranges.

5.2.2 SD, q-ball and DTI comparison

The investigation of the diffusion directions used here does not show the uncertainty of the measurements; this can be estimated, for example, by a Monte-Carlo experiment [54]. Nevertheless, a comparison of diffusion directions derived in successive measurements shows that in a repeated measurements of the white matter structures, the reconstructed directions do not change by more than 10 degrees.

This justifies the conclusion that the results were neither obtained due to noise nor influenced by any other measurement factors. Tensor model, q-ball, and SD, give the reproducibility of the reconstructed diffusion directions at the similar levels.

The ODF_q from the q-ball describes the angular distribution of the diffusion function, whereas the ODF_{SD} from the SD evaluation only represents the directionality of the fiber populations contained inside a voxel. The aim in this work was also to evaluate the reliability and the reproducibility of dominant diffusion directions from both ODFs and to evaluate their suitability for the fiber tracking. Both ODFs should show the similar dominant diffusion directions in the same voxel and are in this aspect comparable. The similarity of the reconstructed dominant diffusion directions could be shown, especially

for the higher FA values (figure 4.7). Their different behaviour regarding the noise and the b-values is only of interest in this investigation if it affects the orientation of the reconstructed dominant diffusion directions.

The stability comparison (see figure 4.7b) shows that the inconsistencies between the tensor model, the q-ball, and the SD are present only for FA values from 0 to 0.2. The voxels with such low FA values are found, for example, in the regions of the fiber crossing inside the white matter. Those voxels are strongly influenced by the noise. The noise fluctuations are a significant part of the signal changes in different diffusion directions because the diffusion is isotropic or almost isotropic in the voxels with low FA. When comparing the delta function in this FA range, one can observe that the tensor model produces the most coherent results in the successive measurements. The noise influence is the most evident in the case of the SD. Tournier et al. did show that the directions reconstructed in the ODF_{SD} are more pronounced depending on the b-value used in the data acquisition [18]. The quality should increase for larger b-values than the 1500 s^2/mm used here because the reconstructed directions will be less noise sensitive. This is in accordance with the results presented in the figure 4.10b.

In the case of a single fiber population inside a voxel, all reconstruction methods may result in the same direction of diffusion. However, in the case of multiple fiber populations (lower FA), the ODFs of q-ball and SD show two or more dominant directions of diffusion and the tensor model indicates the average of these directions as principal direction of diffusion. For low FA values, the tensor model shows the most stable behaviour, but in regions with multiple fiber orientations the reconstructed principal diffusion direction is not accurate.

Figure 4.8 shows the reproducibility of the second direction in the q-ball reconstruction and the SD. It was surprising that there were many points with relatively high FA (≥ 0.15) with high angle above 0.78 radians (45 deg) as shown exemplary in the figure 4.8a for the q-ball. This can be explained (partially) by the noise, since the noise-induced signal variations might lead to a change in the ordering of the reconstructed diffusion directions. In the case of voxels with two approximately equal fiber populations the noise can determine which of the reconstructed directions the main one is.

The second direction of the diffusion is not present in the voxels with the FA above 0.4. Therefore, the axis in the figure 4.8a is restricted to this value. This corresponds to the observation that voxels with only one dominant direction of the diffusion have a higher degree of the anisotropy and therefore, higher FA values. Consistency of the second direction of diffusion increases with the FA-value in the comparison of the q-ball reconstruction and the SD, as shown in figure 4.8b. When the consistency of the main diffusion direction (figure 4.7a) is compared with the consistency of the second diffusion direction (figure 4.8b), the observed delta values for the FA equal to 0.1 are similar. The decrease of the delta in the case of the second diffusion direction is smaller than for the main diffusion direction, because the evaluation of the second diffusion direction may be more vulnerable to the noise.

When fitting the diffusion ellipsoid to the data, the tensor model does not use the surplus of information [12].

As shown in the figure 4.9a, the ODF_q shapes degrade as the smoothing factor increases. One can observe that two, easily distinguishable diffusion directions disappear as σ goes from 0.009 to 1. Those two peaks in ODF_q with σ of 0.009 are replaced in ODFs with higher σ by one peak pointing towards the average of the previously reconstructed diffusion directions.

Two angle distributions were compared in figures 4.9b and 4.9c. Figure 4.9b compares the diffusion directions calculated by the tensor model with the q-ball reconstruction

with standard kernel ($\sigma = 0.009$) and in Figure 4.9b q-ball ODFs were reconstructed with high smoothing ($\sigma = 1$). The directions reconstructed from the highly smoothed ODF_q show very good agreement with the directions derived from the second order tensor. The deviation is below an angle 0.2 rad for most of the evaluated voxels. This supports the conclusion, that strong smoothing of the q-ball reconstruction gives exactly the same results as applying the second order tensor.

No b-value dependence of the distribution was observed for q-ball in figure 4.10a. The stability in finding the main direction of diffusion is similar, so one can still quite accurately determine the main direction of diffusion at low b-values. The influence of the b-value is more visible in blurring the shape of ODF_q at low b-values [18]. Sharpening of the ODF will in general reduce the variability of the reconstructed fiber orientations. For the range of b-factors evaluated in the study presented here no influence of the sharpening of the ODF on the reconstructed orientations was observable, because the orientations were already reconstructed reasonably well for the lowest evaluated b-factor.

For SD, the reconstruction quality improves with an increase in b-factor as shown in figure 4.10b. Tournier et al. pointed out that this improvement is only observable as long as the signal dominates the noise level [55]. The b-factor, therefore, cannot be indefinitely increased. Here, the results of an evaluation of this b-factor dependence for SD are shown in in-vivo data. This new evaluation complements the observations on phantom data presented in [55].

The reconstruction of neuronal connections with fiber tracking algorithms can only improve by using ODF fields instead of tensors. The reproducibility of the q-ball and SD reconstruction is at the same level as tensor model, but ODFs provide much more information about the nature of white matter structures.

In this paper, the algorithm proposed in the first paper on q-ball evaluation by Tuch [6] was used, as well as later introduced SD for calculation of the ODF. Recently, several groups [49][48][56] did show, that HARDI experiments can be performed much faster than evaluations of the whole q-space. Therefore, it should be possible, to introduce this advanced evaluation technique in routine multidirectional diffusion weighted imaging.

Concluding, the HARDI evaluation methods q-ball and SD provide a stable diffusion direction estimation that can be used for fiber tracking for voxel with FA-values larger than 0.2. Both q-ball and SD have their individual advantages and disadvantages. For the range of b-factors evaluated here the orientations reconstructed from ODF_q are more stable in regions with low FA than the ones reconstructed from ODF_{SD} . We, therefore, recommend the use of q-ball for the evaluation of in vivo diffusion measurements that were acquired with a b-factor from the range evaluated in this experiment.

5.3 Clinical applications

fMRI and DTI in optic tract reconstruction

Combination of the functional information from the gray matter using the fMRI with the anatomic information of the white matter is very important for understanding how the brain works. The fMRI can provide an adequate information about the response of the cortex to the stimuli. Those stimuli are usually combined into experiments showing spatially how the gray matter is processing the information. However, the information has to be provided to the neurons as well as it has to be lead out for further processing or for making action. The medium for data transmission are axons. The MRI do not provide a method for direct measurement data transmission in nerves. It is possible only by sticking an electrode into the nerve cell. It is very inconvenient method due to ethical

reasons and huge numbers of nerves in the brain. The electromiography is only applied for single peripheral nerves. The diffusion measurements with the an MRI provide only anatomic information of fiber's pathways. It is assumed that in such a highly organized structure as human brain, it should not be any unnecessary connections. Therefore, it is assumed that existing connections are functional.

In this experiment two centers of visual information processing were found. The DTI reconstructed Meyer's loop correctly. It was known from the anatomy that this connections existed. However, in this experiment regions of the CGL, the V1, and the loop were determined fully *in-vivo*.

Algorithms presented in this thesis were able to correctly acquire the data and reconstruct the part of the optic radiation using a standard DTI data. This information can be very useful in preparation for surgical procedures, when a patient-based information about the location of important structures has to be known.

Sherbondy et al. reconstructed optic radiation using a similar approach[57]. However, in that article the regions of interest were selected manually, basing on the anatomic reference. It can be obtained in healthy brain. However, in the case of patient's study, the brain can be deformed by the disease or tumor. In that case, only a direct measurement can provide an exact location of the lateral geniculate nucleus and the visual cortex.

Thalamus segmentation with PFTR

Probabilistic or stochastic fiber tracking is a method of dealing with the complex architecture of the brain. Each voxel, each measurement is a sum of thousands nerve bundles. An average is measured, but each of those fibers may end in different part of the brain. It is possible to evaluate the probability of connection between two or more regions on white matter by using PFTR.

Dyrby et al. shown the validity, the consistency and the reliability of the probabilistic tractography using a histological tracers as a reference [58]. Three pigs were examined by an in-vivo injection aimed for the right somatosensory cortex, the right prefrontal cortex and the left motor cortex. The brains were measured in-vivo and in-vitro. In vivo DTI data was analyzed using the probabilistic index of connectivity[51]. The fiber tracking was performed with approach proposed by Mori et al [59].

Problems with the tractography in the regions of the thalamus were found in the study of Dyrby et al. [58]. It was explained as a problem of only single diffusion direction of DTI, because the thalamus is known for its complex structure. Therefore, voxels can contain multiple fiber populations. False-positive tracts were found in relation to the histological marker, again Dyrby refer to DTI limitations and suggest that q-ball can improve reconstruction.

The probabilistic fiber tracking reproducibility was also validated in a group study over the healthy volunteers by Behrens et al.[60] and Heiervang et al.[61]. Lazar and Alexander have shown earlier in simulation that the probabilistic fiber tracking can be a reliable method using a synthetic diffusion tensor field[62].

The results presented in this thesis are consistent with results of Behrens et al[63]. In this thesis a lower number of fiber realization was used to obtain coherent result. However, Behrens et al. show segmentation of thalamus into seven segments.

Using the proposed probabilistic fiber tracking algorithm, it is possible to segment the thalamus. The probabilistic approach has a great value in understanding of the structural organization of the human brain. By exploring different classes of connection probabilities, it is possible to distinguish between parts of homogeneous structures in imaging, like for example in the thalamus.

Whole brain q-ball imaging

Finally, it was shown that it is possible to obtain a good quality dataset of the whole brain volume in a clinical reasonable time.

The difference shown in the figure 4.19A and B is crucial. In the case of q-ball imaging, the crossing is clearly resolved. Voxels in *corona radiata* have two peaks - two main directions of diffusion. The regions of fiber crossing mentioned here are causing severe problems for the fiber tracking with the conventional DTI techniques. For multiple fiber population voxels the DTI results in tensors that have two almost equal eigenvalues. The noise determines which of them is dominant if two fiber populations are the same. In the case of not equal ratio between fiber population, only the diffusion direction of the dominant part is visible in the DTI evaluation, while the second direction is not detectable. The added value of the q-ball method is that direct measurement of diffusion is free from the model's assumptions. Therefore, it can resolve multiple peaks in diffusion function. Better diffusion data leads to more accurate tracing and better understanding of human brain connectivity.

Presented q-ball method show better performance not only in the theory and phantoms, but also in the in-vivo experiments. The long optic radiation was successfully reconstructed as presented in figure 4.19. Those fibers go through whole brain volume from the anterior to the posterior passing multiple crossing regions on the way.

Concluding, the high angular resolution diffusion imaging is the next step after the diffusion tensor imaging. New applications for deterministic and probabilistic fiber tracking use multi-directional diffusion [64]. High angular resolution diffusion imaging can be expected to become a new measurement in clinical examination, if new processing techniques for improving data quality and reducing time of acquisition will be available [65].

Acknowledgements

I wish to thank Prof. Uwe Klose for his patience, knowledge and support. Over few last years, he was encouraging me to finish my PhD thesis, even when I have lost all the hope. He also invited me for a early stage training program, where I could learn and work the subjects of the thesis.

I wish to thank also all my teachers and university profesors for the knowledge and passion to sicence, they have inculcated in me.

My thanks go out to Prof. Wolfgang Grodd and Dr. Michael Erb for their help in any medical and technical related question I had.

I wish to thank my family, all friends in Poland and all over the world for believing in me and for showing me a support.

I wish to thank prof. Jarzab for keeping my job in Polnad for two years, even though the thesis was not in the field of nuclear medicine.

Many of the results presented here were obtained with a cooperation with other faculty members and the students. I would like also to thank Filip Jiru and Ralf Saur for many hours, days and weeks of working together on common projects and goals. My thanks go also to Vinod Kumar, who is the most optimistic person I have ever known. I would like to thank David Ratteri, Agnieszka Jablonka and Aleksandra Klimas, the students who were measuring and writing matlab code with me. They have shown me a real determination and they gave me motivation for new experiments.

I would like to thank Prof. Gembris for providing data for the spiral testing phantom and Dr J.D. Tournier for providing the matlab code for spherical harmonic deconvolution.

I wish to thank also all people engaged in the EU program "Maria Curie Action - Early Stage Training Program" for financing my research in Tübingen.

Bibliography

- [1] Tanner JE. Self diffusion of water in frog muscle. *Biophys J.*, 28:107 – 116, 1979.
- [2] Scolan DF. Holmes A. Winslow R. and Forder J. Histological validation of myocardial microstructure obtained from diffusion tensor magnetic resonance imaging. *Am. J. Physiol.*, 275:H2308 – 2318, 1998.
- [3] Moseley ME. Cohen Y. Kucharczyk J. Mintorovitch J. et al. Diffusion-weighted mr imaging of anisotropic water diffusion in cat central nervous system. *Radiology*, 176:439 – 445, 1990.
- [4] Moseley ME. Cohen Y. Kucharczyk J. Mintorovitch J. et al. Diffusion-weighted mr imaging of acute stroke: correlation with t2-weighted and magnetic susceptibility-enhanced mr imaging in cats. *Am. J. Neuroradiol*, 11:423 – 429, 1990.
- [5] Basser PJ Mattiello J and LeBihan D. Estimation of the effective self-diffusion tensor from the nmr spin echo. *J Magn Reson*, 103(1):247 – 254, 1994.
- [6] Tuch DS. Q-ball imaging. *Mag. Res. Med.*, 52(6):1358 – 1372, 2004.
- [7] Mori S. and Barker PB. Diffusion magnetic resonance imaging: Its principle and applications. *New Anat.*, 257:102 – 109, 1999.
- [8] Haacke EM. Brown RW. Thompson MR. and Venkatesan R. *Magnetic Resonance Imaging – Physical Principles and Sequence Design*. Wiley-Liss, 1999.
- [9] Mansfield P. Coxon R. Hykin J. Echo volume imaging of the brain at 3.0t: First normal volunteer and functional imaging. *J Comput Assist Tomogr*, 19:847 – 852, 1995.
- [10] Moore EH. On the reciprocal of the general algebraic matrix. *Bulletin of the American Mathematical Society*, 26, 1920.
- [11] Penrose R. A generalized inverse for matrices. *Proceedings of the Cambridge Philosophical Society*, 51:403 – 413, 1955.
- [12] Jones DK. The effect of gradient sampling schemes on measures derived from diffusion tensor mri: A monte-carlo study. *Magn Reson Med*, 51:807 – 814, 2004.
- [13] Callaghan PT. MacGowan D. Packer KJ. Zelaya FO. High resolution q-space imaging in porous structures. *J Magn Reson*, 90:177, 1990.
- [14] Xia Y. Callaghan PT. One-shot velocity microscopy: Nmr imaging of motion using a single phase-encoding step. *Magn Reson Med*, 23(1):138 – 158, 1992.
- [15] King MD. Houseman J. Roussel SA. van Bruggen N. Williams SR. Gadian DG. q-space imaging of the brain. *Magn Reson Med*, 32(6):707 – 713, 1994.

- [16] Parker G.J. and Alexander D.C. Probabilistic anatomical connectivity derived from the microscopic persistent angular structure of cerebral tissue. *Philos. Trans. R. Soc. Lond. B*, 360(1457):893 – 902, 2005.
- [17] Özarslan E. Shepherd TM. Vemuri BC. Blackband SJ. Mareci TH. Resolution of complex tissue microarchitecture using the diffusion orientation transform (dot). *Neuroimage*, 31(3):1086 – 1103, 2006.
- [18] Tournier J.D. Calamante F. Gadian D.G. and Connelly A. Direct estimation of the fiber orientation density function from diffusion-weighted mri data using spherical deconvolution. *NeuroImage*, 23:1176 – 1185, 2004.
- [19] Healy D.M. Hendriks H. and Kim P.T. Spherical deconvolution. *J. Multivar. Anal.*, 67:1 – 22, 1998.
- [20] Alexander D.C. Barker G.J. and Arridge S.R. Detection and modelling of non-gaussian apparent diffusion coefficient profiles in human brain data. *Magn. Reson. Med.*, 48:331 – 340, 2002.
- [21] Mori S. and van Zijl P.C.M. Fiber tracking: principles and strategies - a technical review. *NMR in Biomedicine*, 15:468 – 480, 2002.
- [22] Chou M.C. Wu M.L. Chen C.Y. Wang C.Y. Huang T.Y. Liu Y.J. Juan C.J. and Chung H.W. Tensor deflection (tend) tractography with adaptive subvoxel stepping. *J Magn Reson Imaging*, 24(2):451 – 458, 2006.
- [23] Cheng P. Magnotta VA. Wu D. Nopoulos P. Moser DJ. Paulsen J. Jorge R. Andreasen NC. Evaluation of the gtract diffusion tensor tractography algorithm: a validation and reliability study. *Neuroimage*, 31(3):1075 – 1085, 2006.
- [24] Behrens T.E.J. Woolrich M.W. Jenkinson M. Johansen-Berg H. Nunes R.G. Clare S. Matthews P.M. Brady J.M. and Smith S.M. Characterization and propagation of uncertainty in diffusion-weighted mr imaging. *Magn Reson Med*, 50:1077 – 1088, 2003.
- [25] Stejskal EO and Tanner JE. Spin diffusion measurements: spin echoes in the presence of time-dependent field gradient. *Journal of Chemical Physics*, 42(1):288 – 292, 1965.
- [26] Wider G. Döetsch V. and Wüthrich K. Self-compensating pulsed magnetic-field gradients for short recovery times. *J Magn Reson A*, 108:255 – 258, 1994.
- [27] Reese T.G. Heid O. Weisskoff R.M. and Wedeen V.J. Reduction of eddy-current-induced distortion in diffusion mri using a twice-refocused spin echo. *Mag. Res. Med.*, 49(1):177 – 182, 2003.
- [28] Bernstein MA. King KF. and Zhou XJ. *Handbook of MRI Pulse Sequences*. Elsevier, 2004.
- [29] Press WH. Flannery BP. Teukolsky SA. and Vetterling WT. *Numerical Recipes in C: The Art of Scientific Computing*. Cambridge University Press, 1992.
- [30] DeYoe EA. Carman G.J. Bandettini P. Glickman S. et al. Mapping striate and extrastriate visual areas in human cerebral cortex. *Proc Natl Acad Sci U S A.*, 93(6):2382 – 2386, 1996.

- [31] Engel SA. Glover GH. and Wandell BA. Retinotopic organization in human visual cortex and the spatial precision of functional mri. *Cereb Cortex.*, 7(2):181 – 192, 1997.
- [32] Sereno MI. Dale AM. Reppas JB. Kwong KK. et al. Borders of multiple visual areas in humans revealed by functional magnetic resonance imaging. *Science.*, 268(5212):889 – 893, 1995.
- [33] Wandell BA. Computational neuroimaging of human visual cortex. *Annu Rev Neurosci*, 22:145 – 173, 1999.
- [34] Press WA. Brewer AA. Dougherty RF. Wade AR. and Wandell BA. Visual areas and spatial summation in human visual cortex. *Vision Res.*, 41(10 – 11):1321 – 1332, 2001.
- [35] Goshima S. Kanematsu M. Kondo H. Yokoyama R. Kajita K. Tsuge Y. Watanabe H. Shiratori Y. Onozuka M. Moriyama N. Diffusion-weighted imaging of the liver: optimizing b value for the detection and characterization of benign and malignant hepatic lesions. *J Magn Reson Imaging*, 28(2):691 – 697, 2008.
- [36] Talwalkar JA. Yin M. Fidler JL. Sanderson SO. Kamath PS. Ehman RL. Magnetic resonance imaging of hepatic fibrosis: emerging clinical applications. *Hepatology*, 47(1):332 – 342, 2008.
- [37] Cui Y. Zhang XP. Sun YS. Tang L. Shen L. Apparent diffusion coefficient: potential imaging biomarker for prediction and early detection of response to chemotherapy in hepatic metastases. *Radiology*, 248(3):894 – 900, 2008.
- [38] Mazaheri Y. Shukla-Dave A. Muellner A. Hricak H. Mr imaging of the prostate in clinical practice. *MAGMA*, Epub:Ahead of print, 2008.
- [39] Somford DM. Fütterer JJ. Hambrock T. Barentsz JO. Diffusion and perfusion mr imaging of the prostate. *Magn Reson Imaging Clin N Am*, 16(4):685 – 95, 2008.
- [40] Nakai R. Azuma T. Sudo M. Urayama S. Takizawa O. Tsutsumi S. Mri analysis of structural changes in skeletal muscles and surrounding tissues following long-term walking exercise with training equipment. *J Appl Physiol*, 105(3):958 – 963, 2008.
- [41] Bammer R. Basic principles of diffusion-weighted imaging. *Eur J Radiol.*, 45:169 – 184, 2003.
- [42] Jones DK. Horsfield MA. Simmons A. Optimal strategies for measuring diffusion in anisotropic systems by magnetic resonance imaging. *Magn Reson Med*, 42:515 – 525, 1999.
- [43] Behrens TE. Clare S. Nunes RG. Jezzard P. Self-navigated multishot echo-planar pulse sequence for high-resolution diffusion-weighted imaging. *Magn Reson Med.*, 53(6):1474 – 1478, 2005.
- [44] Le Bihan D. Mangin JF. Poupon C. Clark CA. Pappata S. Molko N. Chabriat H. Diffusion tensor imaging: concepts and applications. *J Magn Reson Imaging*, 13(4):534 – 46, 2001.

- [45] Mukherjee P. Berman JI. Chung SW. Hess CP. Henry RG. Diffusion tensor mr imaging and fiber tractography: theoretic underpinnings. *AJNR Am J Neuroradiol.*, 29(4):632 – 641, 2008.
- [46] Özarlan E. Mareci TH. Generalized diffusion tensor imaging and analytical relationships between diffusion tensor imaging and high angular resolution diffusion imaging. *Magn Reson Med*, 50(5):955 – 965, 2003.
- [47] Hess P.Ch. Mukherjee P. Han E.T. Xu D. and Vigneron D.B. Q-ball reconstruction of multimodal fiber orientations using the spherical harmonic basis. *Mag. Res. Med.*, 56(1):104 – 117, 2006.
- [48] Descoteaux M. Angelino E. Fitzgibbons S. Deriche R. Regularized, fast, and robust analytical q-ball imaging. *Magn Reson Med.*, 58(3):497 – 510, 2007.
- [49] Anderson AW. Measurement of fiber orientation distributions using high angular resolution diffusion imaging. *Magn Reson Med*, 54(5):1194 – 106, 2005.
- [50] Mori S. and van Zijl P.C. Fiber tracking: principles and strategies - a technical review. *NMR Biomed.*, 15(7 – 8):468 – 480, 2002.
- [51] Parker GJ. Haroon HA. Wheeler-Kingshott CA. A framework for a streamline-based probabilistic index of connectivity (pico) using a structural interpretation of mri diffusion measurements. *J Magn Reson Imaging.*, 18(2):242 – 254, 2003.
- [52] Perrin M. Poupon C. Rieul B. et al. Validation of q-ball imaging with a diffusion fibre-crossing phantom on a clinical scanner. *Philos Trans R Soc Lond B Biol Sci*, 360:881 – 891, 2005.
- [53] Assaf Y. Freidlin RZ. Rohde GK. and Basser PJ. New modeling and experimental framework to characterize hindered and restricted water diffusion in brain white matter. *Magn Reson Med*, 52:965 – 978, 2004.
- [54] Jones DK. Determining and visualising uncertainty in estimates of fiber orientation from diffusion tensor mri. *Mag. Res. Med.*, 49(1):7 – 12, 2003.
- [55] Tournier JD. Calamante F. and Connelly A. Robust determination of the fibre orientation distribution in diffusion mri: non-negativity constrained super-resolved spherical deconvolution. *Neuroimage*, 35(4):1459 – 1472, 2007.
- [56] Jian B. and Vemuri BC. A unified computational framework for deconvolution to reconstruct multiple fibers from diffusion weighted mri. *IEEE Trans Med Imaging*, 26(11):1464 – 1471, 2007.
- [57] Sherbondy AJ Dougherty RF Napel S and Wandell BA. Identifying the human optic radiation using diffusion imaging and fiber tractography. *J. Vis.*, 8(10):12.1–11, 2008.
- [58] Dyrby TB. Søgaard LV. Geoffrey JP. Alexander DC. Lind ML. Baare WFC. Hay-Schmidt A. Eriksen N. Pakkenberg B. Paulson OB and Jelsing J. Validation of in vitro probabilistic tractography. *NeuroImage*, 37:1267–1277, 2007.
- [59] Mori S. Crain B.J. Chacko V.P. and Van Zijl P.C.M. Three-dimensional tracking of axonal projections in the brain by magnetic resonance imaging. *Ann. Neurol.*, 45(2):265 – 269, 1999.

- [60] Behrens T.E. Berg H.J. Jbabdi S. Rushworth M.F. and Woolrich M.W. Probabilistic diffusion tractography with multiple fibre orientations: What can we gain? *Neuroimage*, 34(1):144 – 155, 2007.
- [61] Heiervang E. Behrens TE. Mackay CE. Robson MD. and Johansen-Berg H. Between session reproducibility and between subject variability of diffusion mr and tractography measures. *NeuroImage*, 33:867–877, 2006.
- [62] Lazar M. and Alexander AL. An error analysis of white matter tractography methods: synthetic diffusion tensor field simulations. *NeuroImage*, 20:1140–1153, 2003.
- [63] Behrens TE Johansen-Berg H Woolrich MW Smith SM Wheeler-Kingshott CA Boulby PA Barker GJ Sillery EL Sheehan K Ciccarelli O Thompson AJ Brady JM and Matthews PM. Non-invasive mapping of connections between human thalamus and cortex using diffusion imaging. *Nat Neurosci.*, 6(7):750–757, 2003.
- [64] Descoteaux M Deriche R Knösche TR and Anwander A. Deterministic and probabilistic tractography based on complex fibre orientation distributions. *IEEE Trans Med Imaging.*, 28(2):269–86, 2009.
- [65] Kezele I Descoteaux M Poupon C Poupon F and Mangin JF. Spherical wavelet transform for odf sharpening. *Med Image Anal.*, Epub, 2010.

Appendix A

CURRICULUM VITAE

KAMIL GORCZEWSKI

ul. Gen. Bema 32 m. 25; PL44103 Gliwice

+48784067545

kamil@gorczewski.pl

PERSONAL DETAILS

Date and place of birth: 3.VI.1980 in Gliwice – Poland
Marital status: single

PROFESSIONAL EXPERIENCE

Maria Skłodowska-Curie Memorial Cancer Centre and Institute of Oncology
Department of Nuclear Medicine and Endocrine Oncology

Research Assistant Nov 2007 – present

Physicist Feb – Oct 2007

University of Tübingen
Department of Neuroradiology
Section for Experimental Magnetic Resonance of the Central Nervous System

Research Assistant 2005 – 2007

Maria Skłodowska-Curie Memorial Cancer Centre and Institute of Oncology
Department of Nuclear Medicine and Endocrine Oncology

Physicist 2002 – 2005

Medical-Technical Assistant 2001 – 2002

Maria Skłodowska-Curie Memorial Cancer Centre and Institute of Oncology
Department of Medical Physics

Apprenticeship/training 2001

EDUCATION

PhD student of the Medical Faculty 2005 – present

University of Tübingen – Medical Faculty – Germany

Thesis: *"Multi-directional diffusion weighted imaging: Implementation, verification and clinical application"*

Master's degree in Medical Physics 2004

University of Silesia – Institute of Physics – Katowice City – Poland

Thesis: *"Border: tumour – normal tissue. Comparison between 1H Magnetic Resonance in vivo Spectroscopy and Magnetic Resonance Imaging data"*

Bachelor on science degree in Medical Physics 2002

University of Silesia – Institute of Physics – Katowice City – Poland

Thesis: *"Application of Neural Networks in tumour phenotypes recognition"*

REVIEWED PUBLICATIONS

1. **Gorczewski K.**, Sokół M.; "An application of neural networks and 1H MR in vivo spectroscopy in brain tumour recognition" *Wspolcz Onkol* (2003) vol.7, 1(62 – 66) [Polish]
2. d'Amico A., Szczucka K., Borys D., **Gorczewski K.**, Steinhof K.; "SPECT-CT fusion: a new diagnostic tool for endocrinology" *Endokrymol Pol* (2006);57(Suppl A):71-74
3. Borys D., Panek R., **Gorczewski K.**, d'Amico A., Steinhof K., Psiuk-Maksymowicz K.; "Evaluation of SPECT-CT Image Fusion Quality Control" *Biocybernetics and Biomedical Engineering* vol.26(4) 2006, pp.81-92
4. Psiuk-Maksymowicz K., Borys D., **Gorczewski K.**, Steinhof K., d'Amico A.; "CT/SPECT images fusion in patients treated with iodine-131" *Journal of Medical Informatics and Technologies* vol.8 (2004),pp. II-7 – II-13
5. **Gorczewski K.**, Steinhof K., Borys D., Psiuk K.; "Our first experience with SPECT – CT Image Fusion" *Wspolcz Onkol* (2004) vol. 8; 4(223 – 226)
6. Borys D., Szczucka K., **Gorczewski K.**, Bekman B.; "E.cam DUET gamma camera model validation in GATE", *Journal of Medical Informatics and Technologies*,11(2007) 246-252
7. **Gorczewski K.**, Mang S., Klose U. "Reproducibility and consistency of evaluation techniques for HARDI data.", *Magn Reson Mater Phys.* 2009 Feb;22(1):63-70

CONFERENCE PROCEEDINGS

1. Borys D., Szczucka K., **Gorczewski K.**, Bekman B.; "E.cam DUET gamma camera model validation in GATE" - International Conference of Medical Informatics and Technologies 2007 [oral presentation]
2. **Gorczewski K.**, Saur R., Sharpe L., Erb M., Grodd W., Jäggle H., Klose U. "Reconstruction of the Optic Radiation by means of Combined DTI and fMRI" - Joint Congress of International Society of Magnetic Resonance in Medicine and European Society of Magnetic Resonance in Medicine and Biology - 2007 [Poster presentation]
3. **Gorczewski K.**, Klose U., "Comparison of the main diffusion direction calculated by means of the tensor model and the q-ball reconstruction" - Congress of European Society of Magnetic Resonance in Medicine and Biology - 2006 [Poster presentation]
4. **Gorczewski K.**, Saur R., Sharpe L., Erb M., Grodd W., Jäggle H., Klose U. "Reconstruction of the Optic Radiation by means of Combined DTI and fMRI" - New developments in MR imaging and spectroscopy workshop - 2006 [oral presentation]
5. d'Amico A., Panek R., Borys D., **Gorczewski K.**, Steinhof K., Psiuk-Maksymowicz K., Jarzab B. "Importance of quality control of SPECT-CT fusion In patients treated with 131-iodine" Annual Congress of European Association of Nuclear Medicine - 2005 [Poster presentation]
6. **Gorczewski K.**, Klose U., "Evaluation of multidirectional diffusion weighted MR images" Marie Curie Conference - 2006 [Poster presentation]
7. **Gorczewski K.**, Klose U., "Multidirectional Analysis of ADC Values in Diffusion Weighted MR Images of the Brain" - International Conference of Medical Physics - 2005
8. Borys D., Szczucka K., **Gorczewski K.**; "The point-based image registration method of SPECT/CT in I-131 imaging for quantitative analysis purposes"; AbstractBook; Workshop "Quantitative Imaging and Dosimetry in Nuclear Medicine", Berder Island, France.
9. Szopa I., **Gorczewski K.**, d'Amico A., Jarzab B. "18F-FDG standard uptake value in liver as reference point: analysis of temporal stability and correlation with physiological variables" Annual Congress of European Association of Nuclear Medicine - 2008 [Poster presentation]